PURSUING THE PLASMA DYNAMO AND MRI IN THE LABORATORY : HYDRODYNAMIC STUDIES OF UNMAGNETIZED PLASMAS AT LARGE MAGNETIC REYNOLDS NUMBER

by

David B. Weisberg

A dissertation submitted in partial fulfillment of
the requirements for the degree of

Doctor of Philosophy

(Physics)

at the

UNIVERSITY OF WISCONSIN–MADISON

2016

Date of final oral examination: May 13, 2016

The dissertation is approved by the following members of the Final Oral Committee:

Cary B. Forest, Professor, Physics

John S. Sarff, Professor, Physics

Ellen Zweibel, Professor, Astronomy & Physics

Jan Egedal, Associate Professor, Physics

Chris Hegna, Professor, Nuclear Engineering and Engineering Physics

ProQuest Number: 10112667

All rights reserved

INFORMATION TO ALL USERS
The quality of this reproduction is dependent upon the quality of the copy submitted.

In the unlikely event that the author did not send a complete manuscript
and there are missing pages, these will be noted. Also, if material had to be removed,
a note will indicate the deletion.

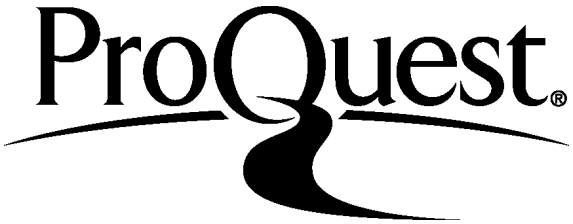

ProQuest 10112667

Published by ProQuest LLC (2016). Copyright of the Dissertation is held by the Author.

All rights reserved.
This work is protected against unauthorized copying under Title 17, United States Code
Microform Edition © ProQuest LLC.

ProQuest LLC.
789 East Eisenhower Parkway
P.O. Box 1346
Ann Arbor, MI 48106 - 1346

© Copyright by David B. Weisberg 2016

All Rights Reserved

Abstract

Pursuing the plasma dynamo and MRI in the laboratory : hydrodynamic studies of unmagnetized plasmas at large magnetic Reynolds number

David B Weisberg

Under the supervision of Professor Cary B. Forest

At the University of Wisconsin - Madison

A new method for studying flow-driven MHD instabilities in the laboratory has been developed, using a highly conductive, low viscosity, spherical plasma. The confinement, heating, and stirring of this unmagnetized plasma has been demonstrated experimentally, laying the foundations for the laboratory studies of a diverse collection of astrophysically-relevant instabilities. Specifically, plasma flows conducive to studies of the dynamo effect and the magnetorotational instability (MRI) are measured using a wide array of plasma diagnostics, and compare favorably to hydrodynamic numerical models.

The Madison plasma dynamo experiment (MPDX) uses a cylindrically symmetric spherical boundary ring cusp geometry built from strong permanent magnets to confine a large (R=1.5 m), warm ($T_e < 20$ eV), dense ($n_e < 5 \times 10^{18}$ m^{-3}), unmagnetized plasma. Detailed probe measurements of plasma transport into the edge cusp have demonstrated that particle confinement follows an ambipolar diffusion model, wherein unmagnetized ions are the more mobile plasma species and total plasma transport is limited by the slow cross-field diffusion of magnetized electrons. Emissive discharge heating is shown to be an efficient method of plasma heating, but limitations caused by instabilities in the anode-plasma sheath are found to prohibit the desired access to the full dimensionless parameter space in *Re* and *Rm*.

The plasma is stirred via $\mathbf{J} \times \mathbf{B}$ torques using current drawn from emissive LaB_6 cathodes located at the magnetized plasma edge, which also ionize and heat the plasma via sizable discharge current injection. Combination Langmuir/Mach probes measure maximum velocities of 6 km/s and 3 km/s in helium and argon plasmas, respectively, and ion viscosity is shown to be an efficient mechanism for transporting momentum from the magnetized edge into the unmagnetized core. Momentum loss to neutral charge-exchange collisions serves as the main source of drag on the bulk plasma velocity, and ionization fraction (He ~ 0.6, Ar ~ 0.95) is shown to be a limiting factor in momentum penetration. High Alfven Mach number flows have also been generated by drawing current across a global axial magnetic field, resulting in a velocity geometry conducive to MRI experiments. The experiment has achieved magnetic Reynolds numbers of $Rm < 250$ and fluid Reynolds numbers of $Re < 200$ (significantly higher than previous flow experiments in cusp-confined plasmas), setting the stage for future research of flow-driven MHD instabilities.

For Lynn.

ACKNOWLEDGMENTS

It's hard to believe that my journey through the halls of higher education is about to come to a close. Through all the classes, conferences, papers, and presentations, my friends and family have been the twin pillars of support that have kept me upright and pointed in right direction. I know for a fact that I would not be where I am today without their continuous guidance, love, camaraderie, and friendship. I could delve the thesaurus for the most syllabled adjectives and I still wouldn't be able to express the extent of my gratitude, so let me say simply this: you are all the important stuff of this world, the rest is just table dressing.

First, let me thank my adviser Professor Cary B. Forest. His unlimited energy and unbridled enthusiasm have created a research team of the highest caliber, of which I am proud to be a member. His leadership by example has enhanced my growth as a young scientist, and his constant pursuit of the unknown and unconquered will forever be to me a model of the best parts of scientific study. Cary, the amount of trust you placed in me during my years building MPDX is humbling, and I hope my work has laid a solid foundation for the continued success of laboratory astrophysics at UW.

To John Wallace and Mike Clark, thank you for your irreplaceable assistance in all things mechanical. Your clever and bombproof engineering designs are what really made this research possible, and it's a testament to your work that such a complex experiment can be successful with only a couple of permanent staff. The quality of this research is largely thanks to the mentorship of Dr. Chris Cooper, who provided an endless supply of advice, ideas, and laughs while driving MPDX from its humble beginnings to the well-diagnosed device it is today. Also much gratitude is due to Dr. Cami Collins and Dr. Ivan Khalzov, who provided the experimental and theoretical foundations for this research through their exemplary work at UW. I am proud to be leaving the

future of this research in the hands of a group of exemplary graduate students; Jason, Ken, Joe, Ethan, and Doug, it has been a pleasure working with you. And of course the hard work of undergraduate researchers was indispensable in constructing the many custom hardware and software systems on MPDX, and I thank Blair, Carl, Andy, and Austin for their dedicated efforts.

Special thanks to Doug, Mike, and Sarah in the instrumentation shop for gently critiquing and correcting my attempts at being a materials engineer; your expertise and advice have produced the prettiest graphite filaments I've ever seen. Thanks to Mikhail and Dave in the electronics shop for their help with all thing circuitry-related, to Alex Squitieri for his unerring maintenance of the various MPDX networks and databases, and to Victor Desangles for his companionship during a semester which would have been so much less productive without him. Also thanks to Dale Schutte and Christine Hrenak for making the plasma physics group the smooth-running, science-doing machine it is today. My years in Madison wouldn't have been nearly as rewarding (or endurable) without the friendship of the rest of the 2009 physics graduate students. Dan, Marty, Guilhem, Josh, Zach, Dan, Zack, Bill, Kara, Jake; the memories we've made here ensure that Madison will forever feel like home to me.

My parents were the very first to encourage my love of science, and I am forever indebted to them for their unwavering love and support. They have given me the means and the will to pursue this accomplishment, as well as the values and integrity to know that this is not an end unto itself but a means to a better world. Mom, Dad, the effort I've put into this thesis is dwarfed by the love you've put into raising me and my siblings, and I couldn't have asked for anything more.

Finally, and most importantly, thank you to my beautiful wife Lynn. You have been the sun on my face during fair weather and the light guiding me home through the storm. You took a chance following me to Madison at the start of this venture, and now we're leaving for the next step in this incredible thing called life. I couldn't imagine anyone else at my side.

TABLE OF CONTENTS

Page

Abstract . . . i

Table of Contents . . . vi

1 Introduction and Motivation . . . 1

1.1 Astrophysical Flow-driven Instabilities . . . 2
1.2 Building a Novel Flow-dominated Plasma Device . . . 7
1.3 Thesis Outline . . . 10

2 Experimental Device . . . 12

2.1 Vacuum Vessel . . . 12
2.1.1 Geographic Coordinate System . . . 15
2.1.2 Vacuum System . . . 16
2.1.3 Gas Fill System . . . 16
2.1.4 Water Cooling . . . 17
2.2 Permanent Magnets . . . 17
2.3 Plasma Heating . . . 18
2.3.1 LaB_6 Emissive Cathodes . . . 19
2.3.2 Anodes . . . 31
2.3.3 Cathode Heater Control System . . . 32
2.3.4 Discharge Power Supply System . . . 35
2.4 Plasma Diagnostics and Data acquisition . . . 37
2.4.1 Langmuir and Mach probes . . . 38
2.4.2 mm-wave interferometer . . . 40
2.4.3 Fabry-Perot spectrometer . . . 41
2.4.4 Additional non-invasive diagnostics . . . 42
2.4.5 Data acquisition and analysis . . . 42

3 Measurements of cusp plasma losses and comparison to a quasi 1D transport model 44

3.1 Edge transport measurements . . . 45

Page

3.2 Ambipolar diffusive transport theory . . . 52
3.3 Linear transport model . . . 53
3.4 Linear model results . . . 65
3.5 Edge ion drift modeling and measurements . . . 70

4 Global plasma confinement: Particle, Charge, and Power balance . . . 73

4.1 Arc Discharge Heating . . . 74
4.2 Particle Balance . . . 79
4.3 Current Balance . . . 82
4.4 Power Balance . . . 84
4.5 Numerical balance calculations . . . 86

5 Two techniques for stirring high Alfven Mach number plasmas . . . 92

5.1 Numerical modeling of plasma hydrodynamics . . . 92
5.2 Edge-driven Flow . . . 98
5.2.1 Counter-rotating hemispheres . . . 100
5.2.2 Co-rotating hemisphere . . . 103
5.3 Volumetric-driven Flow . . . 105
5.4 Prospects for instability measurements . . . 109

6 Conclusion . . . 111

6.1 Summary of Thesis . . . 111
6.2 Future Work . . . 114

APPENDICES

Appendix A: Vacuum Field Equations . . . 116
Appendix B: Hydrodynamic model . . . 123

REFERENCES . . . 124

Chapter 1

Introduction and Motivation

Plasma physics is fundamental to our understanding of astrophysical phenomena. The vast majority of matter throughout the universe is in an ionized state, and the action-at-a-distance of electromagnetic forces can play a critical role in a wide variety of observed and theorized phenomena. In order to better understand astrophysical processes like the dynamo effect and the magnetorotational instability, it is important to have laboratory experiments that can investigate the fundamental physics underlying these complex systems. This is no small task, as laboratory plasmas exist in a parameter space far removed from interstellar and galactic scales. But a new experimental device has been constructed that aims to narrow this gap: the Madison plasma dynamo experiment (MPDX). This doctoral thesis will present the initial results of confinement, heating, and hydrodynamic studies on a novel unmagnetized plasma device, with the goal of applying these findings to further our understanding of flow-driven MHD processes in astrophysical systems.

This Chapter will introduce the thesis as follows: In Section 1.1, the theoretical basis for flow-driven MHD instabilities will be presented. Section 1.2 will describe the rational behind the design of MPDX as the next generation in laboratory astrophysics, and will outline the desired experimental goals. Finally, a map of this thesis is given in Section 1.3.

1.1 Astrophysical Flow-driven Instabilities

A flow-driven MHD instability is defined as an MHD instability in which the dominant source of free energy lies not in the magnetic energy but in the kinetic flow energy of the system. These types of systems are quite common in astrophysical contexts due to the usually weak magnetic field strength of the interstellar and galactic magnetic fields. Even stellar magnetic fields are much weaker than the kinetic energy in the turbulent flows of dense stellar material. These flows are driven by various types of non-magnetic energy sources, ranging from thermal convection at the surface layer of stars, to radiation pressure at the shock fronts of supernovae, to Keplarian rotation of gravitationally-bound proto-stellar material. In these cases the existence of a weak magnetic field does not initially determine the dynamics of the system; instead a flow-driven instability is needed to amplify the magnetic field to sufficient levels where it may have enough of an impact to result in a new, saturated state of the system.

The two main examples of flow-driven MHD instabilities relevant to this thesis are the dynamo effect and the magnetorotational instability (MRI). In fact, the hydrodynamic results presented in Chapter 5 are direct attempts at generating suitable flow geometries for the excitation of these two instabilities. A brief description of each instability is given here, with the intent of motivating their study on MPDX.

The dynamo effect is the theoretical mechanism for the inductive generation and maintenance of astrophysical magnetic fields. Without such an effect, most observed magnetic fields would have decayed to negligible levels due to magnetic diffusion; i.e. ohmic losses in a resistive medium. For example, the Earth's magnetic field is a result of the complex fluid motions within the liquid metal outer core, thought to consist primary of liquid iron and other lighter silicates that precipitate down from the solid mantle [1]. If there were no inductive processes to generate magnetic energy from the sizable flows in the Earth's core, then the free decay time for a loop of current would be of the order $\tau = R^2/\lambda\pi^2$, where $\lambda = 2.6\,\mathrm{m^2 s^{-1}}$ is the resistivity of the liquid metal and $R = 3500\,\mathrm{km}$ is the radius of the core. This works out to be about 1.5×10^4 years, which is considerably shorter than the 4 billion year lifetime of the Earth. Added to this discrepancy in time

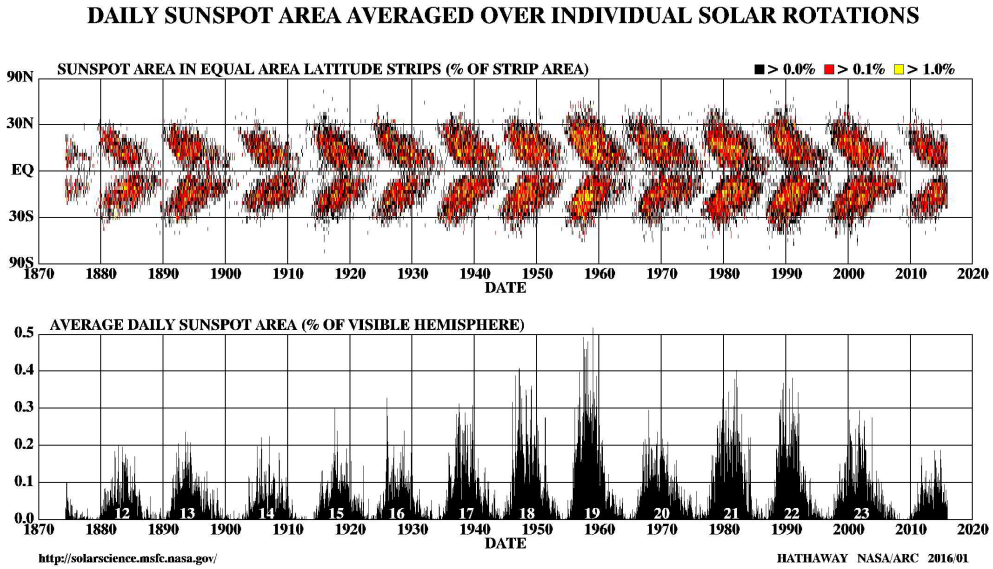

Figure 1.1: The sunspot 'Butterfly diagram', showing the 11 year solar half-cycle and the corresponding sunspot migration from mid- to low-latitudes. Not shown: the global polarity reversal that occurs after each half-cycle. Image courtesy of the NASA/Marshall Space Flight Center.

scales are the geological observations of magnetic reversals encoded in million-year old rock on the ocean floor. While random in occurrence, these reversals are on average spaced apart by about 2×10^5 years, indicating a dynamic, non-linear process. A similar periodicity is observed in the solar magnetic field, albeit on a much shorter timescale. The solar cycle is a well-known 22 year cycle that involves two maxima and two minima of global field strength with a polarity reversal every 11 years. One visible signature of this is the increase and decrease of sunspots on the solar surface; indeed, sunspot measurements have been conducted since the late 19th century and are often summarized in the so-called Butterfly diagram, shown in Fig 1.1. The higher conductivity of the plasma in the solar convective zone is significantly higher than that of the Earth's core, and so the solar dynamo resistive time is much longer; on the order of the age of the sun. But the well-documented short time-scale activity of the solar magnetic field argues convincingly for the existence of an inductive process driving field dynamics.

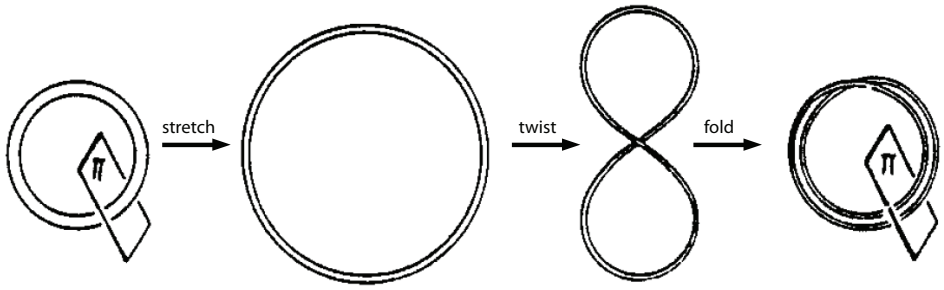

Figure 1.2: The 'stretch, twist, fold' description of magnetic amplification. A single flux tube is lengthened by the plasma flow, increasing magnetic tension, and then folded back onto itself such that the original flux through the surface Π is doubled. Taken from [2].

Dynamo theory can be divided into two types of systems. 'Slow' dynamos are laminar systems, with simple flow geometries and relatively low conductivity. The 'stretch, twist, fold' process of magnetic amplification, described by Moffatt [2] and diagrammed in Fig. 1.2, relies on a single closed flux tube that is folded back onto itself by a similarly simple flow. The magnetic instability growth rate is tied to the time it takes for one iteration of this cycle to occur, which is usually the same as a single eddy turn-over time. If the system's flows are laminar then this picture exists only at the macroscopic level and the eddy turn-over time is relatively long, resulting in a slow instability growth rate. But if the system is turbulent, then this picture can be applied to every eddy scale size, and the average eddy turn-over time is much smaller. This second case is identified as a 'fast' dynamo, since the resulting magnetic instability growth rate is significantly faster than the laminar case [3].

The type of dynamo is determined using a set of dimensionless parameters to relate the competing sources and sinks of kinetic and magnetic energy. The fluid Reynolds number *Re* is a common concept from hydrodynamics and is the ratio between momentum advection and momentum diffusion due to viscosity. The magnetic Reynolds number *Rm* is the analogous ratio for inductive effects, being the ratio between magnetic advection and magnetic diffusion due to resistivity. These parameters are defined in terms of some characteristic length and velocity, usually the system size and peak flow speed, which characterizes the magnitude of the velocity gradients wherein lies the

free energy for the 'stretch, twist, fold' of magnetic flux tubes. The ratio of *Rm* to *Re* is known as the magnetic Prandtl number and is a characteristic of the conducting medium itself, determining whether the turbulent cascade bottoms out at the viscous scale length before or after the minimum magnetic scale length has been reached:

$$Re = \frac{VL}{\nu}$$
$$Rm = \frac{VL}{\eta}$$
$$Pm = \frac{Rm}{Re} = \frac{\nu}{\eta}$$

Generally speaking, a flow-driven MHD instability will only be excited if the parameter *Rm* is large enough. As the kinetic energy in the flow is initially much larger than the magnetic energy, field will be advected so long as the fluid has a large enough conductivity. An ideal flow geometry will advect field so that flux density is increased, leading to growing magnetic eigenmodes and possibly a globally amplified field. If *Rm* is too small (i.e. the fluid is too resistive) then magnetic diffusion will rise to dominance before flux density is measurably enhanced, preventing the dynamo instability from taking off. For a given viscosity and resistivity coupled with a specific flow geometry, a liminal Rm_{crit} can be identified above which the magnetic growth rate becomes positive.

Astrophysical dynamos are gigantic systems with large flow velocities; the values of *Re* associated with these systems are usually on the order of 10^{10} or greater, predicting highly turbulent flows. It is therefore likely that these are 'fast' dynamos [4]. The salient feature of 'fast' dynamos in this regard is the independence of instability growth on *Rm* in the highly conducting limit. In slow, laminar dynamo theory the magnetic growth rate is positive only for a finite range in *Rm*, as the large-scale flux tube advection becomes impossible at very high conductivity due to the frozen-in flux condition. In turbulent systems, numerical models suggest that the magnetic growth rates approaches a constant positive value as *Rm* trends towards infinity [5, 6, 7], a result that bodes well for this theory in the context of some astrophysical systems like the interstellar and intergalactic media where *Rm* might be just as large as (or larger than) *Re*. A laboratory dynamo experiment

would ideally be able to probe both types of dynamos, the 'slow' dynamo being a macroscopic version of the many microscopic building blocks of the more astrophysically-relevant 'fast' dynamo.

The magnetorotational instability (MRI), like the dynamo, is a theory that uses MHD turbulence to explain the growth rate of an astrophysical phenomena that would otherwise be orders of magnitude slower than observations suggest. The accretion of matter in a gravitationally bound system is a universally occurring process that marks the very first stages of planetary, solar, and galactic formation. Not only does accretion result in the coalescence of a massive central object but it can also release very large amounts of radiation, powering some of the most luminous objects in the universe. The problem, then, is whether ordinary viscous diffusion is efficient enough to account for this observed accretion rate. The simple answer is no; estimations of molecular viscosity in accretion disks leads to timescales of 3×10^7 years, which is far too slow when compared to the massive luminosity of accretion objects [8]. A turbulent system would have a significantly higher enhanced viscosity and therefore faster accretion rates [9], but Keplarian orbits are linearly stable by the Raleigh criterion and so the path to turbulence is not obvious. The solution to this was proposed several times before the application to accretion was finally realized [10, 11, 12], and involves the presence of a very weak magnetic field normal to the orbital plane. The increase in magnetic tension caused by the radial displacement of a fluid element acts as a destabilizing force: if $d\Omega/dr < 0$ then the magnetic field transfers momentum from an inwardly displaced fluid element to an outwardly displaced element. The outer element speeds up, moving to a larger radius, while the inner element does the opposite, further stretching the connecting field line and leading to an instability. Numerical simulations have shown that turbulence caused by the MRI can indeed increase the accretion rates to observed levels [13, 14, 15], but these models are limited by the large *Re* and cannot resolve both large and small fluid scales. Experimental observation of the MRI and confirmation of its impact on global turbulence has yet to be achieved in the laboratory and would be a valuable benchmark for numerical techniques.

1.2 Building a Novel Flow-dominated Plasma Device

Previous experimental work on flow-driven MHD instabilities can be generally described as an evolution from liquid metals in a constrained flow geometry, to liquid metals in a free flow geometry, to plasmas in a free flow geometry. Initial attempts at creating a dynamo in the laboratory used molten sodium forced into a helical flow using pipes with angled fins. Experiments in Riga, Latvia [16] and Karlsrhue, Germany [17] were able to excite growing magnetic eigenmodes, with the latter measuring a saturated field of 70 G. The next generation of liquid metal dynamo devices moved away from constrained flow through pipes and towards much simpler boundary conditions. Whether using a spherical [18] or cylindrical [19] vessel, impellers were used to stir the liquid metal in an axisymmetric geometry with simply connected streamlines. These experiments were successful in measuring a positive effect of specific flow geometries on global magnetic decay rates [20], but they also encountered the major limitation of liquid metals: anomalous turbulent resistivity [21]. The unconstrained, simply connected flow geometries allowed for the excitation of large fluctuations $\tilde{V}$ and $\tilde{B}$ that produced a turbulent EMF, effectively opposing the inductive current required for global dynamo excitation. The small magnetic Prantdl number ($Pm \sim 10^{-6}$) of liquid sodium meant that the critical *Rm* required for a transition to a growing magnetic eigenstate was pushed out of reach thanks to the detrimental effects of the turbulent resistivity.

The MRI has also been studied in a liquid metal experiment: the Princeton MRI experiment uses liquid gallium in the cylindrical couette geometry [22]. This effort at producing the MRI has so far been unsuccessful, although it has identified a magnetically-driven instability of the free-Shercliff-layer due to the mechanically necessary shear layers at the liquid metal boundaries [23]. Once again, it appears that the relatively small magnetic Prandtl numbers of liquid metals always leads to the dominance of inviscid effects over inductive dynamics.

The latest generation of this type of laboratory astrophysics has moved from liquid metals to plasmas as the conducting medium of choice. The name of the game is achieving as large of an *Rm* as possible, and plasmas hold several advantages in this context. First, the mass density of ionized gas is orders of magnitude smaller than metal, permitting much larger flow speeds at comparable

input power. Second, the viscosity and conductivity of a plasma are strongly dependent on the plasma temperature and density, meaning that the Reynolds numbers are not fixed functions solely of velocity and system size. Braginskii's seminal work on plasma transport properties derives these relationships in terms of measurable plasma parameters [24],

$$Re = \frac{VL}{\nu} = 7.8\frac{n_{18}\sqrt{\mu}Z^4 V_{km/s} L_m}{T_{i,eV}^{5/2}}$$

$$Rm = \mu_0 \sigma V L = 1.6\frac{T_{e,eV}^{3/2} V_{km/s} L_m}{Z}$$

where n_{18} is the plasma density in units of $10^{18} m^{-3}$, μ is the ion mass in amu, Z is the ion charge state, V and L are the characteristic flow speed and system size, and the electron and ion temperatures are in units of eV. In a plasma device where these parameters are measured and controlled, *Re*, *Rm*, and *Pm* can be varied over a much larger range than any liquid metal experiment could achieve. This opens a number of doors with respect to the possible types of dynamo that a plasma experiment might investigate. For example, the turbulent flows that prohibited dynamo excitation in the Madison dynamo experiment could instead be used in a plasma device to successfully investigate a 'fast' dynamo, since *Pm* could be increased to values much larger than unity simply increasing heating to both the electrons and ions.

The first plasma device built to investigate flow-driven MHD instabilities was the plasma couette experiment (PCX), located at the University of Wisconsin - Madison [25]. Several milestones were reached on PCX, including the successful confinement of a moderately dense, highly conducting plasma. Typical plasma parameters of $n_e = 10^{11}\,\mathrm{cm}^{-3}$ and $T_e = 8\,\mathrm{eV}$ were regularly achieved in both helium and argon plasmas, and a novel stirring electrode array was designed to spin the plasma edge to maximum speeds of 3 km/s [26, 27]. This excellent work by C. Collins resulted in dimensionless parameters of $Re = 1 - 23$, $Rm = 1 - 23$, and $Pm = 0.3 - 5.5$; a completely new parameter regime for this type of experiment [28]. The cylindrical geometry of PCX is ideally suited for a close study of the MRI in accretion disks, and the permanent magnet confinement scheme (shown in Fig. 1.3) was crucial in providing good confinement without the presence of a strong guide field in the plasma core. Despite all its accomplishments, PCX did not observe

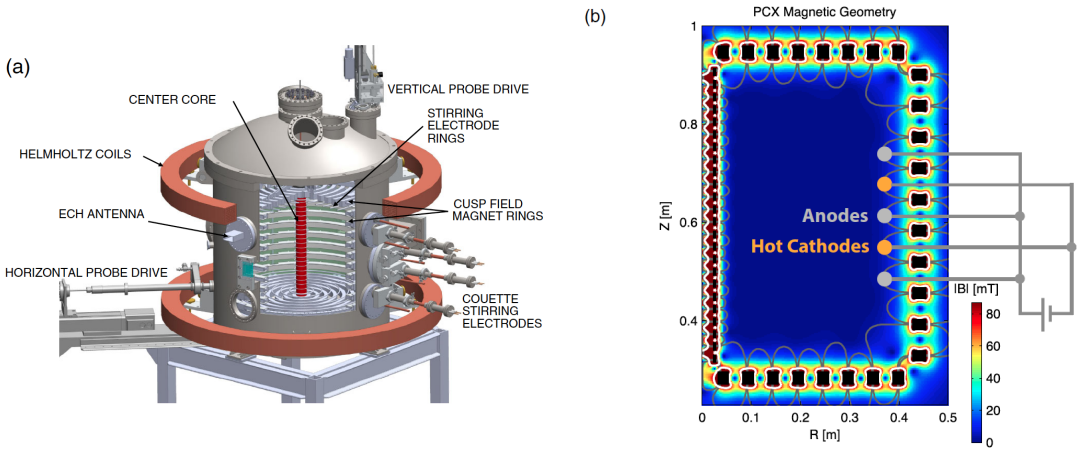

Figure 1.3: The plasma couette experiment (PCX). a) Experiment schematic, showing cylindrical vacuum chamber, permanent magnet rings, stirring electrodes, ECH waveguide, and probe locations. b) Magnetostatic simulation of ring cusp vacuum magnetic field. Stirring electrodes are inserted past the cusp field into the unmagnetized core. Taken from [26]

the MRI, most likely due to an insufficiently large *Rm* as well as a poorly controlled radial velocity profile. The addition of a center magnet stack with accompanying stirring electrodes helped shift the flow geometry so that the condition $d\Omega/dr < 0$ was marginally satisfied at certain locations, but the overall accomplishments seemed to suggest that a new experiment could be designed based on the valuable insights gained thus far.

Building on the lessons learned from previous work, the next experiment in this new generation of plasma laboratory astrophysics was designed and constructed at the University of Wisconsin - Madison: the Madison plasma dynamo experiment (MPDX). Many of the MPDX design components are taken from successful operations on PCX, first and foremost being the permanent magnet cusp field. A total of 36 axisymmetric magnet rings are used to confine the plasma, and improvements in magnet fabrication have permitted higher magnet energy density as well as better thermal contact with the water cooled vessel wall. With the ultimate goal of attaining the maximum *Rm*, the size of the device was increased three-fold over the dimensions of PCX to a diameter of 3 m, and the vessel geometry was chosen to be spherical instead of cylindrical. This allows MPDX to investigate a wider range of flow-driven instabilities, drawing on results from previous spherical

dynamo experiments but still retaining the cylindrical symmetry that facilitates investigation of the MRI. MPDX also uses the plasma stirring techniques developed on PCX, upgrading the emissive electrodes to a LaB_6 design that can draw hundreds of amps across the edge cusp field and drive plasma flow with a substantially larger $J \times B$ torque. These new emissive cathodes are also the main source of plasma heating in the current MPDX design, which while ensuring a large amount of stirring power also posses several limitations on the overall power input. One of the most convenient aspects of PCX, the microwave ECH system, has yet to be added to MPDX, but current work shows promise and could see a high-power ECH system installed not long after the publication of this thesis.

This thesis present the initial results of MPDX, including experiments that investigate the details of the plasma confinement by the ring cusp field and power balance inherent in the discharge heating system. Extensive probe measurements and non-invasive optical diagnostics are presented to facilitate these studies, and a set of numerical simulations are described that were used to direct experimental efforts and provide comparison to physical models. The first successful plasma flow experiments are also presented, setting the stage for future investigations into the dynamo effect and the MRI. The hydrodynamic details of an unmagnetized plasma are discussed, with an emphasis on the effect of the strong magnetic gradients at the plasma edge as well as the volumetric momentum sink that come from neutral charge-exchange collisions.

1.3 Thesis Outline

A brief outline of this thesis is presented. Throughout, the motivations and supporting theoretical work necessary are provided within each Chapter.

This introductory Chapter (Chapter 1) served to introduce the goals and challenges of studying flow-driven MHD instabilities in the laboratory, and presents a clear motivation for the thesis. Chapter 2 describes the experimental device and the plasma. Chapter 3 details the studies conducted concerning the plasma confinement; measurements of plasma flux into the cusp are presented, and a linear ambipolar diffusive transport model is described which predicts the total

plasma particle loss area as a function of core plasma parameters. Chapter 4 presents the experimental investigation of plasma heating in MPDX, including attempts at maximizing T_e and n_e and the limitations thereof. A global 0D particle and power balance model is derived in an attempt to explain the curious sensitivity of the bulk plasma potential and its deleterious effects on discharge heating. Chapter 5 describes the plasma stirring experiments conducted thus far on MPDX: 1) edge-driven follow similar to PCX experiments, where viscosity is the main conduit of momentum transport from the edge into the core and 2) volumetric-driven flow, where a weak axial field is applied and the emissive discharge current is drawn radially across the machine to generate a $J \times B$ torque that is present throughout the entire plasma volume. Chapter 6 provides concluding remarks and suggestions for future work.

Chapter 2

Experimental Device

This chapter will describe the MPDX experimental device, including details of the vacuum vessel, the ∼3000 permanent magnets that make up the cusp confinement system, and the emissive cathode discharge heating system. The MPDX diagnostic suite will also be reviewed, with emphasis on the 10-probe Mach/Langmuir probe array. A CAD schematic of the entire device is shown in Fig. 2.1, and a photo is shown in Fig. 2.3.

2.1 Vacuum Vessel

The MPDX vacuum vessel is a 3.0 m diameter sphere, consisting of two identical hemispheres of cast aluminum. A schematic of one hemisphere is shown in Fig. 2.2. Casting was done by Portage Casting & Mold, Inc., located 45 minutes north of UW Madison in Portage, WI. The wall thickness is 3.175 cm (3.0 in), which is large enough to contain a system of stainless steel cooling pipes cast into the wall. There are a large number of vacuum ports cast into the vessel wall, including one hundred eighty-four 7.5 cm (2.9 in) diameter diagnostic ports, fourteen 35 cm (13.8 in) diameter diagnostic ports, and twelve rectangular box ports (18 cm wide, 99 cm long). There are an additional two 35 cm (13.8 in) ports at the north and south poles of the vessel, which for this research were each occupied by a modified flange with an additional permanent magnet ring and three 7.5 cm (2.9 in) diagnostic ports. There are also four 35 cm (13.8 in) diameter vacuum pump ports located on the bottom of the vessel at the end of cylindrical cast extrusions such that all pumps are vertically aligned.

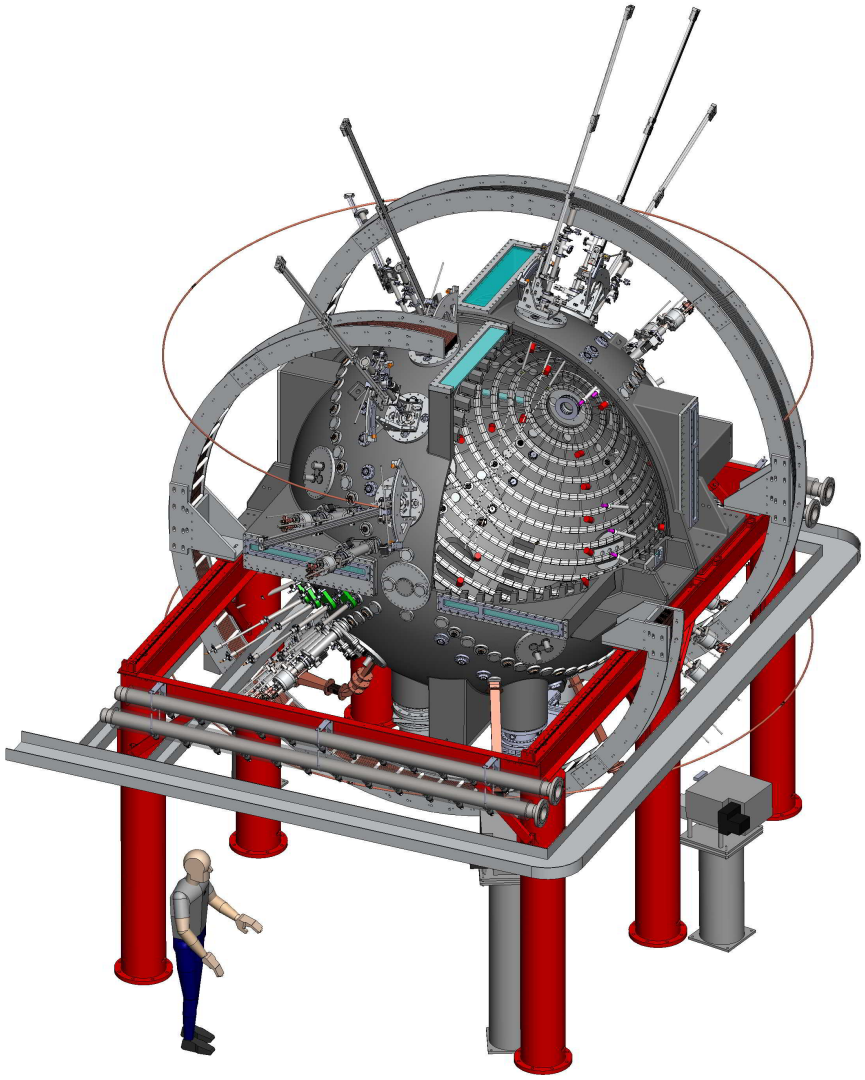

Figure 2.1: SolidWorks schematic of the MPDX experimental device.

Because the vacuum vessel is cast aluminum, all vacuum seals are made with Viton o-rings. Tapped bolt holes with stainless steel Heli-Coil inserts allow for flange connections on the exterior of the machine wall, and all circular ports have flat o-ring surfaces that are compatible with

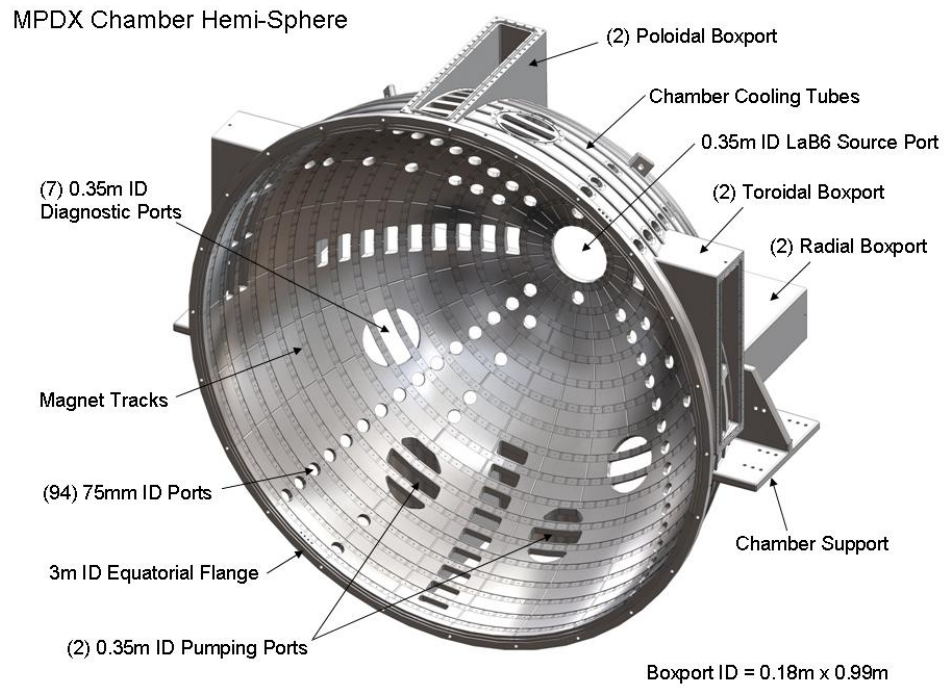

Figure 2.2: SolidWorks schematic of one of the two identical vacuum vessel hemispheres.

standard ConFlat flanges (using square cross-section Viton gaskets) as well as custom aluminum flanges (using round cross-section Viton gaskets). The larger ports, including the box ports and the equatorial vacuum seal, have double o-ring grooves machined into the aluminum vessel with differential pumping access in-between.

The entire interior of the vessel is precision machined to allow for the installation of the more than 3000 permanent magnets that make up the multi-pole cusp confinement geometry. Thirty-six axisymmetric grooves are recessed 0.32 cm (0.125 in) into the wall, and tapped screw holes are evenly spaced one magnet length ($\sim$5 cm). The remaining interior surface is coated with a 0.025 cm thick layer of alumina film using plasma spray coating, serving to ensure electrical insulation between the plasma and the vessel wall.

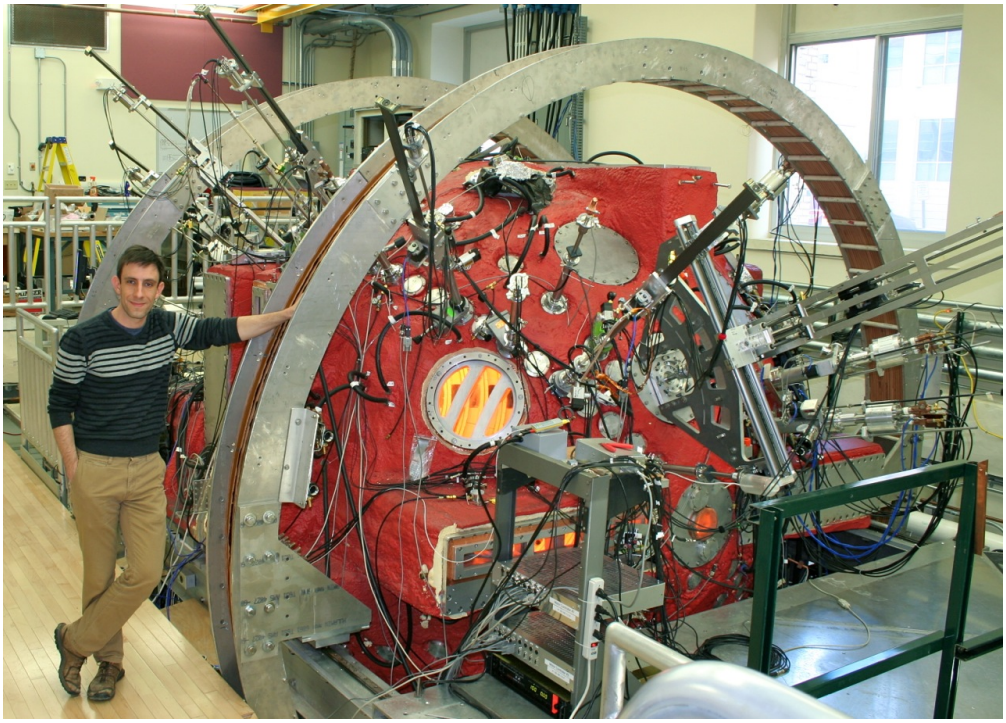

Figure 2.3: Photograph of MPDX with graduate student for scale.

2.1.1 Geographic Coordinate System

It is important to explain the various coordinate systems used in the MPDX experiment to identify locations around the surface of the vacuum vessel. Two main coordinate systems are used: spherical (θ and ϕ) and geographic (latitude and longitude). As will be discussed, MPDX has an axis of symmetry that corresponds to the z-axis in spherical geometry; the main direction of symmetry is therefore in the $\hat{\phi}$ direction. To specify a location on the vessel surface, a $\theta = 0$ point is chosen (ie: a North pole) as is a $\phi = 0$ line (ie: a prime meridian). It is more intuitive to label a position using latitude and longitude, as the two halves of the vacuum vessel meet at $\theta = \pi/2$, what is essentially the equator. Therefore lines of latitude are identified as either being in the 'northern' half of the vessel ($0 \leq \theta < \pi/2$) or in the 'southern' half of the vessel ($\pi/2 < \theta \leq \pi$). the only drawback of this geographic coordinate system is the fact that the MPDX vacuum vessel is laying on its side: the north and south poles create an axis of symmetry that is horizontal, and the equatorial plane is vertical. The axisymmetric magnet rings, however, are at lines of constant

latitude and the numerous 3 in ports are arranged along lines of longitude, and so identifying a specific port is easy and intuitive. The 'prime meridian' is arbitrarily defined as the constant ϕ line that intersects the point on the very top of the machine. The north pole of the vessel is chosen to be the one facing the west side of the experimental high bay, and is the side of the machine facing the camera in the photograph in Fig. 2.3. The magnet ring closest to the north pole happens to have its magnetization vector pointing away from the machine center, so the local magnetic field is also pointing the 'north' direction.

2.1.2 Vacuum System

Up to four vacuum pumps can be installed on MPDX at any given time. The default configuration consists of two 2000 l/m turbomolecular pumps and two 4000 l/m cryogenic pumps. Base vacuum pressure between plasma shots is 5×10^{-7} Torr, with experimental operating pressures $< 1 \times 10^{-4}$ Torr. A residual gas analyzer (RGA) is used to measure the partial pressures of fill and impurity gases, with the largest impurity component consisting of molecular and atomic hydrogen outgased from plasma-facing surfaces. Vacuum interlocks are set to close all pump gate valves and turn off cathode heating when vessel pressure rises above 1×10^{-3} Torr.

2.1.3 Gas Fill System

Neutral fill gas is puffed into the MPDX vacuum vessel using a piezoelectric puff valve, located as close as possible to the equator at 5 S. The valve is actuated by voltage between 20 V and 100 V and gas flow is roughly proportional to the applied voltage. Experimental operation usually follows the following procedure. First, a short 100 V pulse is applied to the valve for no more than 50 ms. This puffs a large amount of gas into the vessel and effectively fills it to the desired operating neutral pressure. After about 500 ms, the DC discharge bias is applied to the heating electrodes and the neutral gas is ionized into plasma. Most experiments require a constant neutral pressure over the course of the seconds-long shot, and so the valve is one again opened using a lower voltage (20 V-35 V). This slowly leaks gas into the vessel during the plasma shot, fueling the plasma and maintaining a flattop in most plasma parameters.

2.1.4 Water Cooling

The system of cooling pipes embedded in the cast aluminum wall is connected to a chilled water loop with a total cooling capacity of 1 MW. Flow is controlled by a PID feedback system, maintaining output temperature at a constant setpoint between 60° C and 70° C. The vacuum vessel is covered with $\sim$3 cm of foam insulation to prevent condensation, and is coated with red fire-resistant paint to comply with safety and school spirit regulations. Other systems that use the main chilled water loop include the turbomolecular pumps and the helium compressors associated with the cryogenic pumps, the large Helmholtz coils and their DC power supplies, and the emissive cathodes and the large polar anodes.

2.2 Permanent Magnets

Plasma confinement in MPDX is made possible by a set of over 3000 permanent samarium cobalt (SmCo) magnets distributed into thirty-six axisymmetric rings bolted to the inside of the vacuum vessel wall. The magnets in each ring are oriented so their magnetization vectors are all either in the $+\hat{r}$ or $-\hat{r}$ direction, and each ring has the opposite orientation of the two adjacent rings. This results in a high-order multi-pole cusp magnetic field that is localized to the vessel wall and drops off exponentially in radius, leaving the bulk of the vessel volume unmagnetized.

Each magnet is keystone-shaped (3.8 cm $\times$ 2.5 cm $\times$ 5.0 cm) and is secured to the vessel wall with one central bolt hole. The interior of the vessel wall is precision machined with thirty-six grooves to accept the installation of the magnets, and these rings are located at the latitudes 87.5 N, 82.5 N, ... , 2.5 N, 2.5 S, ... , 82.5 S, 87.5 S. This corresponds to an arc length spacing of 13.3 cm between magnet ring centerlines. Compared to the magnet width of 3.8 cm, this means that the magnet rings make up a total of 28.58% of the inner wall surface area. The actual plasma loss area to the wall is significantly smaller, as evidenced by the mm-wide plasma burn marks that run down the center of each magnet ring. During construction the field strength of each magnet was measured so that the entire magnet order could be binned into thirty-six groups of similar strength,

ensuring maximum axisymmetry by minimizing the standard deviation of field strength within each group.

According to factory measurements, the SmCo magnets have an intrinsic coercivity of $H_{cj} = 2116\,\text{kA/m}$ and a remanent field of $B_r = 1.06\,\text{T}$, with a maximum energy-product of $BH_{max} = 217.76\,\text{kJ/m}^3$. The remanent magnetization is given as $H_{cb} = 794\,\text{kA/m}$, which corresponds to a surface magnetization current of 19.8 kA and a surface field strength of $B_{max} = 0.305\,\text{T}$. Calibrations of vacuum field strength were done using *in situ* Hall probe measurements, and were compared to an analytic model of the permanent magnets using discrete rings of current located on the magnet ring side walls. The results of these calibrations, as well as a detailed description of the modeled magnetic field, are presented in the Appendix.

SmCo magnets were chosen over neodymium magnets primarily for their high Curie temperature and their resistance to hydrogen corrosion. While recent neodymium materials like Nd_2Fe_14B have a higher maximum energy-product and are cheaper to manufacture compared to SmCo, in-house testing determined that extended exposure to hydrogen gas at atmospheric pressure resulted in degradation of the sintered crystalline structure of the magnet. As little as six hours of exposure to H_2 gas at $\sim 700\,\text{Torr}$ transformed a nickel-coated neodymium magnet into a corroded mass of individual grain structures. SmCo magnets, however, have strong resistance to corrosion and can operate at high temperatures, with Curie temperatures of around 800° C.

After installation, all magnetic plasma-facing surfaces were covered with a layer of Kapton polyimide film followed by custom-made 0.32 cm (0.125 in) thick alumina tiles, which are held onto the magnets using small steel pins. This double layer of electric insulation is a key feature of the ambipolar plasma transport at the plasma edge, as no net current can flow to the vessel wall. It also ensures that any electric field set up across the edge field lines is not shorted out by the metallic magnet face.

2.3 Plasma Heating

Perhaps the most important feature of a experimental plasma device, the heating system must be able to inject enough power into the plasma to offset energy losses and maintain the confined

gas in an ionized state [29]. MPDX plasmas are ionized and heated using DC electrical discharges between hot emissive cathodes and cold anodes. These electrodes are inserted into the vacuum vessel through ports on the vessel wall, and are normally positioned at radial locations between $r = 120\,\text{cm}$ and $r = 135\,\text{cm}$. The large number of vacuum ports on the vessel allow for many unique arrangements of cathodes and anodes, but in general the two types of electrodes are installed on opposite sides of the device. This section will present the details of electrode design, construction, and operation. It is important to note that, unlike previous magnetic bucket experiments, this research did not have the advantage of a robust electron cyclotron resonance heating (ECRH) source. MPDX plasmas require a substantially larger amount of heating power relative to smaller plasma devices, and the 5-10 kW magnetrons which are reliably used for table-top experiments are insufficient. As will be shown, a minimum of 100 kW of discharge heating power is necessary to achieve MPDX plasmas with significant ionization fractions. However, the advantages of an ECRH system should not be overlooked, and it is hoped that the current plans to install a custom-made 100 kW magnetron system will be soon be realized. Indeed, much of the research detailed in this graduate thesis could be significantly expanded upon with such an addition, as will be discussed in later chapters.

2.3.1 LaB_6 Emissive Cathodes

MPDX cathodes are probe-like devices that are inserted through the 3 in vacuum ports ubiquitously located between magnet rings. Fig. 2.4 shows several views of cathode design. The major design components and the corresponding construction materials are:

- emissive tip (LaB_6)
- heating filament (graphite)
- tip base (graphite)
- tip base insulator (boron nitride)
- shaft conductors (copper)

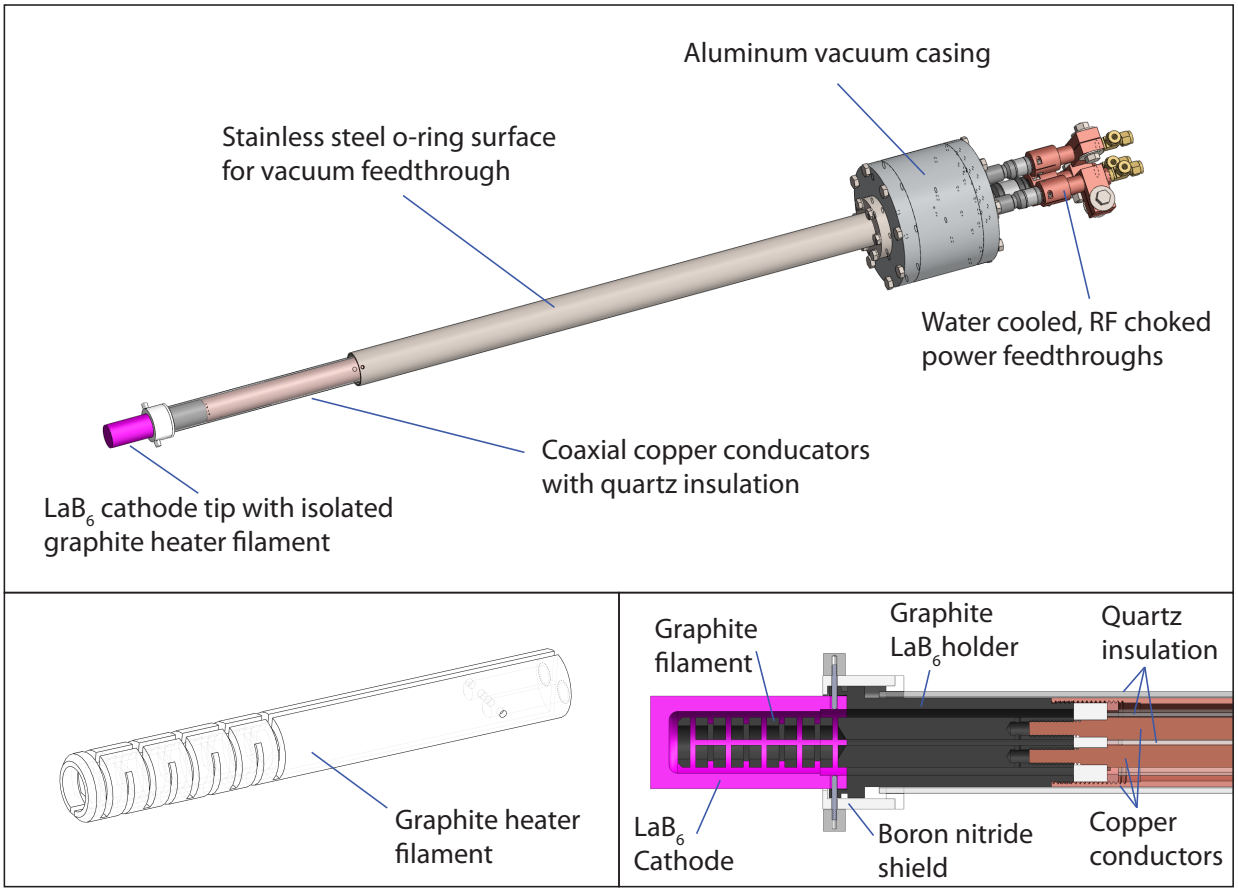

Figure 2.4: Emissive LaB_6 design. Nine-winding filament design in an upgrade from the original five-winding design.

- shaft insulator (quartz)
- sliding shaft vacuum surface (stainless steel)
- electric breakout (aluminum)
- electric vacuum feedthroughs (copper)
- water cooling / RF choke clamps (copper)

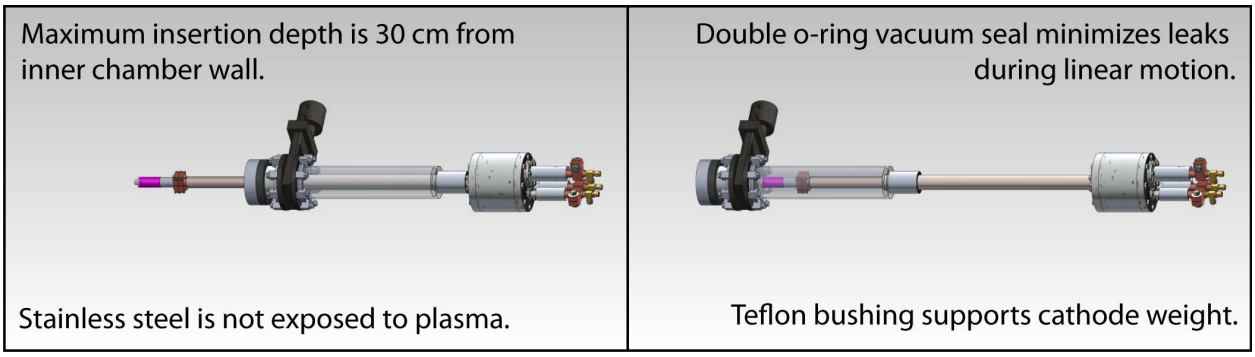

Figure 2.5: Cathode vacuum garage allows cathode installation/replacement without breaking main vacuum. The garage itself is transparent in these schematics, while the gate valve is black.

Ease of use was a priority in cathode design. Each cathode is paired with a vacuum garage, and can be quickly retracted behind a gate valve for maintenance or replacement without breaking vacuum. This garage system is shown in Fig. 2.5. The 1.5 in OD stainless steel half-nipple that makes up the majority of the shaft length is the sliding vacuum surface that allows cathode insertion under vacuum. A double o-ring vacuum seal and Teflon bushing holds the weight of the cathode in any orientation. The cathode shaft is as long as it is so that the cathode tip can be inserted to a maximum radial position of $r = 120$ cm (30 cm from the inner vessel wall) and still be retracted behind the pneumatic 3 in gate valve.

Because installation location on the vessel can make it hard to reach a particular cathode, each cathode is fitted with a remotely-controlled stepper motor and linear screw drive. Each motor is fitted with a capacitive or optical encoder that tracks the motor rotations and reports the total motion with a high level of accuracy. The array of stepper motors are controlled by three 8-axis Galil motor controllers, and motion commands are passed through from LabView VIs on the main control room computer.

Each cathode tip consists of a hollow cylinder of lanthanum hexaboride (LaB_6) that is radiatively heated by a coaxial graphite filament. LaB_6 is the emissive material that allows MPDX cathodes to reliably generate 100 kW DC discharge plasmas. It is a very hard ceramic with a relatively low work function of 2.67 eV, and is commonly used as an thermionic electron source in

low-temperature plasma devices [30, 31, 32]. When heated to high enough temperatures, electrons at the ceramic surface have enough thermal energy to escape from the semiconductor matrix and, if the cathode is electrically biased with respect to the surrounding plasma, are accelerated to hundreds of electron volts. This primary electron beam both ionizes the neutral fill gas and heats the plasma. LaB_6 is manufactured either in small crystals or in larger sintered shapes, the later of which was chosen for MPDX cathodes due to its large surface area and customized shape. The ceramic sintered LaB_6 pieces used in MPDX cathodes were purchased from Leybold Vacuum as a replacement part in a scanning electron microscope, and their 'shot glass' shape is ideal for efficient radiative heating.

The graphite heater is positioned coaxially inside the LaB_6 'shot glass', and nearly all of the radiated power is captured by the LaB_6 inner walls. The heat transfer efficiency is further enhanced by the relatively large emissivities of LaB_6 and graphite ($\sim$0.8). The graphite filament is ohmically heated by $\sim$1 kW of AC current, and has a resistance of 0.42-0.44 Ω at operating temperature. The filament power supply circuit is isolated both from the LaB_6 as well as from the mains circuit, so as to minimize the possibility of arcing between the discharge power supplies and mains ground. This heater power supply also allows for remote analog control of heating power using phase-controlled solid state relays, and is discussed in more detail below. The filament itself is heated to about 1700 °C, which results in a LaB_6 outer surface temperature of 1300 °C (as measured by optical pyrometer). The cathode tips glow a yellow-white color at this temperature, which is ideal for maximum current emission given the limitations of the 120 A discharge power supplies. The cathode emission curve is difficult to define in terms of temperature for a number of reasons, but in general all but the most diffuse MPDX plasmas have space-charge current limitations of 200 A or more per cathode, and so cathode current is usually limited either by their temperature or by the power supply current limit of 120 A. An increase in cathode temperature therefore leads to a roughly linear increase in cathode current. The exact relationship is complicated by the inaccuracies of measuring LaB_6 temperature *in situ*. Various efforts to anchor a high temperature tungsten-rhenium thermocouple to the cathode tip have proven ineffective, and optical pyrometer measurements are only as accurate as the combined knowledge of the cathode emissivity as well as

Figure 2.6: Two main heater filament designs. Ruler measurement is in inches. Top: five-winding design. Bottom: nine-winding design.

the optical properties of the vacuum windows. In practice, cathode temperature is controlled using a feed-forward system where the experiment operator fine tunes the heating power for each cathode to achieve the desired discharge current. The cathodes are slowly heated to emission (following an increase in heating power of 100 W per hour) at the beginning of an experimental campaign and remain at high temperature for a duration of weeks to months. This is done to limit the thermal stresses on the cathode components that occur during each heat-up or cool-down cycle. Accidental losses in heating power have been known to result in cracked LaB_6, which then requires removal and replacement.

A significant amount of research and design work went into heater filament fabrication. The main challenge involved the limited space inside each LaB_6 'shot glass', where the inner diameter is only $\sim$0.75 in. Heater filaments usually follow a 'snake' winding design in order to maximize resistance, and thus I^2R, in comparison to the rest of the heating circuit conductors. This increase in filament length is often the desirable option over a decrease in cross-sectional area because the

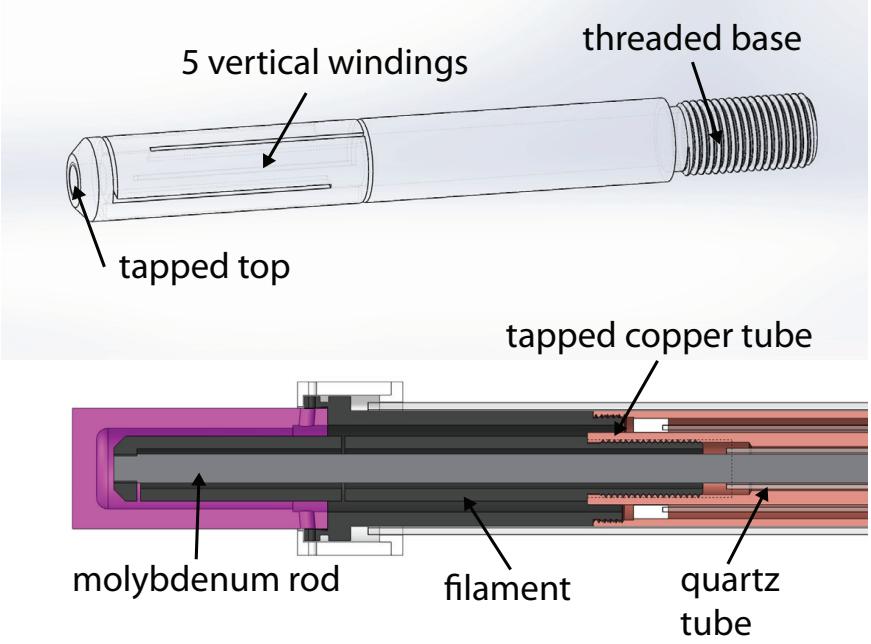

Figure 2.7: SolidWorks schematics for the original five-winding filament design, and its location in the cathode assembly.

later choice can lead to increased material evaporation and a shorter component lifespan. Fitting a winding design in a thin cylindrical form, with both sides of filament anchored at the same base, was an exercise in graphite machining. Fig. 2.4 shows the final version of the filament, but this was only reached after several rounds of prototypes and feedback from experimental operation. Fig. 2.6 shows the two main heater filament designs: a five-winding design and a nine-winding design. The first two years of MPDX experiments were conducted with the vertical design, but a sufficient number of filament failures prompted a re-design.

The original five-winding design used vertical windings with electric connections at either end of the filament. The filament bottom was threaded and screwed into a copper tube, while the filament top had a tapped hole that was connected to the end of a thin molydbenum rod. The molybdenum and copper tube served at the two return paths for the heater circuit, and were insulated from each other by a quartz tube, as shown in Fig. 2.7. COMSOL Multiphysics was used to model the ohmic heating, radiative flux, and thermal expansion of the entire cathode heater circuit,

Surface temperature
Max temp = 2309.6 C (filament)
Min temp = 200 C (end of copper conductor)

Radiative heat flux
Max heat flux = 176.12 W/cm^2 (filament)

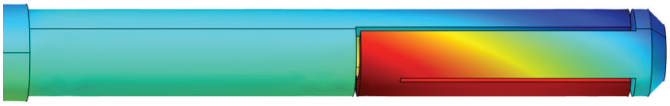

Radial thermal expansion
Max radial displacement = 0.02 in
Max axial displacement = 0.293 in

Figure 2.8: COMSOL simulations for the original filament design. Surface temperature, radiative flux, and radial displacement are shown for a total heating power of 3 kW (150 A over a 20 V DC potential drop). Total cathode thermal expansion in the axial direction was only 0.293 in, and so it was concluded that the operating heating power of 1.5 kW would lead to acceptable axial displacement.

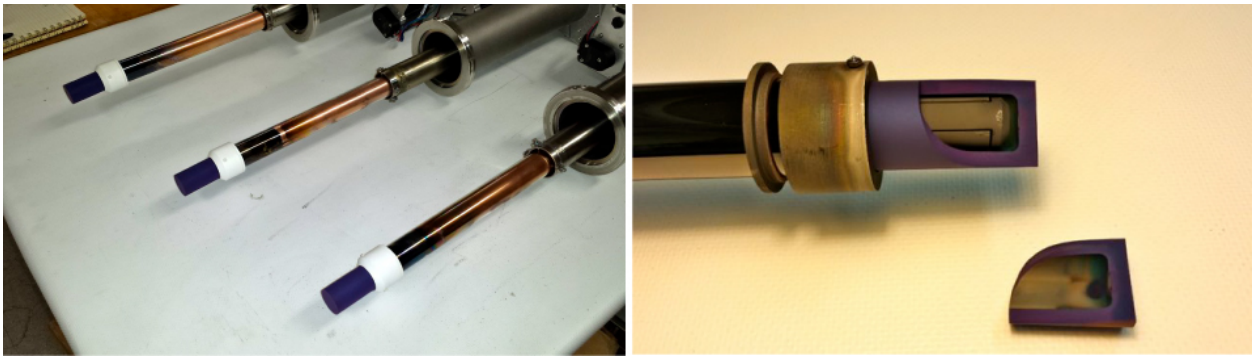

Figure 2.9: Left: LaB_6 cathode assemblies with new ceramic tips. Right: Five-winding filament inside LaB_6 tip, after cathode failure due to excessive thermal expansion.

and results are shown in Fig. 2.8. A total of eight cathodes were constructed with this filament design, and it was determined that about 1.5 kW of heater power was required to heat the LaB_6 to emission. It was discovered, however, that over time filaments would suffer from internal short circuits, leading to blown fuses and rapid cooling of the LaB_6. This rapid cooling could sometimes lead to cracks in the cathode tip, and one particularly catastrophic case is shown in Fig. 2.9. It was hypothesized that these failures were caused by adjacent filament windings coming into contact with each other due to thermal expansion. Although COMSOL modeling had suggested that the inter-winding gap was large enough to accommodate expansion, the simulations ignored the structural constraints of the filament circuit. Specifically, the center molybdenum rod that was attached to the top of the filament was not lengthening as much as the copper tube, resulting in an axial squeezing of the filament itself. The addition of a stress relieving spring tab at the base of the molybdenum rod was not enough to overcome this problem, and a new filament was designed to minimize the chance of an electrical short.

The new nine-winding filament design uses several design changes to circumvent all of these problems. First, the two electrical connections to the graphite filament are both at the filament base, allowing the top to thermally expand freely away from the fixed base. Instead of connecting to conductors with very different coefficients of thermal expansion (copper and molybdenum) the new design connects to two identical copper rods via tapped holes in the filament base (Fig. 2.4). The gaps between adjacent windings are larger, and filament heating is more uniform over the

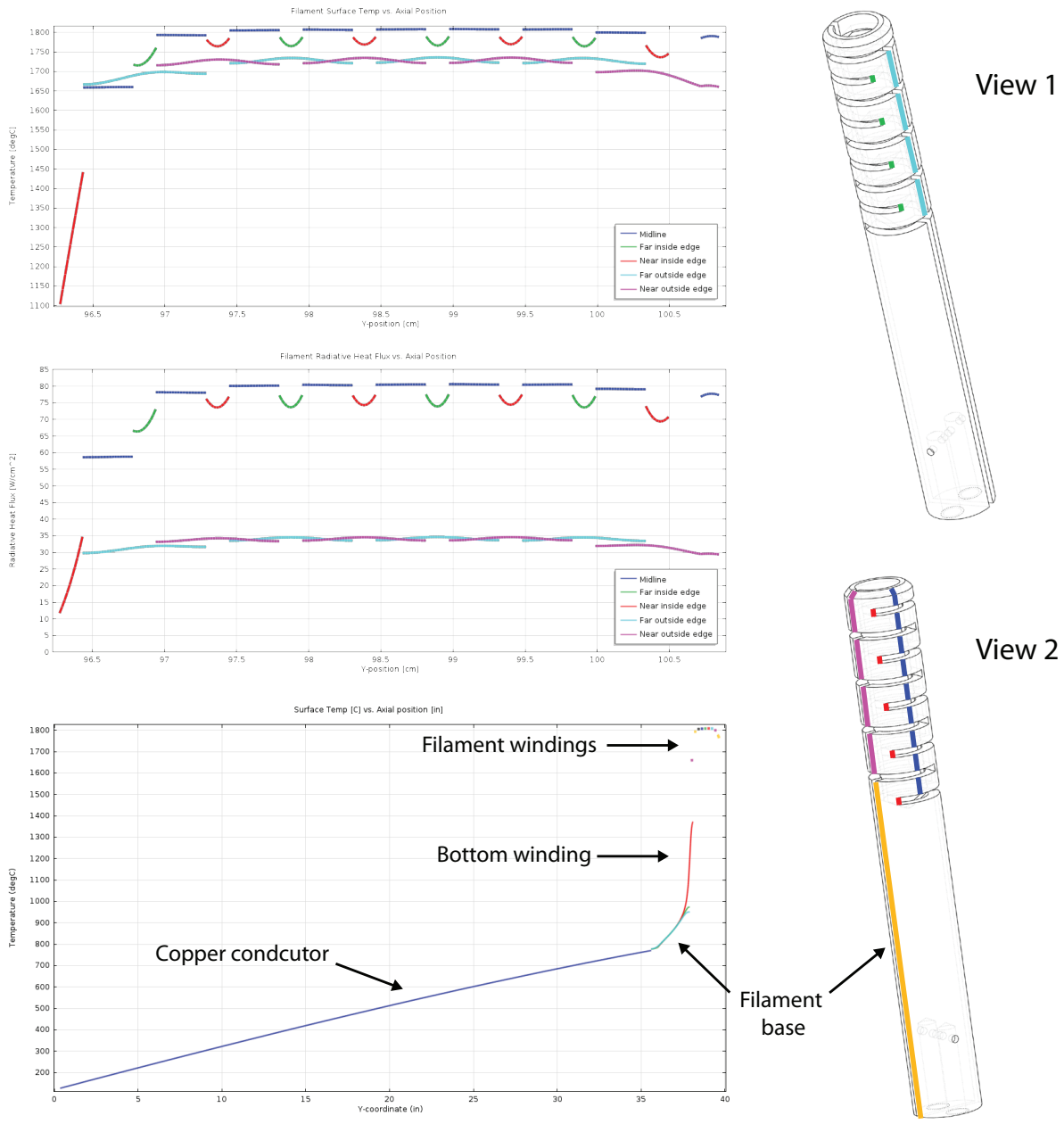

Figure 2.10: COMSOL simulations for the updated filament design. Surface temperature and radiative flux are shown at the filament tip, plotted in the axial direction along a collection of lines. The temperature of the entire heater circuit is also shown, with the base of the copper conductors kept at room temperature by the water cooling clamps.

windings, further decreasing the relative displacement due to thermal expansion. The results from a COMSOL model are shown in Fig. 2.10, showing the expected temperature and radiation flux for the typical heating power of 1.2 kW. As desired, the temperature gradient between the hot windings and the copper conductors is large enough to prevent the copper from reaching its melting point of 900 °C. The large majority of the heating power is lost via radiative flux, and only a small amount of heat needs to be removed from the copper conductor base via water cooling. Table 2.1 describes the main results from the COMSOL model, and operation has shown these numbers to be very good predictions of measured electrical resistance and required input power. This model includes the nonlinear modeling of the temperature-dependent changes in the conductivity, emissivity, and thermal expansion coefficients for both graphite and copper.

The new filament design has been incorporated into all twelve cathodes currently installed on MPDX. The LaB_6 tip is held in place by a graphite base, which in turn screws into a large copper tube that serves as both the discharge circuit conductor as well as the main structural support for the cathode tip. Since LaB_6 has the largest coefficient of thermal expansion of any of the materials used in cathode construction, maintaining a good electrical contact has been another significant design challenge. Commonly used connection techniques like surface-to-surface clamps or bolts are untenable due to this expansion mismatch combined with the cylindrical geometry of the tip; if held from the inside, the LaB_6 will expand away from the contacting surface, whereas any clamp on the LaB_6 base needs to expand just as much as the LaB_6 itself. Threading the bottom of the LaB_6, as has been done for the graphite-copper electrical connections, is not possible due to the high brittleness and hardness of LaB_6.

The solution has been to capture the expanding LaB_6 in a castle-like graphite base. This base has an inner diameter a few thousandths of an inch larger that then LaB_6 outer diameter, and the gap at room temperature is calculated to disappear at emission temperatures. In fact, to ensure a solid electrical connection and to prevent arcing, the graphite base has a series of discrete tabs that have enough flexibility to accommodate a slight *increase* in the graphite base diameter as the LaB_6 expands. This technique works very well in practice, as the LaB_6 expands to an exact fit in the graphite base and continued operation actually increases the connection as evaporated LaB_6

Boundary Conditions	Copper rod # 1 base potential	25 V
	Copper rod # 2 base potential	0 V
	Copper rod base temperature	126.8 °C
	Ambient (LaB_6) emissivity	0.8
Results	Total current	51.6 A
	Filament ohmic heating	1269.7 W
	Copper ohmic heating	7.38 W
	Filament radiation	1251.16 W
	Filament maximum temperature	1812.7 °C
	Copper maximum temperature	778.2 °C
	Conductive heat flux through copper rods	20 W
	Total resistance	0.48 Ω

Table 2.1: Main results from COMSOL modeling of the nine-winding filament heating circuit.

deposits on the graphite to fill in any residual gaps due to imperfections in the smoothness of the LaB_6 surface. The cathode tip is held in place via two alumina screws that pass through two drilled holes near the LaB_6 before anchoring in complimentary tapped holes in two of the graphite base tabs. This allows the cathode to operation in any orientation, and thus permits cathode installation anywhere on the MPDX vessel.

All the copper and graphite components in the cathode need to be shielded from the plasma, both to prevent sputtering as well as unwanted arcing to biased surfaces. At the cathode tip this is achieved using a cylindrical boron nitride shield, which covers the graphite base. The main copper tube is covered with a slightly larger quartz tube, which also provides electrical insulation from the stainless steel half-nipple that functions as the sliding vacuum o-ring surface. Like every insulator that is exposed to plasma, these insulators slowly accumulate a black coating over months of experimental operation. While the exact composition of this coating is unknown, it is hypothesized to be either sputtered molybdenum or evaporated graphite that somehow makes its way out of the confines of the LaB_6 tip. Regardless of its source, this coating has not shown to be conducting, and is easily removed during cathode maintenance using sandpaper.

The final part of the cathode assembly is the electric breakout and feedthroughs. This is located at the non-vacuum end of the assembly and allows for electrical connections to the two heating conductors and single discharge conductor. Feedthroughs are made with standard high-voltage Conflat vacuum components with copper feedthrough conductors of 3/8 in and 3/4 in OD respectively. In order to provide the heat removal that is necessary to maintain the feedthoughs at room temperature, a set of cylindrical copper clamps were designed to lock onto the end of each feedthrough. Not only do these clamps serve as water-cooled heat sinks and wire terminals, but they also act as RF clamps in anticipation of the large amount of electron cyclotron heating planned for MPDX plasmas. There is a large change in clamp diameter exactly 1/4 λ from the clamp base, where $\lambda = 3\,\text{cm}$ is the microwave wavelength used in the planned 2.54 GHz magnetron system. The addition of a grounded coaxial shield to the cylindrical clamp will create two discontinuities in the line capacitance separated by one quarter-wavelength, and will block all RF power that is

picked up by the cathode inside the vessel. As ECH has not yet been used in MPDX, it remains to be seen whether this provisional functionality is necessary for RF containment.

2.3.2 Anodes

The second part of the discharge heating system is much less complicated than the emissive cathodes described above. A set of up to twenty molybdenum anodes are inserted into the vessel and collect the electron current injected into the plasma by the cathodes. Each anode tip is similar in size and shape to the cylindrical LaB_6 tips; however unlike the hollow LaB_6 these molybdenum tips are solid. They are connected to a threaded copper rod via a tapped hole at the cylinder base, which in is connected to the positive discharge power supply terminal via an electrical feedthrough and RF clamp identical to those describes above. The copper rod makes up the bulk of the anode length, and is shielded from the plasma by an alumina tube. A stainless steel tube serves as the o-ring surface for linear motion in the radial direction.

Some care must to taken to limit the electron current drawn by each anode, as the copper rod can reach its melting temperature in extreme cases. This temperature increase does not come directly from the ohmic heating of the collected current, but instead from the impact energy carried by the collected electrons on the molybdenum surface. As copper's melting point is much lower than molybdenum's, the first point of failure is at the interface between the two metals. It is common practice in MPDX experiments to try to maximize the total anode surface area, both to lessen the individual electron heating as well as to stabilize the global plasma potential. The anodes are grounded, and are the plasma's only reference to ground, so a dearth of anode area may result in a very negative plasma potential. In some cases the global plasma potential drops to the cathode bias, which is usually hundreds of volts below ground. This not only extinguishes the plasma (as the emitted primary electrons have no accelerating electric field) but also tends to burn out any sensitive probes as well. This interested phenomenon is discussed in greater detail in Chapter,4.

2.3.3 Cathode Heater Control System

The radiative filament heaters that maintain the LaB_6 cathode tips at emission temperature are powered by custom-made AC power supplies. These power supplies were designed to meet a set of requirements specific to their application in MPDX. The main consideration in their design was to prevent arcing between the LaB_6 and the graphite filament during plasma discharges. Initial cathode operation with DC power supplies resulted in an unacceptable amount of arcing, which not only prevented a quiescent plasma shot but also damaged the DC power supplies through internal shorting to ground. To fix this issue, the graphite filaments obviously had to be isolated from the mains ground as well as from the LaB_6 itself. This was accomplished using a step-down transformer that reduces the 120 VAC mains voltage to $\sim$25 V, an appropriate level for the 0.4 Ω filament resistance.

A second design requirement is remote control of the power supply output voltage. Considering the amount of power sent to the heater filaments and the high temperatures reached during operation, it is desirable when starting at room temperature to slowly increase the heating power over an extended period of time. This slow heat-up cycle usually lasts several hours and prevents damage to the cathode components caused by thermal shock; that is, stress caused by a steep gradient in the thermal expansion that overcomes the material strength. Autotransformers are a common way to dial up the amplitude of an AC signal, and can be remotely controlled using motors; however the relatively large amount of current needed for these heater circuits pose a problem. Autotransformers with current ratings above 20 A are large and expensive, and power loss to conductor heating can be substantial. A set of twelve power supplies (one for each cathode) that used autotransformers to control the power output would take up a significant amount of space and produce a large amount of heat. An attractive alternative is to use solid state relays (SSRs). This class of high-power solid state devices is intended to handle switching waveforms with large currents and voltages, and the category of phase-controlled SSRs are specifically designed to modulate the amplitude of the output waveform based on an analog input voltage. The phase-controlled SSRs used in these heater power supplies are rated to 240 VAC and 50 AAC, both well within the expected amplitudes of the mains signal drawn on the primary side of the step-down transformer.

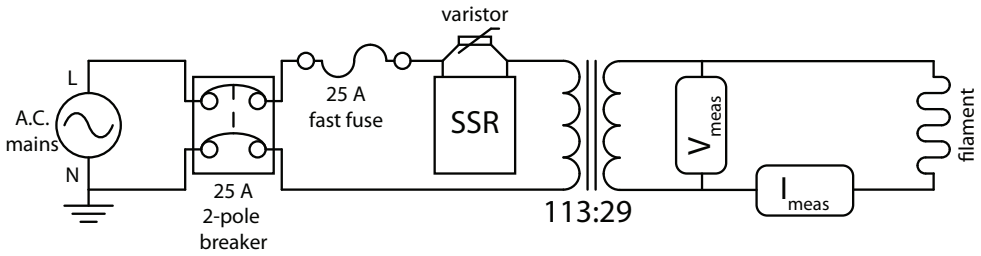

Figure 2.11: Heater power supply circuit diagram.

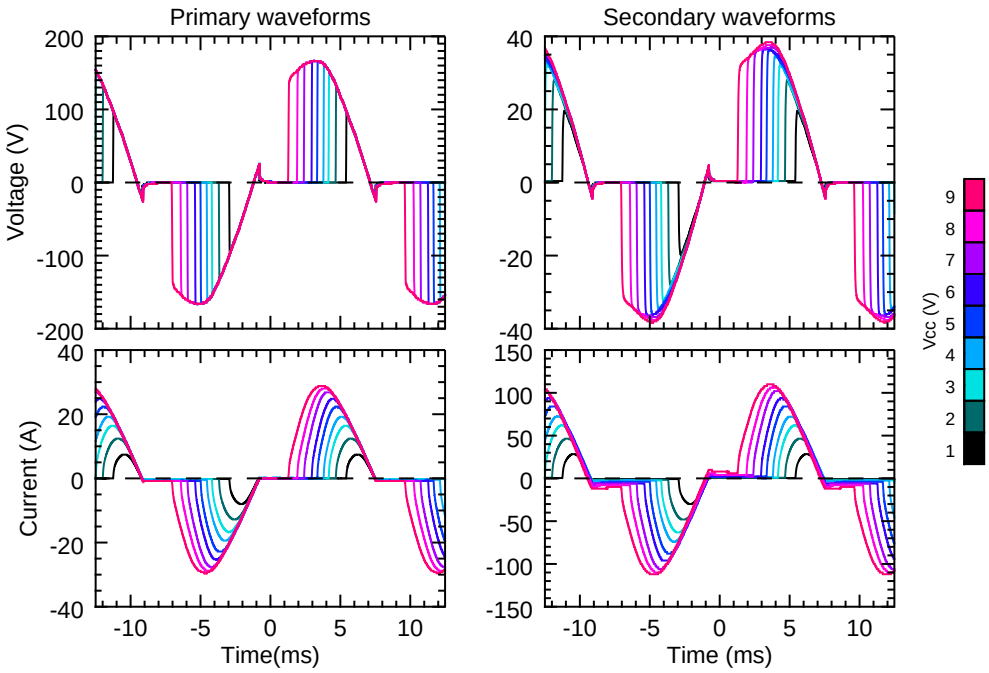

Figure 2.12: Heater power supply waveforms.

A circuit diagram of the heater power supply is shown in Fig. 2.11. The over-current and over-voltage protection prevents damage to the delicate solid state components in the SSR in the event of a short-circuit failure on the fuse or transformer saturation. Voltage and current transducers measure the heater power on the secondary side of the step-down transformer. The SSR itself is controlled via an analog 0-10 VDC input, which corresponds to a linear increase from 0% to 100% RMS power transmission. This analog control is done via synchronized switching controlled by the internal SSR circuitry. The SSR opens at every zero-crossing of the mains voltage waveform,

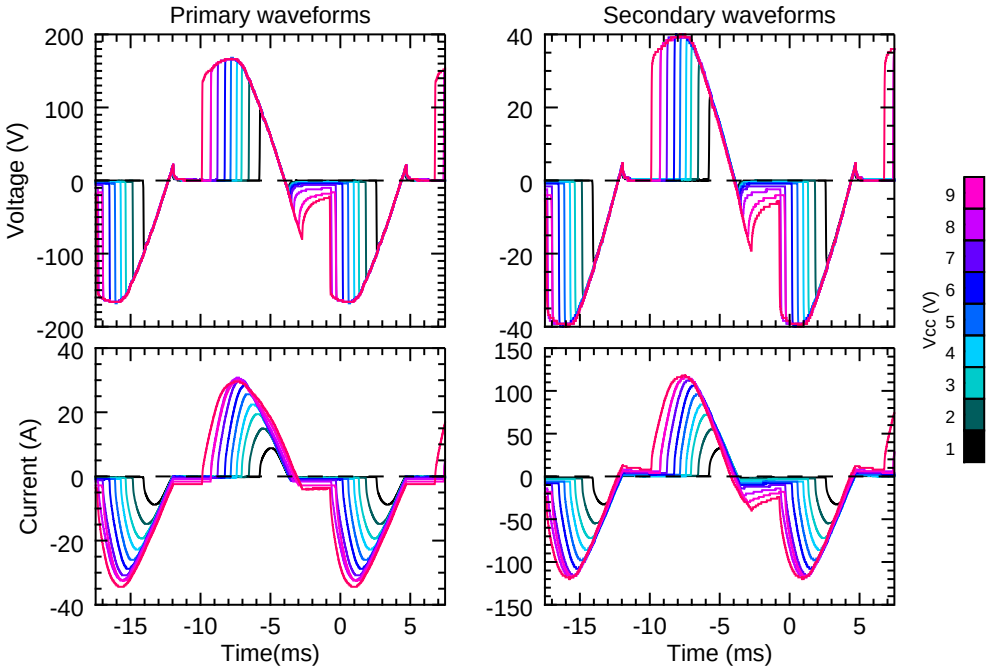

Figure 2.13: Heater power supply waveforms during SSR failure and core saturation.

and closes some fraction of the 60 Hz period later: the control voltage (Vcc) moves this closing timepoint either forward or backward in time relative to the zero-crossing. At Vcc=5 V, the relay closes exactly halfway through the waveform half-period, and so 50% of the mains RMS voltage is passed through. The entire waveform is passed through for Vcc=10 V, and the relay is permanently open for Vcc=0 V. Fig. 2.12 shows the primary and secondary voltage and current waveforms as a function of control voltage. While the primary and secondary voltage traces do indeed have a sharp turn-on point, it is important to note that the current traces do not - the leakage inductance in the step-down transformer smooths out the large dI/dt that would correspond to the large dV/dt during turn-on.

An interesting side note deals with the prototyping of these heater power supplies. The ferrite cores used for the step-down transformer were obtained from old Variac autotransformers, so that the primary windings were already wound and epoxied in place. The secondary windings were added using fewer turns of higher gauge wire. The cores originally were chosen to meet the

required Volt-seconds as estimated based on the total power supplied to the heater filament (up to 2 kW). However, initial operation led to unexpected transformer core saturation and the subsequent tripping of over-current protection on the primary side. This saturation tended to occur at an RMS volt-second threshold significantly below the core power rating. Further analysis of the waveform details showed that the transformer leakage inductance was adversely affecting SSR operation, which in turn was shifting the I-V phase and decreasing the step-down transformer efficiency. Fig. 2.13 shows the primary and secondary waveforms of a core that suffers from this problem. The voltage and current overshoots on the secondary waveforms indicates that the SSR built-in snubber circuit was not large enough to dampen the inductive back-reaction on the switching in both directions. This asymmetry in the SSR operation led to a DC offset on the transformer input, which of course will lead to core saturation if large enough. This problem was fixed by simply replacing the transformer with a larger core, one that could handle the increased flux swing added by the SSR asymmetry.

A summary of heater power supply operation is shown in Fig. 2.14. Up to 2 kW of heating power can be supplied to a $\sim 0.4\,\Omega$ filament, and power output is a linear function of control voltage (Vcc). Power supply efficiency is typically between 85% and 95%. The data points that fall below the average trend in the efficiency were measured used an undersized transformer core, which as mentioned above experienced larger-than-expected power loss due to core saturation.

2.3.4 Discharge Power Supply System

Once the cathode tips have been heated to emission temperatures, the discharge power supplies are used to draw large amounts of DC current across the MPDX vessel. Each cathode has its own DC switching power supply made by Communications & Power Industries (CPI) expressly for use within the industry of physical vapor deposition (PVD) semiconductor fabrication. These power supplies are compact yet high-powered, with maximum DC outputs of 550 V, 120 A, and 36 kW. They are also designed specifically for neutral gas ionization; the voltage output is designed to spike to more than twice the DC rating in order to break down the neutral fill gas, after which the output regulation decreases the voltage to the desired setpoint. These units are also equipped

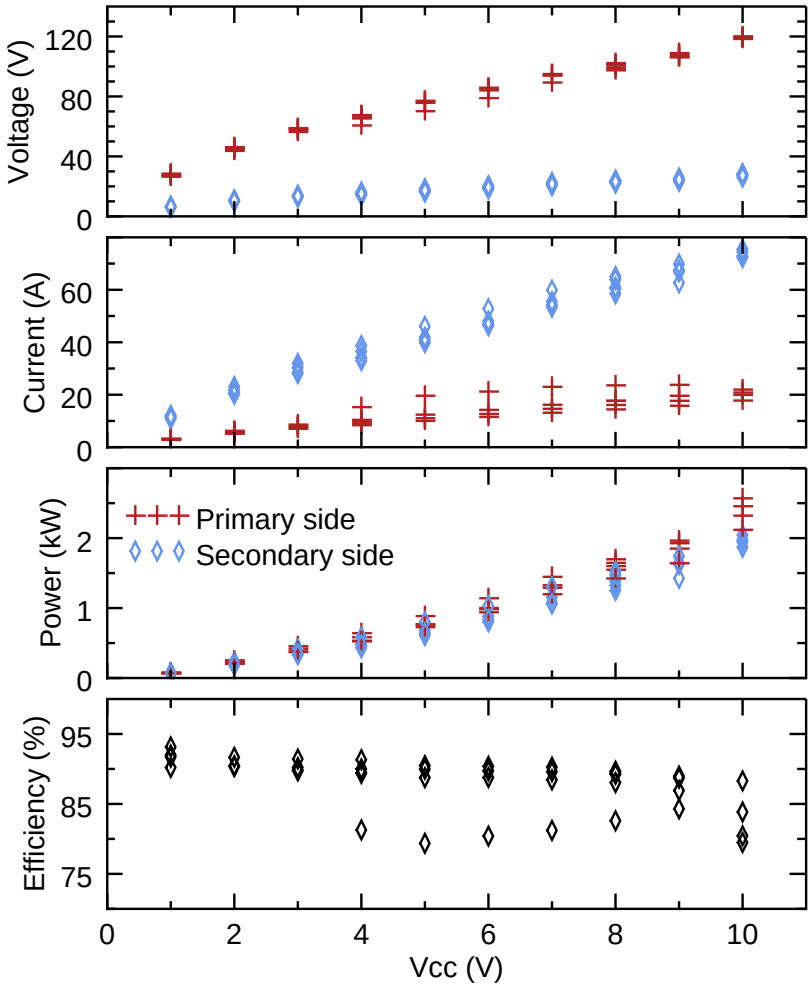

Figure 2.14: Summary of heater power supply operation for four different heater circuits. All measured values are RMS. The data points that deviate from the average trend, particularly in efficiency and primary current, are from a heater circuit with a undersized transformer.

with arc suppression, which temporarily shuts down the power output if a large change in the load resistance is detected. Overall, the CPI switching power supplies are nicely suited for steady-state plasma heating, and are the integral component in the MPDX discharge power system.

Because the discharge power supplies are controlled via serial communication protocol, the turn-on and turn-off of all twelve units is difficult to synchronize. The typical jitter can be up to

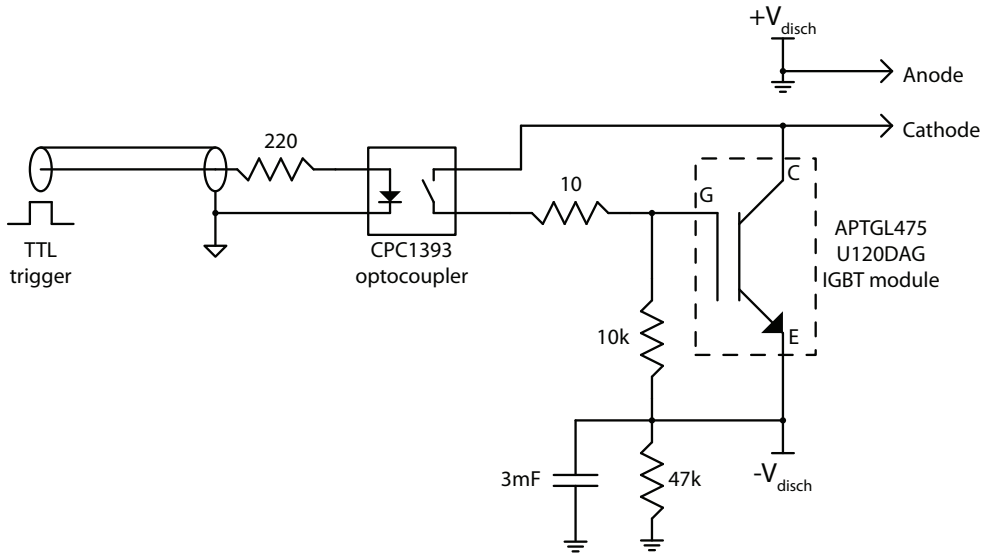

Figure 2.15: Discharge power circuit diagram. The CPI power supply terminals set the voltage rails $\pm V_{disch}$. Not shown: transducers measuring cathode voltage and discharge current.

100 ms, which can significantly affect shot-to-shot repeatability. In order to better synchronize the unit turn-on times, an array of high-power IGBT modules have been installed. These modules are used to apply the bias voltage to the cathodes with time resolution accurate to several hundred nanoseconds, and are controlled by a bank of optocoupled TTL triggers. The timing of the triggers is managed by a National Instruments FPGA module, which is also used to set the master clock for the data acquisition boards located around the experimental lab area. Fig. 2.15 outlines the circuit diagram for a single discharge power supply circuit. The 3mF filter capacitor bank is used to eliminate the 360 Hz mains noise that is otherwise present in the power supply voltage output, and which can reach amplitudes approaching 50% of the output DC setpoint. With these capacitors in place, the power supply AC ripple is less than 1% of the DC level.

2.4 Plasma Diagnostics and Data acquisition

Fig. 2.16 shows the digitized timetraces of two typical plasma discharges. An extensive suite of diagnostics are used to measure a large number of plasma parameters; for example, the traces on these plots combine probe data, mm-wave interferometer data, cold cathode vacuum gauge data,

(a) Helium plasma discharge

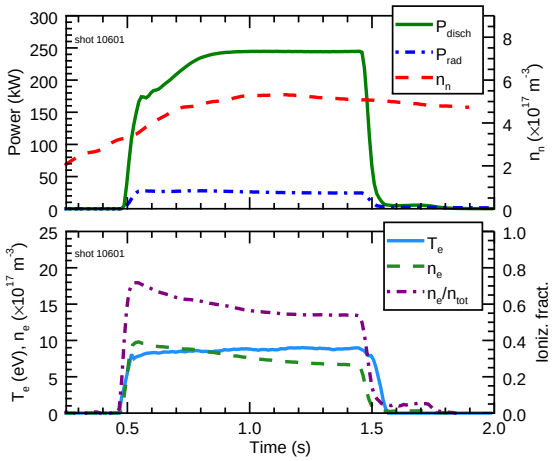

(b) Argon plasma discharge

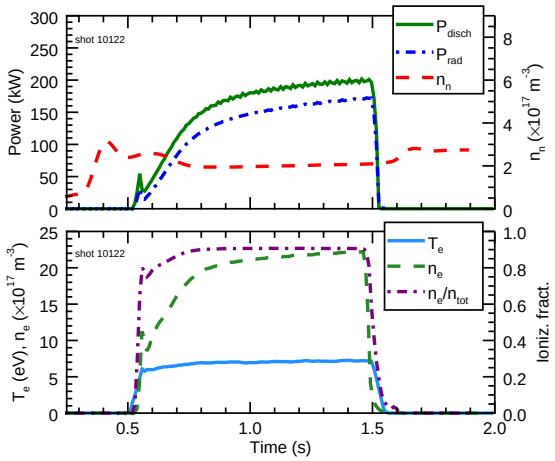

Figure 2.16: Parameter timetraces of typical high-power helium and argon plasma discharges in MPDX.

bolometer data, and data from voltage and current transducers on the discharge circuit conductors. This section will serve as an outline of this diagnostic suite so that the experimental results presented in following chapters can focus on the physics instead of the hardware details.

2.4.1 Langmuir and Mach probes

One of the most important measurements made on MPDX involves the global geometry of plasma parameters. Probe measurements made at many different latitudes provide a description of the plasma pressure and flow over the entire poloidal plane. A large number of probes will increase the angular resolution of this global dataset, and so an array of ten motor-controlled linear probes were constructed. One such probe is shown in Fig. 2.17, detailing the combination Langmuir/Mach tip, the installation locations on the MPDX vessel, and the motorized linear stage. The initial results discussed in this section have been published in Physics of Plasmas and the Journal of Plasma Physics [33, 34].

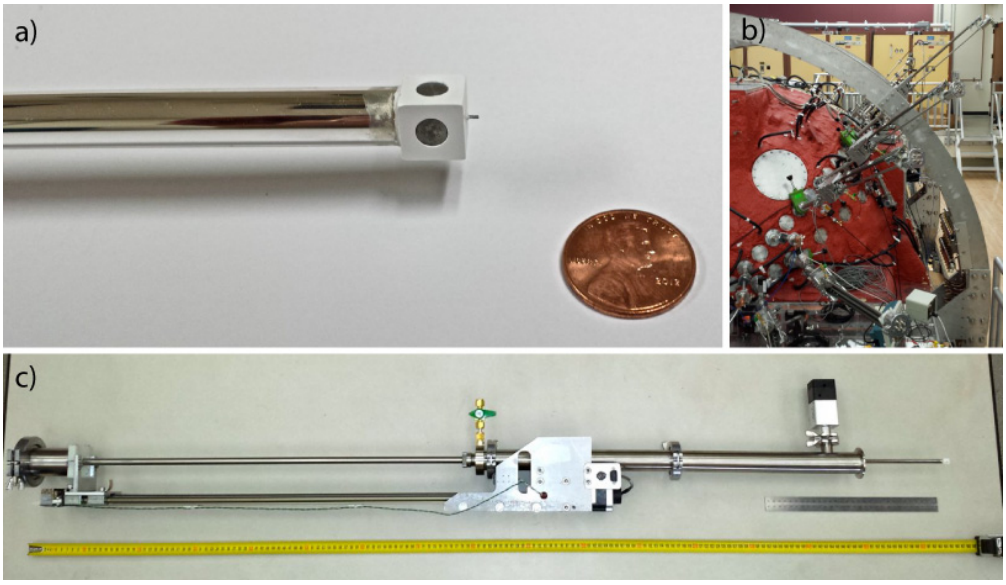

Figure 2.17: Combination Langmuir/Mach probe array. a) Close-up of probe tip, showing two Mach faces and the Langmuir pin tip. b) Location of 6 installed probes on MPDX vessel. c) Entire motorized linear probe stage; each 4-ft long probe can be inserted to a radial position of $r = 85$ cm.

Each probe tip consists of two independent Mach probes (each composed of two ion-collecting molybdenum planar faces) and one Langmuir probe (~ 2 mm long molybdenum wire). The cube-shaped boron nitride tip allows for the four Mach faces to measure ion flow in two orthagonal directions, which are oriented in the toroidal ($\hat{\phi}$) and poloidal ($\hat{\theta}$) directions. The Langmuir tip measures the local T_e, n_e, and floating and plasma potentials, using a triangle-wave swept bias at 400 Hz. This provides the local ion acoustic speed, which in combination with the Mach number measurements produces measurements of two components of the absolute ion velocity. Normal operation is to calibrate the Mach probe measurements before and after a linear scan, using well-established Mach probe theory. Calibration consists of a set of identical plasma shots taken with the probe tip rotated 180° between shots; this corrects for any error due to differences in the Mach face collection areas, which can change over time thanks to sputtering and plasma deposition.

One major obstacle to extensive probe operation in MPDX is the plasma heat load to the probe surface. MPDX plasma are dense enough such that more than 10 seconds of plasma exposure is enough to damage probe components, specifically the internal copper wiring and ceramacast

binding agent used in construction. Even short shot lengths can damage probes if the operation duty cycle is large enough. Probes are designed to minimize overheating through several design features. The probe shaft is made with copper tube so that heat conduction to the room-temperature electrical feedthrough end is as large as possible, and this copper is shielded from plasma sputtering by a quartz tube. A thin layer of silver is chemically deposited on the interior of the quartz so that rational from plasma as hot cathodes is reflected instead of absorbed by the probe shaft. Overall, these probes have proven to be very reliable in diagnosing the global plasma parameters.

A unique two-axis motorized probe stage has been used on MPDX to map out 2D data planes at the plasma edge. A CAD schematic of this is shown in Fig. 2.18. The two-axis articulation is possible thanks to an innovative ball joint vacuum seal, wherein a precisely machined 3 in diameter stainless steel ball joint is held in place by a matching socket with two differentially pumped o-ring seals. The probe can sweep out a solid angle of 0.84 sr, corresponding to a maximum angle of 30° from the normal unit vector.

2.4.2 mm-wave interferometer

The reliable measurements of core electron density presented throughout this thesis are obtained using the MPDX mm-wave heterodyne mm-wave interferometer. This non-invasive diagnostic uses mm-wave radio frequency (320 GHz) beams to measure the line-averaged n_e through the plasma bulk via wave phase shifts. Analog mixers generate an intermediate frequency of $\sim$ 1 MHz that is phase shifted as it propagates through the plasma. Typical MPDX densities of $10^{11} - 10^{12}\,\mathrm{cm}^{-3}$ result in a phase shift of several fringes (one fringe corresponds to a 2π shift between the reference and plasma beams). This shift is measured at a high time resolution so that the fast turn-on and turn-off dynamics can be adequately tracked. A high speed FPGA is programmed to digitally compute this shift using a simple comparator operational amplifier, yielding a time resolution of $10^{10}\,\mathrm{cm}^{-3}$ per microsecond. The less accurate Langmuir probe measurements of bulk plasma density are calibrated using the output of this diagnostic.

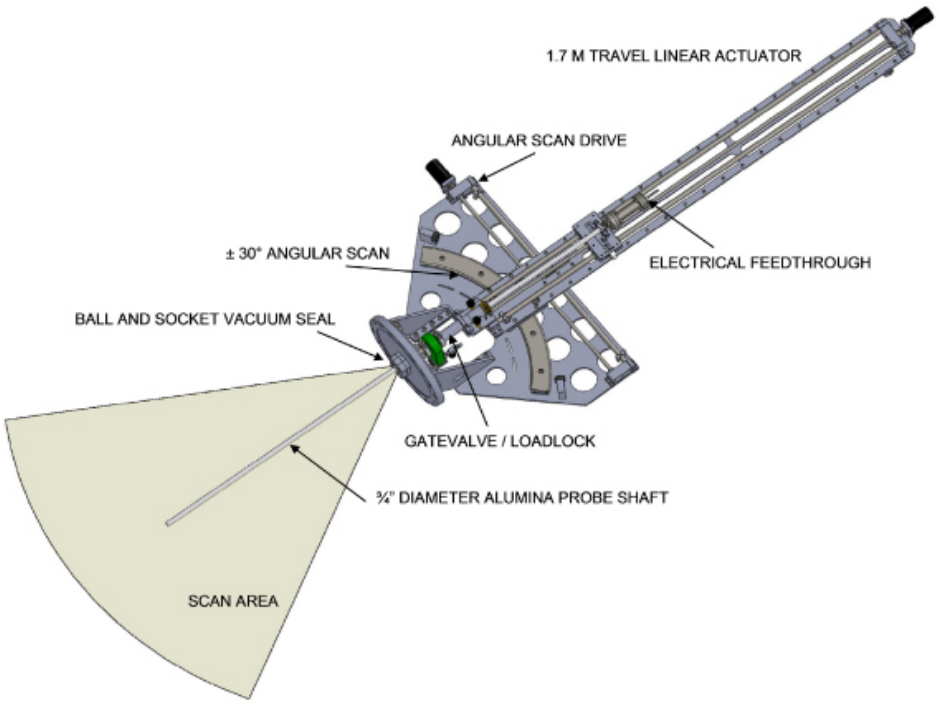

Figure 2.18: CAD schematic of the two-axis sweep probe. The ball and socket vacuum seal allows the probe axis to be rotated up to 30 degrees from normal in any direction. Remotely controlled stepping motors and digital encoders facilitate precise probe operation.

2.4.3 Fabry-Perot spectrometer

Doppler shifted line emission is measured using a Fabry-Perot spectrometer, and provides a core T_i measurement for MPDX plasmas. Plasma light is passively collected at a specific ion emission line ($\lambda = 488\,\text{nm}$ in argon, $\lambda = 468.6\,\text{nm}$ in helium) and is sent through a precision etalon, which creates a ring pattern of interference fringes. Each fringe is integrated in the angular direction to obtain a high-resolution image of the ion emission line. This technique, called ring summing, can greatly increase the signal to noise and allows exact fits to determine emission line broadening [35]. The typical resolution of ion temperature measurements is $\pm 0.05\,\text{eV}$, but the required integration time is on the order of several seconds, meaning that only one core T_i is

obtained for each plasma shot. This diagnostic could also be used to measure bulk ion flow, with a theoretical velocity resolution of ± 10 m/s, but this feature has yet to be realized on MPDX.

2.4.4 Additional non-invasive diagnostics

Several other non-invasive diagnostics are used to passively measure MPDX plasmas. Several survey spectrometers are used to measure neutral and ion emission in the visible spectrum. Spectra are continuously captured with exposure times ranging from 2-200 ms, depending on the gas species and line intensity. These spectrometers have been used to diagnose plasma impurities as well as to measure the neutral burn-out. Varying the impact parameter of the collimated line-of-sight has produced radial profiles of neutral emission, which have been used to benchmark neutral penetration depths and characterize the difference in burn-out between the plasma edge and core regions.

A pyrometric bolometer is used to measure the total power radiated by MPDX plasmas. These measurements are used as a comparison to power balance predictions based on atomic radiation rates. Argon plasmas in particular are limited by the large fraction of radiated power, resulting in lower electron temperatures relative to helium discharges.

2.4.5 Data acquisition and analysis

All probe diagnostics, as well as voltage and current transducers on electrode power connections, are digitized using D-tAcq 96-channel ADC boards. These digitizers are 16 bit per channel with 500 kSamples per second throughput, and have true differential input for each channel. The results presented in this thesis were acquired using four 96-channel boards that were synchronously driven by a 1 MHz FPGA-controlled external clock (the same clock used in the mm-wave interferometer phase detection). Raw data is written to a local MDSplus hierarchical database.

Raw data is analyzed using IDL code written specifically for MPDX experiments. An second MDSplus process tree stores the analyzed Langmuir and Mach data for each plasma shot, as well as a collection of processes timetraces from every other installed diagnostic. Both MDSplus databases are remotely accessible using the built-in client/server model. Data is also logged to a

SQL database, both to note the initial conditions before every plasma shot as well as to continuously log (on a per minute basis) the vessel vacuum conditions and cathode heating conditions.

All experimental operations are controlled via custom-made LabView code. This includes both monitoring and control of cathode heating power supplies, as well as plasma shot setup and triggering. The full suite of motorized probes and cathodes are remotely controlled using this LabView interface, and the full set of initial conditions that determine each discharge are set and logged to SQL with every plasma shot. This includes neutral fill level, cathode voltage and current setpoints, data acquisition rates (for DAC boards, interferometers, and spectrometers), and all the timing associated with cathode bias turn-on and turn-off. A shot timer can be enabled to automatically trigger a preset number of plasma shots, which is especially useful when conducting a series of probe scans with many radial points. A set of web cameras maintain a visual link between the control room and the MPDX experimental room.

Chapter 3

Measurements of cusp plasma losses and comparison to a quasi 1D transport model

Understanding plasma confinement is an essential component of high magnetic Reynolds number experiments on MPDX. High plasma density, temperature, and ionization fraction are prerequisites to any experiment investigating flow-driven MHD instabilities, and the details of the ring cusp confinement scheme will ultimately determine how best these parameters can be achieved. Historically, so-called 'magnet-bucket' devices have been useful in exploring fundamental plasma physics mainly because of their steady-state operation at low densities and temperatures, allowing precise probe measurements of plasma phenomena like sheaths and double-layers [36, 37, 38]. These experiments had very short particle confinement times and had ionization fractions much smaller than unity. The highly-ionized, high energy-density parameter regimes that MPDX plasmas inhabit are quite far removed from previous 'magnetic-bucket' research, and so previous work on cusp confinement and transport needs to be looked at from this new perspective.

Confinement research on MPDX has covered several areas, including both measurements and modeling of cusp transport. This chapter will present novel surface probe measurements of the plasma flux through the magnetic cusp to wall, and will show that the measured trend in confinement is not explained by the currently accepted theory. An ambipolar diffusive transport theory is presented, and a corresponding numerical model is described that offers a better explanation of the MPDX cusp measurements. Finally, the diamagnetic and $\mathbf{E} \times \mathbf{B}$ drifts predicted by the diffusive transport model are shown to be in good agreement with probe measurements of edge ion drifts. This combination of measurements and modeling brings us to the conclusion that edge transport

in MPDX, while significantly different from previous cusp confinement research, is now a well understood part of the MPDX device.

3.1 Edge transport measurements

Measurements of the plasma edge in MPDX have been made using an array of Langmuir and Mach probes, both along radial chords and across the surface of the plasma-facing limiter tiles that cover the magnet rings. In general, sharp gradients in electron density and temperature are measured at the plasma edge. Fig 3.1 shows an average Langmuir probe scan in radius between magnet rings. The electron temperature and density are uniform within the unmagnetized core of the plasma, and the edge gradient covers a radial extent of about 10 cm. The cusp field maintains a vacuum gap of about 10 cm between the very edge of the plasma and the vessel wall. The measurements are fitted by error functions that accurately characterize the sharp transition from the homogeneous core to the magnetized edge, indicating that electron temperature gradients are about half as large as electron density gradients. This data actually is an average of eight probes at eight different magnet ring latitudes, showing that the radial location of the plasma edge is spherically symmetric.

In addition to one dimensional probe scans, two dimensional scans have also been taken at the plasma edge. Fig. 3.2 shows a 2D plane that was mapped out by a Langmuir probe in a helium plasma using a novel ball-joint vacuum seal probe design. The locations of the MPDX wall and two closest magnet rings are shown, as well as the constant flux surfaces of the vacuum magnetic field as measured by a Hall probe array. Both density and temperature contours follow lines of constant ψ, indicating that the cross-field transport in the cusp field is much slower than parallel field transport. Interestingly, the edge gradients of this probe scan are also about 10 cm wide, but are located further from the vessel wall in comparison to the probe scan shown in Fig. 3.1. These scans were taken for two different plasmas, and the pattern that has emerged from these and other probe scans has been that higher plasma pressures result in a smaller vacuum gap between the wall and the plasma edge. That is, plasma with higher electron temperatures and densities penetrate farther into the cusp magnetic field.

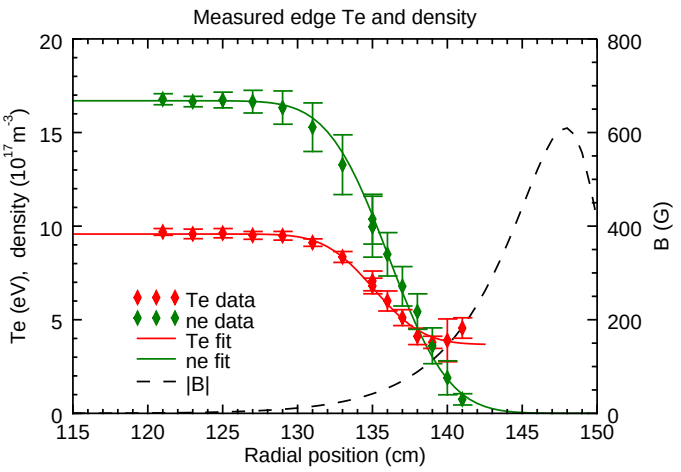

Figure 3.1: Average Langmuir probe measurements of electron temperature and electron density at the plasma edge. Measurements are a weighted average of eight probes distributed across eight unique latitudinal locations, and error bars indicate variation among probes. Error function fits accurately characterize the edge gradients, and the vacuum B field is shown for comparison.

Because cross-field transport is observed to be strong enough to hold back plasma from the wall between magnet rings, the only way plasma can be lost to the wall is *along* field lines to the ceramic tiles that cover the surfaces of the magnet rings. This results in a visible burn line that forms down the center of each magnet ring. Fig. 3.3 shows a surface Langmuir probe diagnostic designed to measure the parallel plasma flux to the wall, with the cusp burn line tracing the region of highest flux along the center of the magnet ring. This probe array consists of twenty tungsten wires spaced across the cusp width, where each tip is biased with a swept voltage in order to measure the local electron density, temperature, floating and plasma potentials. The array as a whole measures the cusp as a Gaussian-like distribution in most plasma parameters, with the center values matching measurements made by Langmuir probes inserted past the edge into the homogeneous core. This further confirms the assumption that temperature and density are constant along field lines, as the very center of the cusp is connected to the plasma core. With each probe position farther from the cusp center measuring lower plasma pressure, it appears that there is a one-to-one matching between the distance across the cusp and the distance along a radial probe chord. With sufficiently

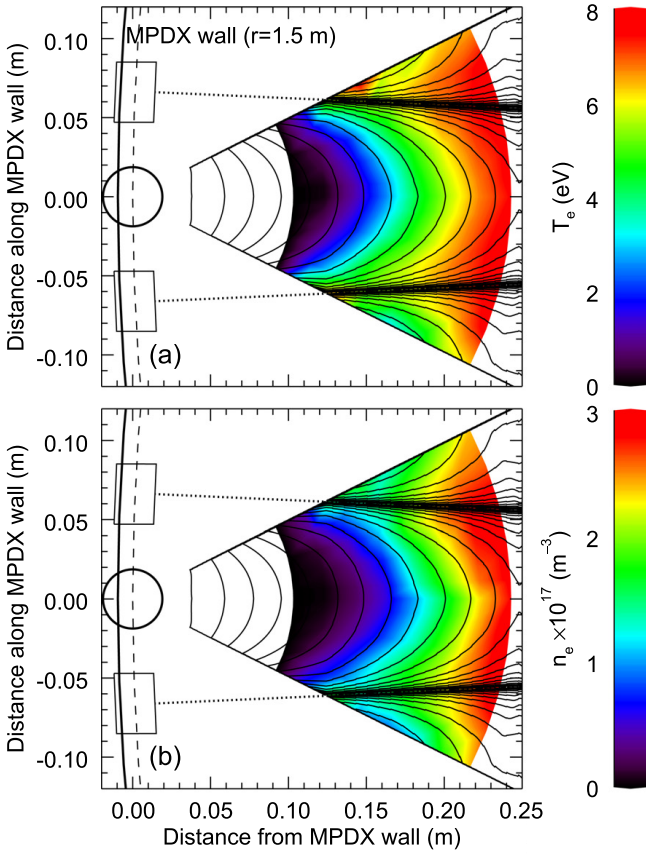

Figure 3.2: Langmuir probe measurements of electron temperature and electron density in the poloidal plane near the plasma edge. Overlaid solid black lines indicate contours of constant vacuum magnetic field as measured bu Hall probes. The vacuum vessel wall and two closest magnet rings are shown, as well as the ball-joint vacuum seal about which the 2D probe was rotated.

accurate knowledge of the cusp magnetic field, a radial 1D probe scan can be used to reconstruct the plasma parameters on the magnet face, and therefore becomes an indirect measurement of the cusp width itself.

As mentioned above, previous experimental research on the cusp loss width of a 'magnetic bucket' device has been conducted at much lower plasma pressures and ionization fractions. These studies have suggested a variety of cusp width scalings, with the most widely reported loss width

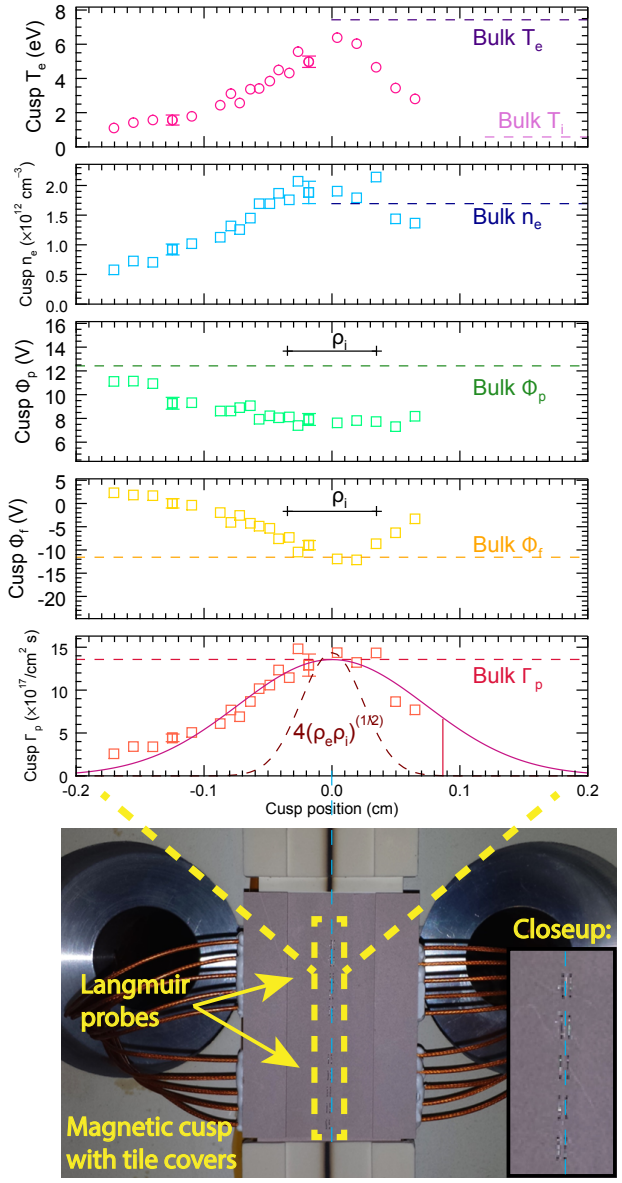

Figure 3.3: Embedded Langmuir probes in a specially-made alumina limiter, used to measure parallel plasma flux to the wall. Measured parameters in the cusp center match probe measurements in the plasma core, indicating that the open magnetic surfaces are also surfaces of constant Te, ne, and floating potential. Furthermore, the measured cusp width is significantly wider than the theorized hybrid gyroradius scaling. The cusp burn line is wider on adjacent tiles that have been in the machine for a much longer time.

being proportional to the hybrid gyroradius $w = \sqrt{\rho_e \rho_i}$ [39, 40, 41, 42]. Using the measured field strength at the magnet limiter surface of 3500 G, this corresponds to a loss width that is significantly smaller than what the embedded Langmuir probes measure. Fig. 3.3 shows the hydro gryoradius using the measured tile Te and core Ti, and this prediction is at least twice as small as the measured loss width.

Loss width measurements were taken over a large range of neutral fill pressures and discharge input power, which corresponds to a similarly large scaling in electron density, electron temperature, and ion temperature. The parameter space covered by this data set is shown in Fig. 3.4, which also shows the measured cusp widths compared to the hybrid gyroradius theory; the dashed line has a slope of 1. It is apparent that the measured widths are uniformly wider than what the theory predicts, and there is no obvious offset or similar scaling that could be attributed to systematic errors in diagnostic measurements. Fig. 3.5 shows a more detailed break-down of the scaling of the measured cusp width: while argon plasma loss widths appear to scale with n_n and n_e and inversely with T_e, helium plasma loss widths do not have any immediately obvious scaling. Neither does either species' loss width have any discernible scaling with T_i.

The global plasma particle balance is very sensitive to the total loss area available to particles free-streaming along open field lines to the wall, and so it would be very useful to have a predictive theory for the cusp loss width as a function of core plasma parameters. The next two sections will cover the formulation of a diffusive transport theory in the MPDX cusp geometry and will apply that theory to these measurements. As will be seen, the result is a much better description of the observed losses and, though it fails to perfectly fit the data and leaves out what may be important non-linear physical contributions to collisional transport, opens the door for further research into this transport problem.

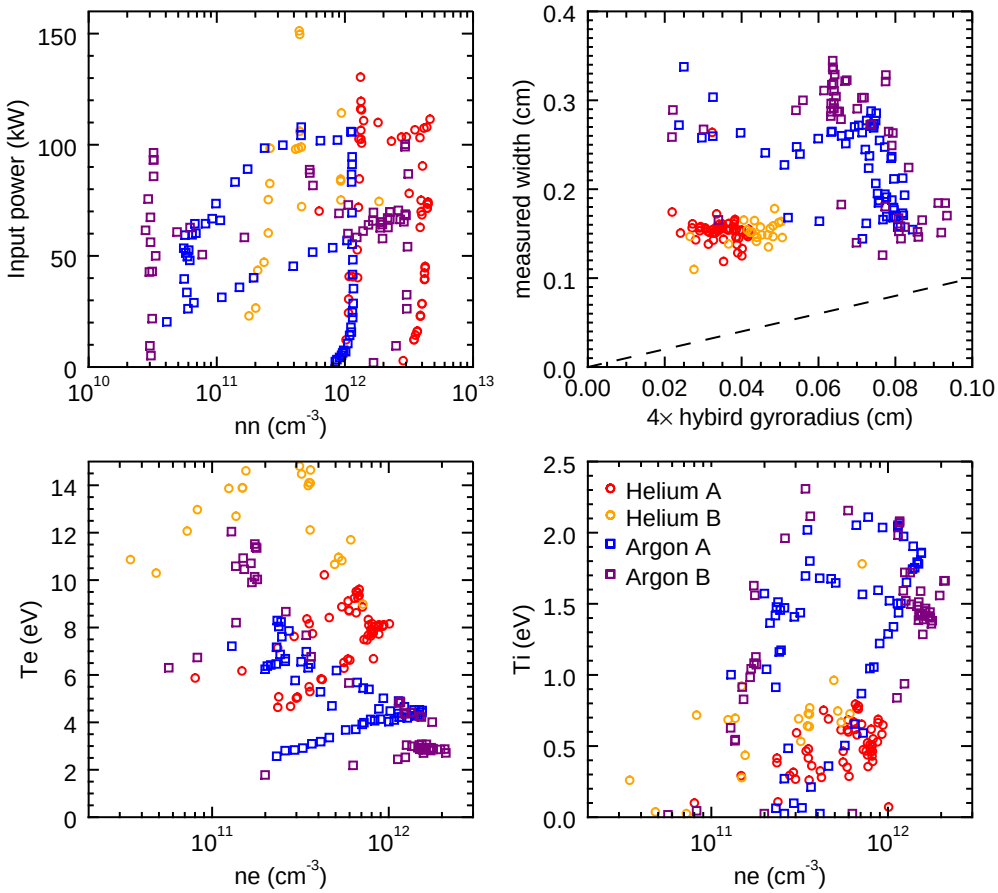

Figure 3.4: Summary of the embedded Langmuir probe data set. The main device input controls (neutral fill density and input power) were varied over a large range, spanning two orders of magnitude for both variables. Two data sets (A and B) were taken for both Helium and Argon, and are colored to help identify where either power or neutral density was held constant while the other input control was varied. The width measurements are shown in comparison to the hybrid gyroradius theory; the dashed line has a slope of 1.

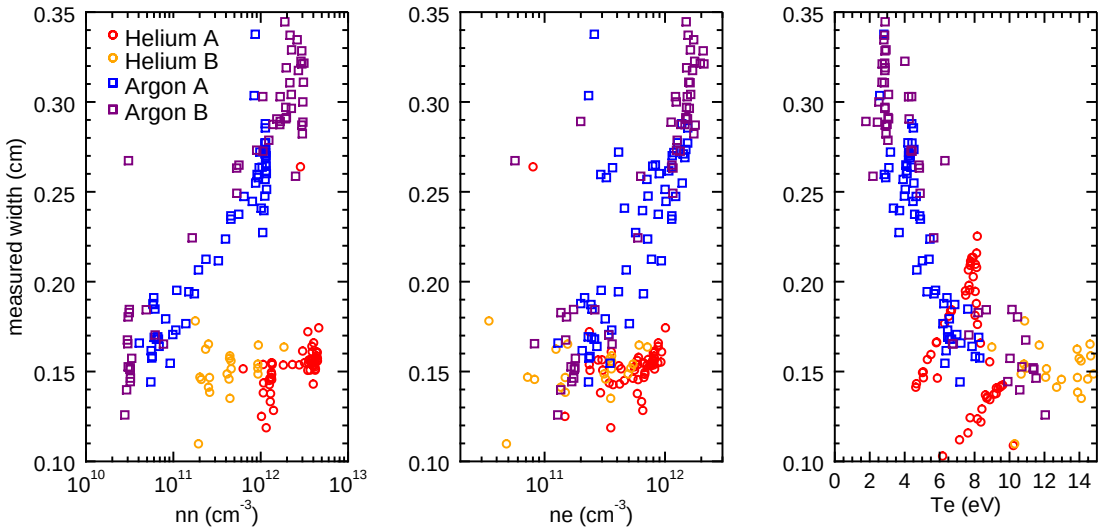

Figure 3.5: Measured scaling the cusp loss width as a function of neurtal fill density, electron density, and electron temperature. Argon plasmas can be sustained at lower fill pressure and lower Te due to the smaller ionization potential and larger radiative power loss, respectively, in comparison to helium.

3.2 Ambipolar diffusive transport theory

The cusp loss width is a poorly understood variable in the calculation of particle confinement, and an accurate transport model should properly predict the cusp loss width over a large range of plasma parameters. What should this transport model look like?

First, the model should reflect the strong magnetic field gradients that characterize the confinement in MPDX. The plasma volume can be divided into two regions: an unmagnetized core and a magnetized edge, and plasma transport is handled very differently depending on the region in question. If we start with the assumption that transport is a diffusive process, and that the lack of plasma current allows for an ambipolar treatment, then we should define a generalized diffusion coefficient that is true for both regions. This treatment follows the approach in Olson 1964 [43]. Starting with the two-fluid MHD momentum equations (in steady-state),

$$0 = Zen_i(\mathbf{E} + \mathbf{v}_i \times \mathbf{B}) - kT_i\nabla n_i - n_i m_i \nu_{ie}(\mathbf{v}_i - \mathbf{v}_e) - n_i m_i \nu_{in}\mathbf{v}_i \tag{3.1}$$

$$0 = -en_e(\mathbf{E} + \mathbf{v}_e \times \mathbf{B}) - kT_e\nabla n_e - n_e m_e \nu_{ei}(\mathbf{v}_e - \mathbf{v}_i) - n_e m_e \nu_{en}\mathbf{v}_e \tag{3.2}$$

where a constant T_i and T_e has been assumed. Since diffusion will be limited primarily by the presence of a magnetic field, we can solve these equations for a cross-field diffusion coefficient $D_\perp$. This requires the consideration of perpendicular fields and flows, which in the ambipolar limit reduce to

$$\nabla n_e/n_e = \nabla n_i/n_i = \nabla n/n \tag{3.3}$$

$$v_{e\perp} = v_{i\perp} = v_\perp \tag{3.4}$$

$$\mathbf{E} = E_\perp \tag{3.5}$$

In the axisymmetric MPDX geometry, these parallel and perpendicular unit vectors do not have components out of the poloidal $(r-\theta)$ plane. We solve this system of two momentum equations for the velocity components $v_\perp$, $v_{e\phi}$, and $v_{i\phi}$ and the ambipolar electric field, and obtain an equation for the cross-field flux,

$$\Gamma_\perp = -D_\perp \nabla n = -\frac{D_a}{1+\beta}\nabla n \tag{3.6}$$

where D_a is the classical ambipolar diffusion coefficient in a weakly ionized plasma,

$$D_a = \frac{D_e\mu_i + D_i\mu_e}{\mu_i + \mu_e} \tag{3.7}$$

$$D_e = \frac{kT_e}{m_e\nu_{en}}, \qquad D_i = \frac{kT_i}{m_i\nu_{in}} \tag{3.8}$$

and β contains the modifications to classical diffusion due to magnetization and plasma collisions,

$$\beta = \frac{\omega_e\omega_i}{\nu_{ei}\nu_{in} + \nu_{ie}\nu_{en} + \nu_{en}\nu_{in}} \tag{3.9}$$

Eq.3.6 gives a sense of how diffusion changes between the core and edge. In the unmagnetized core, $\beta \ll 1$ and so transport reduces to the simple linear case, where diffusion is neither a function of plasma density nor magnetic field strength. We thus expect the MPDX core to be spherically symmetric with very small density gradients. In the magnetized edge, $\beta \gg 1$ and so the main impediment to plasma transport is the magnetic field, which changes strongly with radius and imposes a non-spherically symmetric geometry. Transport can also be non-linear if the plasma collision rates ν_{ei} and ν_{ie} are big enough, significantly complicating the mathematics. How many of these complications we include in the model depends on how important we expect each effect to be. Since the magnetic field is obviously the most important parameter in plasma confinement, we can start with a linear model that includes the multi-cusp magnetic geometry but ignores non-linear plasma collisions.

3.3 Linear transport model

A linear transport model will ignore the effect of plasma collisions on transport in the magnetized edge. This reduces the cross-field diffusion coefficient to the form

$$D_\perp = \frac{D_a}{1 + (\omega_e \omega_i)/(\nu_{in}\nu_{en})} \tag{3.10}$$

The next step is to use this diffusive flux in the plasma continuity equation. Again, the approach we take depends on which region we're in. In the unmagnetized core, plasma continuity follows the simple spherically symmetric form

$$\nabla \cdot \Gamma_r = nNS_p \tag{3.11}$$

$$\frac{d\Gamma_r}{dr} = -\frac{2}{r}\Gamma_r + nNS_p \tag{3.12}$$

$$\frac{dn}{dr} = -\frac{1}{D_\perp}\Gamma_r \tag{3.13}$$

where we have allowed 'cross-field' to be in the radial direction. S_p is the volumetric ionization rate, and is the only source term for plasma density (recombination is negligibly small). N is the neutral density.

This system of equations is the end result of our derivation, as they can now be used in an iterative numerical solver to calculate the plasma density as a function of radius. We could, if we wanted to, also include similar equations for the neutral flux and density, using some diffusive form for the neutral transport. It turns out that this is not always an accurate method in MPDX plasmas because neutral collision mean free paths can be much larger than the machine size, and so it can be incorrect to model the neutrals as a fluid. Specifically, room-temperature neutrals in argon plasmas tend to have very short *ionization* mean free paths but very long collision (and charge-exchange) mean free paths. In this case, argon neutrals should be modeled as ballistic particles that penetrate the plasma a short distance before being ionized. On the other hand, in helium plasmas these three mean free paths are the same order of magnitude, but collision lengths tend to be shortest and on the order of tens of cm. Thus it is also acceptable to model helium neutrals as ballistic particles with a mean free path based on ionization and charge exchange interactions. In either case, the neutral transport is spherically symmetric and uses the measurement of the neutral pressure at the vessel wall as its only boundary condition.

Overall it is probably not necessary to couple the plasma and neutral transport models, for the simple reason that the plasma density is uniform for the large bulk of the machine volume. The sharp gradient in plasma density at the edge is easily approximated as a step function for the purposes of calculating neutral sink rates, and so the neutral density profile is only a function of the core plasma density and temperature. This allows us to start our solver at the machine center with the core n and T_e and the edge N as inputs to the model and then solve for the neutral profile before iterating through the plasma differential equations. The 1D neutral profile is calculated as follows,

$$n_n(r) = A\frac{\sinh(r/\lambda_{mfp})}{r/\lambda_{mfp}}, \tag{3.14}$$

$$\lambda_{mfp} = v_{th,n}/(\nu_{iz} + \nu_{cx}), \tag{3.15}$$

$$A = \frac{n_{nR}R/\lambda_{mfp}}{\sinh(R/\lambda_{mfp})}, \tag{3.16}$$

where λ_{mfp} is the total neutral mean free path for ionization and charge-exchange collisions, $v_{th,n}$ is the neutral thermal velocity (based on room temperature $T_n = 0.025\,\text{eV}$) and n_{nR} is the measured neutral density at the wall ($r = R$). In plasmas with higher ionization rates, the neutral density will be more localized to the plasma edge.

In the magnetized edge, plasma transport is determined by the magnetic geometry. Because cross-field diffusion is much slower than parallel transport, it is possible to treat plasma density and temperature as flux functions. This agrees with 2D measurements of plasma parameters in the cusp, which show that contours of constant n_e and T_e match up very well with magnetic field lines. For a given flux surface, plasma continuity is a balance of perpendicular flux across the surface and parallel flux to the wall where the flux surface terminates. Adding the volumetric source of ionization, the total continuity equation is

$$\nabla \cdot \Gamma_\perp = -\nabla \cdot \Gamma_\parallel + nNS_p \tag{3.17}$$

A diagram of this flux continuity is shown in Fig. 3.6, overlaid with a magnetostatic simulation of the cusp vacuum field. The differential volume bordered by two adjacent magnetic surfaces

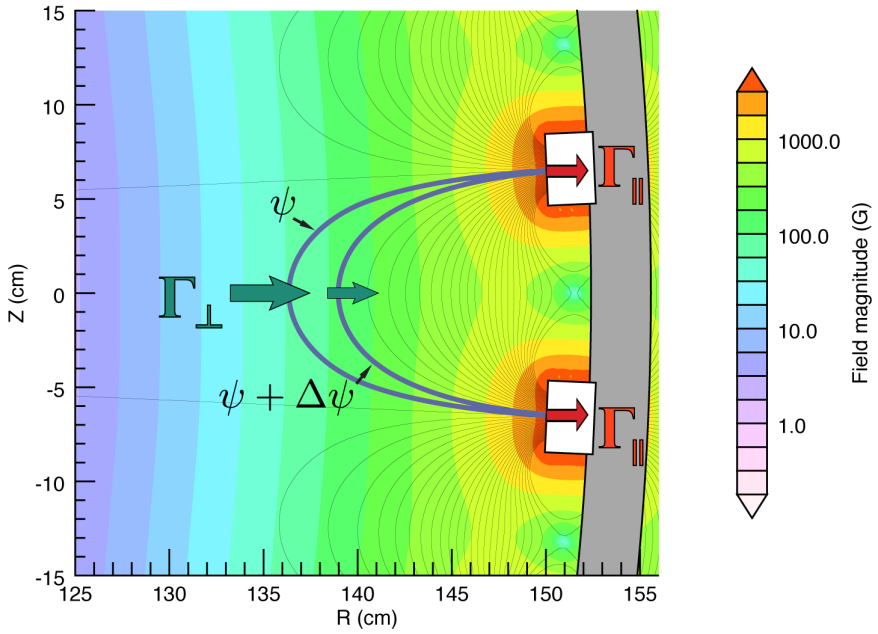

Figure 3.6: Diagram of transport equation 3.17. Plasma diffusing across the cusp field is lost through parallel flux to the magnet faces, but is replenished by ionization in the differential flux volume.

must obey particle continuity, and so cross-field diffusion and local ionization is balanced by free-streaming losses where the magnetic surfaces terminate at the magnet faces. While this parallel transport is much faster than perpendicular diffusion, the flux volume narrows to a very small loss area on the magnet face, and the divergence of $\Gamma_\perp$ will be small if the ionization source term or the differential volume is large. This is the case in the unmagnetized plasma core, but as plasma diffuses into the cusp the size of this differential flux volume decreases exponentially relative to the parallel transport loss area. Eventually the parallel losses are too great for the particle source terms, and the plasma density drops to zero.

It is essential to note that this continuity equation mixes two different curvilinear coordinate systems. The spacial divergence of the flux components is a function of the spherical geometry of MPDX, while the use of parallel and perpendicular flux components requires the identification

of magnetic surfaces and their corresponding flux coordinates. MPDX is an open-ended magnetic system because none of the magnetic surfaces in are closed; every field line terminates somewhere on the vessel wall. This is similar to a linear confinement device, but instead of a single magnetic axis MPDX is a combination of 36 axisymmetric magnetic mirrors. Nevertheless, the derivation of the appropriate flux coordinates is similar to that for a linear device and uses generic Clebsch coordinates.

Clebsch coordinates were first used in fluid mechanics to describe 3D streamlines of hydrodynamic flows. They are equally useful in plasma physics, where they represent stream functions of the magnetic field [44, 45]. The general Clebsch coordinates in MPDX are labeled by ψ and ϕ, and we can write $\mathbf{B}$ as the cross product of their gradients

$$\mathbf{B} = \nabla\psi \times \nabla\phi. \tag{3.18}$$

The magnetic field is by definition perpendicular to the ψ=constant and ϕ=constant surfaces. A magnetic surface is uniquely labeled by an appropriate measure of the magnetic flux contained within that surface, and so one of these coordinates (ψ) can be designated as the flux variable. The other is then a label for individual field lines that pass through each magnetic surface. In the axisymmetric geometry of MPDX, the flux coordinate is defined as the amount of poloidal flux contained inside a flux surface

$$\psi = \int_0^{2\pi}\int_0^{r} \mathbf{B}\cdot d\mathbf{S}, \qquad dS = r\sin\theta dr d\phi. \tag{3.19}$$

This is just the poloidal-disk flux commonly used in toroidal geometries. In terms of the magnetic vector potential A_ϕ, which is solely in the azimuthal direction, the poloidal flux is written as

$$\psi = r\sin\theta A_\phi = xA_\phi, \tag{3.20}$$

where x is the cylindrical radius. The second flux coordinate ϕ is simply the regular azimuthal coordinate, and so field lines on a flux surface are defined by their angular position around the

axis of symmetry (the $\hat{z}$ axis in cylindrical coordinates), and we can fully describe the magnetic geometry by drawing 1D field lines in the poloidal (x, z or r, θ) plane.

The third flux coordinate denotes location *along* a field line, and is usually labeled l in open-ended magnetic systems. However, it is advantageous to use a set of orthogonal coordinates, and ∇l is not necessarily perpendicular to $\mathbf{B}$. A better field line coordinate would follow the Boozer-Grad relationship

$$\mathbf{B} = \lambda \nabla \psi + \nabla \chi, \tag{3.21}$$

where the function λ is the stream function of the plasma current density

$$\mu_0 \mathbf{J} = \nabla \lambda \times \nabla \psi. \tag{3.22}$$

Since plasma current in MPDX experiments is negligibly small, this simplifies to $\mathbf{B} = \nabla \chi$, and so the third flux coordinate is defined as the magnetic scalar potential. We can still refer to a differential length along a field line in terms of dl, as well as a differential volume perpendicular to a flux surface dV, where

$$dl = B d\chi, \qquad \frac{dV}{d\psi} = 2\pi \int \frac{dl}{B} = 2\pi \int \frac{d\chi}{B^2}. \tag{3.23}$$

There are no closed flux surfaces and so these integrals are evaluated between the two endpoints of a specific field line. A diagram of the MPDX ring cusp geometry is shown in Fig. 3.7, with lines of constant ψ and χ shown in relation to the vessel wall and the two magnet rings on either side of the machine equator ($\theta = \pi/2$).

Now that we have established the appropriate magnetic coordinate system for the ring cusp geometry in MPDX, we can continue to evaluate the particle continuity equation. We evaluate the flux-surface average of each term in Eq. 3.17 and take advantage of Green's theorem to express the surface-averaged parallel flux as a line integral around the circle traced out by the foot point of a flux surface on the vessel wall

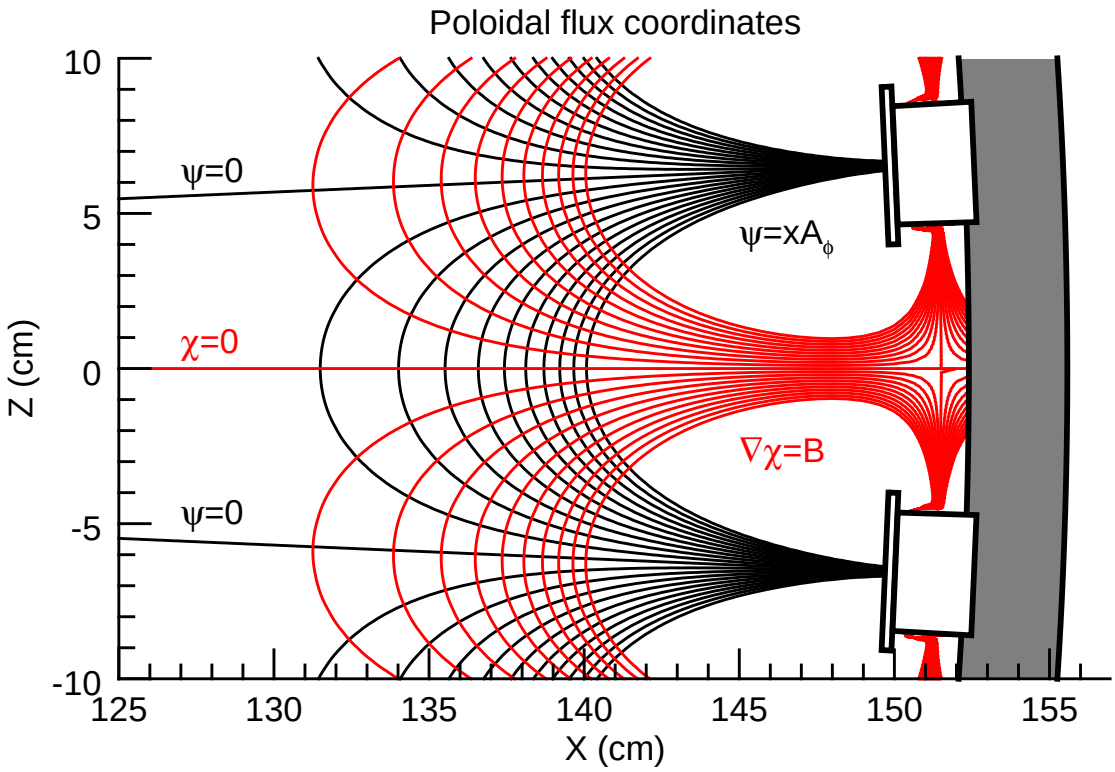

Figure 3.7: Poloidal cross-sectional view of flux coordinate system. The region covered by the constant ψ contours matches the typical location of the plasma edge gradient, with electron density dropping to zero at ~ 142 cm on the radial chord bisecting magnet rings ($z = 0$ cm).

$$\langle \nabla \cdot \mathbf{\Gamma}_\perp \rangle = -\langle \nabla \cdot \mathbf{\Gamma}_\parallel \rangle + \langle n N S_p \rangle \tag{3.24}$$

(3.25)

$$\frac{d\psi}{dV} \iint_{S(\psi)} (\nabla \cdot \mathbf{\Gamma}_\perp) \frac{dS}{B} = -\frac{d\psi}{dV} \iint_{S(\psi)} (\nabla \cdot \mathbf{\Gamma}_\parallel) \frac{dS}{B} + \frac{d\psi}{dV} \iint_{S(\psi)} n N S_p \frac{dS}{B} \tag{3.26}$$

(3.27)

$$\iint_{S(\psi)} (\nabla \cdot \mathbf{\Gamma}_\perp) \frac{dS}{B} = -\oint_{s_\phi} (\mathbf{\Gamma}_\parallel \cdot \hat{\mathbf{n}}) \frac{ds_\phi}{B} + \iint_{S(\psi)} n N S_p \frac{dS}{B} \tag{3.28}$$

where $dS = dl ds_\phi$ and $ds_\phi = r \sin\theta d\phi$. The parallel flux at the vessel wall is simply the plasma flux falling into a classical Bohm sheath,

$$\oint_{s_\phi} (\mathbf{\Gamma}_\parallel \cdot \hat{\mathbf{n}}) \frac{ds_\phi}{B} = \frac{0.6 \cdot 2\pi}{B_{max}} n c_s r_f \sin\theta_f \tag{3.29}$$

where r_f and θ_f are the coordinates of the foot point of the flux surface, c_s is the ion acoustic speed in that flux surface, and B_{max} is the magnetic field strength at the magnet face.

The remaining integrals in Eq. 3.28 are also simplified through the use of the flux functions n, $\partial n/\partial\psi$, and $\partial^2 n/\partial\psi^2$. The end result is a set of 1D differential equations in radius, similar to the unmagnetized core transport equations. The main difference, reflecting the change in symmetry from spherical to flux surface, is a set of coefficients that incorporate the effects of the complex edge magnetic geometry. We start by expanding the perpendicular flux divergence,

$$\nabla \cdot \mathbf{\Gamma}_\perp = \nabla \cdot (-D_\perp \nabla n) = -D_\perp \nabla^2 n - \nabla n \cdot \nabla D_\perp \tag{3.30}$$

$$\begin{aligned} &= -\frac{D_\perp}{r^2}\left(2r\frac{\partial n}{\partial r} + r^2\frac{\partial^2 n}{\partial r^2} + \cot\theta\frac{\partial n}{\partial\theta} + \frac{\partial^2 n}{\partial\theta^2}\right) \\ &\quad - \frac{\partial D_\perp}{\partial r}\frac{\partial n}{\partial r} - \frac{1}{r^2}\frac{\partial D_\perp}{\partial\theta}\frac{\partial n}{\partial\theta} \end{aligned} \tag{3.31}$$

and converting the density polar derivatives into flux derivatives so they can be pulled out of the integral. Since all flux functions are constant along field lines, the partial derivatives are only dependent on ψ ($\partial/\partial\chi = 0$ along a field line),

$$\frac{\partial n}{\partial\alpha} = \frac{\partial\psi}{\partial\alpha}\frac{\partial n}{\partial\psi} \tag{3.32}$$

$$\frac{\partial^2 n}{\partial\alpha^2} = \left(\frac{\partial\psi}{\partial\alpha}\right)^2 \frac{\partial^2 n}{\partial\psi^2} + \frac{\partial\chi}{\partial\alpha}\frac{\partial^2\psi}{\partial\chi\partial\alpha}\frac{\partial n}{\partial\psi} \tag{3.33}$$

where $\alpha = r, \theta$ and

$$\frac{\partial \psi}{\partial r} = -B_\theta r \sin\theta \tag{3.34}$$

$$\frac{\partial \psi}{\partial \theta} = B_r r^2 \sin\theta \tag{3.35}$$

$$\frac{\partial \chi}{\partial r} = B_r \tag{3.36}$$

$$\frac{\partial \chi}{\partial \theta} = r B_\theta \tag{3.37}$$

In this linear transport model, $D_\perp$ is not a function of density and so can be explicitly calculated for any location (r, θ), as can its derivatives. Organizing the terms in the surface integral of $\nabla \cdot \Gamma_\perp$, we see start to see the form of the final equation emerge:

$$\begin{aligned}\int \nabla \cdot \Gamma_\perp \frac{dS}{B} = &-\frac{\partial^2 n}{\partial \psi^2} \int D_\perp \left((\partial_r \psi)^2 + \frac{(\partial_\theta \psi)^2}{r^2} \right) \frac{dS}{B} \\ &- \frac{\partial n}{\partial \psi} \int D_\perp \left(\frac{2\partial_r \psi}{r} + \partial^2_{\chi,r}\psi B_r + \frac{\cot\theta}{r^2}\partial_\theta \psi + \partial^2_{\chi,\theta}\psi \frac{B_\theta}{r} \right) \frac{dS}{B} \\ &- \frac{\partial n}{\partial \psi} \int \left(\partial_r \psi \frac{\partial D_\perp}{\partial r} + \frac{\partial_\theta \psi}{r^2} \frac{\partial D_\perp}{\partial \theta} \right) \frac{dS}{B}\end{aligned} \tag{3.38}$$

where terms like $\partial_r \psi$ and $\partial^2_{r,\chi}\psi$ have been used as shorthand for the terms defined in Eq. 3.34-3.37.

Now that all density-dependent terms have been moved outside the flux surface integrals, the polar-to-flux coordinate operations can be reversed to rewrite the perpendicular flux divergence as a function of the radial derivatives of plasma density,

$$\frac{\partial n}{\partial \psi} = \frac{\partial r}{\partial \psi}\frac{\partial n}{\partial r} + \frac{\partial \theta}{\partial \psi}\frac{\partial n}{\partial \theta} = \frac{1}{\partial_r \psi}\frac{\partial n}{\partial r} \tag{3.39}$$

$$\frac{\partial^2 n}{\partial \psi^2} = \left(\frac{\partial r}{\partial \psi}\right)^2 \frac{\partial^2 n}{\partial r^2} + \frac{\partial \theta}{\partial \psi}\frac{\partial}{\partial \theta}\left(\frac{\partial r}{\partial \psi}\frac{\partial n}{\partial r}\right) = \frac{1}{(\partial_r \psi)^2}\frac{\partial^2 n}{\partial r^2} \tag{3.40}$$

The θ derivatives in the above expressions are dropped because we choose to evaluate them along a radial chord that *bisects* the adjacent magnet rings. This corresponds to the $\chi = 0$ surface shown in Fig. 3.7, and is a natural axis of symmetry for any particular ring cusp. Note that this surface is not always tangent to the $\hat{r}$ direction. At higher latitudes, the overall cylindrical symmetry

of the magnet rings starts to exert more influence than the spherical symmetry of the vessel, and $\chi = 0$, $\psi = 0$ surfaces will not longer contain radial chords. However, this approximation is valid near the vessel equator, which is where these calculations are targeted. This will also match the 1D probe measurements that are made by the scanning Langmuir/Mach probe array.

The final form of the left-hand side of Eq. 3.28 in terms of plasma density is

$$\int \nabla \cdot \Gamma_\perp \frac{dS}{B} = A_0 \frac{\partial^2 n}{\partial r^2} + A_1 \frac{\partial n}{\partial r} \tag{3.41}$$

where

$$A_0 = -\frac{1}{(\partial_r \psi)^2} \int D_\perp \left((\partial_r \psi)^2 + \frac{(\partial_\theta \psi)^2}{r^2} \right) \frac{dS}{B} \tag{3.42}$$

$$A_1 = -\frac{1}{\partial_r \psi} \int \left[D_\perp \left(\frac{2\partial_r \psi}{r} + \partial^2_{\chi,r} \psi B_r + \frac{\cot\theta}{r^2} \partial_\theta \psi + \partial^2_{\chi,\theta} \psi \frac{B_\theta}{r} \right) + \partial_r \psi \frac{\partial D_\perp}{\partial r} + \frac{\partial_\theta \psi}{r^2} \frac{\partial D_\perp}{\partial \theta} \right] \frac{dS}{B} \tag{3.43}$$

For the linear diffusion coefficient given in Eq. 3.10, the spherical symmetry of the neutral profile allows for the r and θ derivatives can be explicitly written as

$$\frac{\partial D_\perp}{\partial r} = \frac{D_a}{(1+\beta)^2} \left(\frac{\beta - 1}{N} \frac{dN}{dr} - \frac{2\beta}{B} \frac{\partial B}{\partial r} \right) \tag{3.44}$$

$$\frac{\partial D_\perp}{\partial \theta} = -\frac{2\beta D_a}{(1+\beta)^2} \frac{1}{B} \frac{\partial B}{\partial \theta} \tag{3.45}$$

where, as stated above, $\beta = \omega_e \omega_i / (\nu_{in} \nu_{en})$ is a function of the magnetic geometry and the neutral density profile. In order to avoid the added complication of solving heat transport equations, the electron and ion temperature gradients are assumed to be constant fractions of the density gradient. This is motivated by the radial cusp measurements, which show that throughout the plasma edge ∇T_e is always about one-half as large as ∇n_e.

This is a good step towards a final set of differential 1D transport equations, but we'd like to express Eq. 3.41 without any second derivatives, and it's more intuitive to write the left-hand side

of the continuity equation in terms of the perpendicular flux, which when evaluated on a probe chord is just the radial flux,

$$\int \nabla \cdot \mathbf{\Gamma}_\perp \frac{dS}{B} = C_0 \frac{\partial \Gamma_r}{\partial r} + C_1 \Gamma_r \tag{3.46}$$

where

$$C_0 = -\frac{A_0}{D_\perp} \tag{3.47}$$

$$C_1 = \frac{A_0}{D_\perp^2}\frac{dD_\perp}{dr} - \frac{A_1}{D_\perp} \tag{3.48}$$

This finally lets us write a set of 1D differential equations for the radial plasma flux and density along a probe chord:

$$\frac{d\Gamma_r}{dr} = -\frac{\Gamma_r}{L_0} + n(\nu_s - \nu_l) \tag{3.49}$$

$$\frac{dn}{dr} = -\frac{\Gamma_r}{D_\perp} \tag{3.50}$$

The flux-averaged coefficients in the continuity equation are L_0, the geometric length scaling, ν_s, the ionization source rate, and ν_l, the convective parallel loss rate to the magnet surface, and are defined as

$$L_0 = \frac{C_0}{C_1} = \frac{A_1}{A_0} - \frac{1}{D_\perp}\frac{dD_\perp}{dr} \tag{3.51}$$

$$\nu_s = \frac{1}{C_0}\int N S_p \frac{dS}{B} \tag{3.52}$$

$$\nu_l = \frac{1.2\pi}{C_0 B_{max}} c_s r_f \sin\theta_f \tag{3.53}$$

Eqs. 3.49 and 3.50 are a set of ordinary differential equations for the radial plasma flux and density along a radial probe chord between two magnet rings. The coefficients defined above are flux-averaged functions of the vacuum magnetic field and the neutral density profile, and can be calculated for any plasma using only the homogeneous core plasma parameters as inputs.

In evaluating the integrals in Eqs. 3.47-3.48, it is important to note that the flux coordinate l is the length along the field line starting at the *midpoint* between magnet rings. At most latitudes (excluding the one or two rings closest to the poles where the normally periodic cusp field geometry is affected by the small magnet ring diameter) this coincides with the radial probe chord, which is defined as $l = 0$ in flux coordinates. The integral limits are from $l = 0$ to $l = L$, where L is the total field line length from the probe chord to the magnet face. We could just as easily integrate across the entire field line from magnet face to magnet face, but we would then have to double the parallel flux term since there are now two field line foot points. This thesis chooses to use the first option; all field line integrals are from 0 to L.

Given that the magnetic vector field, magnetic flux, and neutral radial profile is known, the numerical evaluation of these integrals further requires the parametrized equation for a large number of field lines in the edge region. The field line equation is

$$dl = \sqrt{dr^2 + r^2 d\theta^2} = \sqrt{dx^2 + dz^2} \tag{3.54}$$

where x and z are the cylindrical coordinates for radial and axial displacement. Cylindrical coordinates are convenient to use both for simplicity and because the vacuum magnetic field is calculated using cylindrical coordinates. Integrating this line element yields the field line length as a function of the chosen independent variable. For example,

$$l(z) = \int_0^z \sqrt{1 + \left(\frac{dx}{dz}\right)^2}\, dz, \qquad \frac{dx}{dz} = \frac{-B_x}{B_z - \psi/x^2} \tag{3.55}$$

This numerical integration is carried out using the 4th order Runga-Kutta method [46], with iteration completed when the field line reaches the magnet face radius. The tabulated array of l and corresponding r, θ positions can then be used to calculate the known fields and solve the integrals derived above. The endpoint of the l solution will not be exactly at the magnet face, and so the integration is allowed to proceed slightly farther and then the l value exactly at the magnet face is interpolated.

The transport model defined by Eq. 3.49 and Eq. 3.50 is numerically integrated using the 4th order Runga-Kutta method, with a modified shooting method used to determine the correct initial

values. Integration begins at the radial location $r = 120\,\text{cm}$ with n set equal to the measured core density. Γ_r is the shooting variable, and a root-finding routine calculates the correct initial value of plasma flux that satisfies in the desired edge boundary conditions: namely, that n and Γ_r are equal to zero at the same radial location. This boundary condition is both physically intuitive and numerically convenient, and a unique radial edge is efficiently found for every combination of core plasma parameters values. The resulting radial profile in n and Γ_r can then be transformed to obtain the flux profile across the width of the magnet face, using the fieldline tracing described above. This flux profile is fit to a Gaussian curve in the same way the measured cusp width was determined by a similar fitting routine, and although the modeled profile is not exactly Gaussian this allows a direct comparison between the embedded probe measurements and the model results.

3.4 Linear model results

The results of this numerical simulation of plasma transport through the MPDX cusp are in good agreement with probe measurements. Fig. 3.8 shows two typical cases of a helium and an argon simulation. The three terms in the continuity equation sum to give the radial profile of the flux gradient, and show that losses to the magnet face become more and more important as plasma diffuses further into the cusp field. The ionization source term is also important, and can even have a maximum value within the cusp if the neutral density profile drops off fast enough, as is the case with many argon plasmas. The effect of flux conservation begin constrained by the cusp geometry is small in comparison. The actual density and flux profiles are a good qualitative match to what is measured in the plasma edge, as all simulations show that the plasma density drops to zero between $r = 135$ and $r = 145\,\text{cm}$. The cross-field flux reaches a maximum value in the middle of the edge gradient region and then decreases as parallel plasma losses outweigh the ionization source term.

The localization of plasma ionization to the edge region of argon plasmas leads to an interesting feature of this ambipolar transport model: inward plasma flux. This is evidenced by negative values of Γ_r at radial positions inside of the maximum in $\nu_s n$, and is a necessary result of the confluence of the sharp gradients in both plasma and neutral density. This solution is allowed in the MPDX system because the core plasma has direct access to a large loss area, provided by the inserted

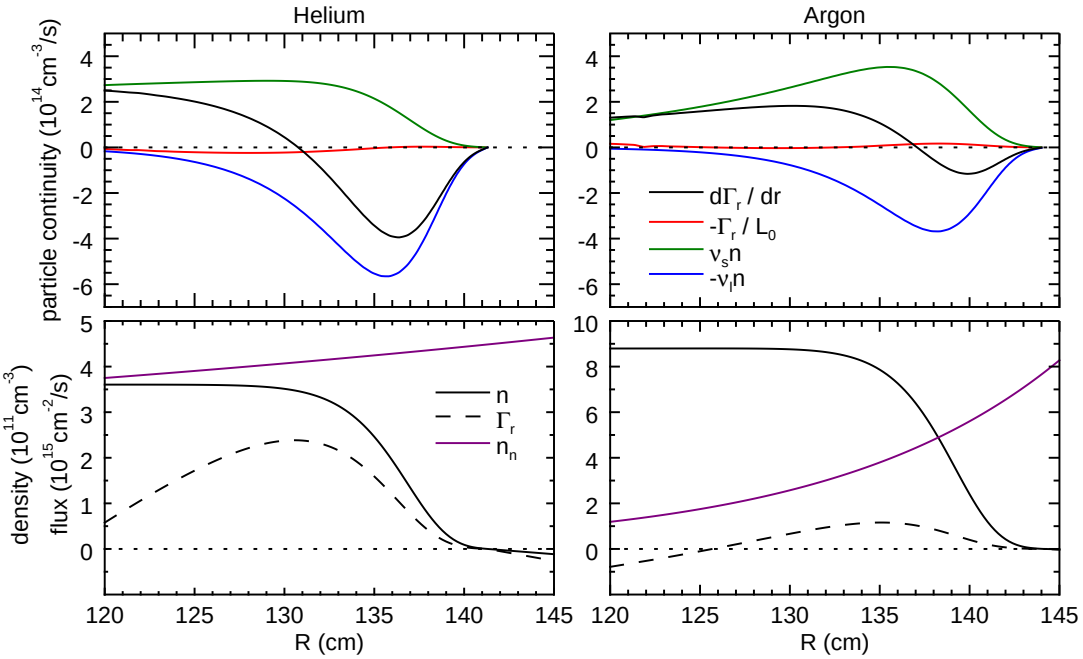

Figure 3.8: Numerical model results for typical helium (left) and argon (right) plasmas. The top plots show the radial profiles of the terms in the continuity equation, while the bottom plots show the resulting plasma density and flux, as well as the input neutral density profile.

anodes and probes. These are usually positioned at a radial location of less than $r = 120\,\text{cm}$, and so provide a second loss mechanism that helps balance the hollow ionization profile and maintain a homogeneous unmagnetized core.

The cusp width calculations based on these density profiles are shown in Figs. 3.9 and 3.10. In general, simluations with higher density in the plasma core lead to larger cross-field flux into the cusp and a larger cusp loss width. A similar trend is seen for neutral density (measured at the wall), where the increase in cross-field flux is a product of the increased ionization rate. Conversely, the simulations of plasmas with larger electron temperatures tend to have smaller cusp loss widths, most likely due to the increase in parallel flux into the Bohm sheath at the magnet faces. The modeled radial profiles for a selection of differing core plasma parameters is shown in Fig. 3.11, where it is apparent that increasing the core density will produce a radial edge closer to the vessel

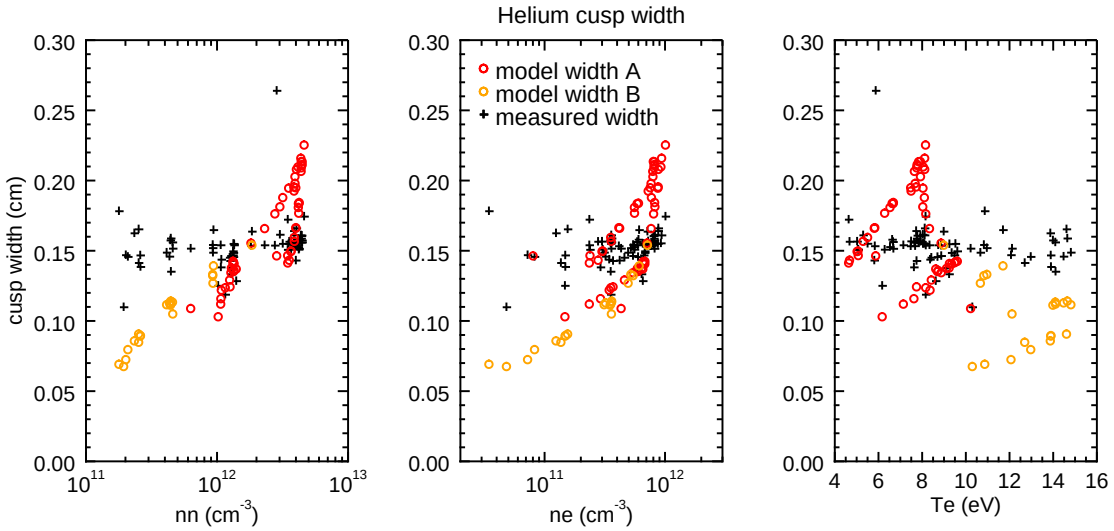

Figure 3.9: Simulated cusp loss width for helium plasmas. The embedded tile probe measurements are shown for comparison.

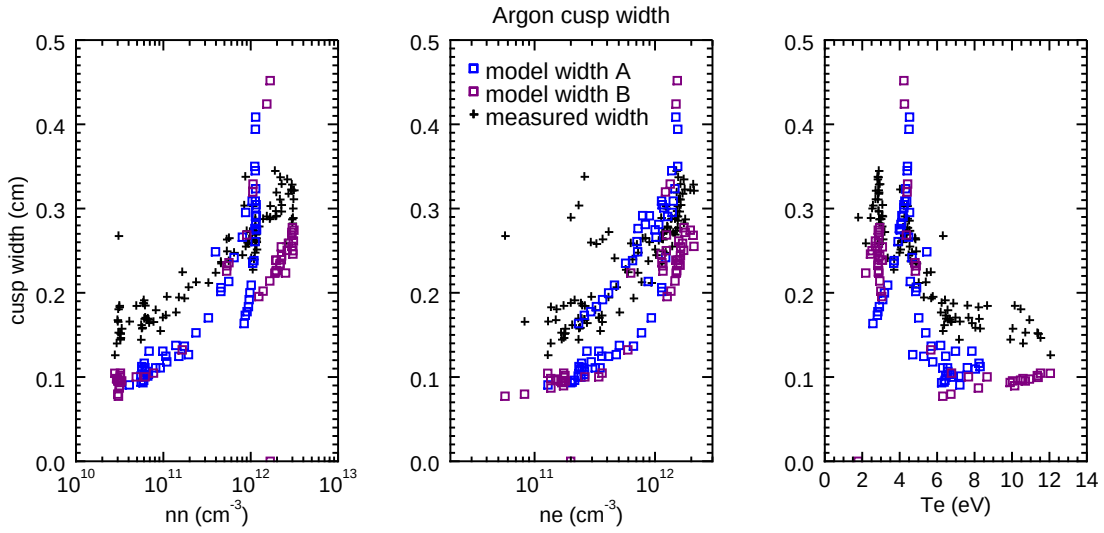

Figure 3.10: Simulated cusp loss width for argon plasmas. The embedded tile probe measurements are shown for comparison.

wall (corresponding to a large cusp width). Not only do the denser plasmas have more radial flux into the cusp, but the peak of the radial flux is closer to the density edge as well.

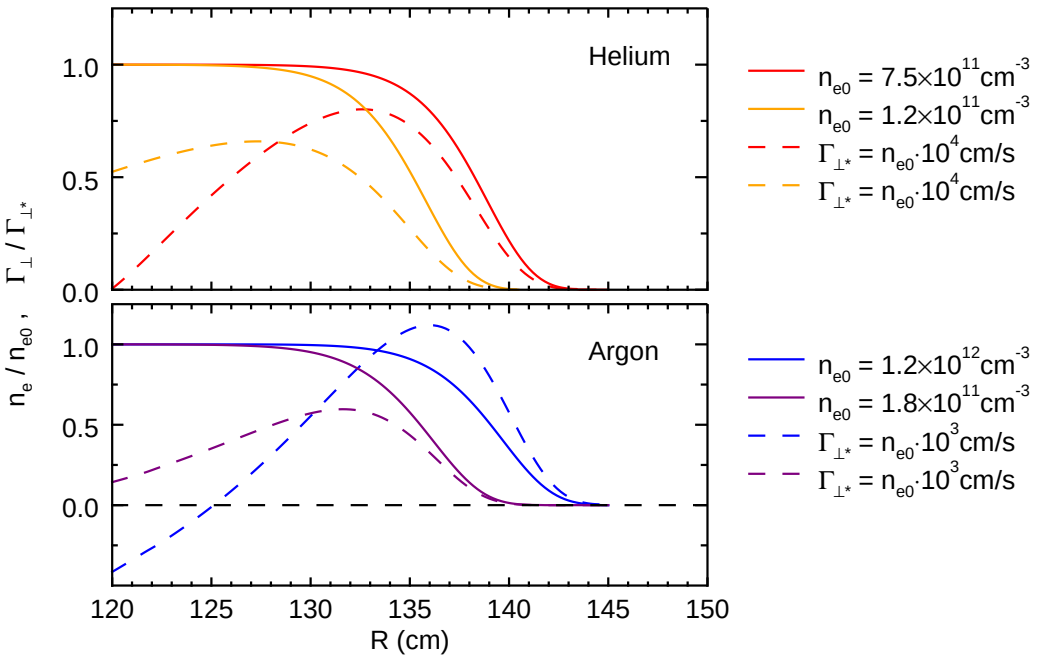

Figure 3.11: Variations in plasma edge position for helium and argon simulations. In general, higher densities in the plasma core result in larger cross-field fluxes and a plasma edge that is closer to the vessel wall.

These simulated trends match the cusp width measurements in argon plasmas only; helium measurements, as noted above, are insensitive to all three plasma parameters. This is better seen in Fig. 3.12, where the modeled cusp widths are compared to the embedded probe measurements. The argon and helium width measurements are better fit by the ambipolar transport model in comparison to the hybrid gyroradius theory. The argon measurements trend closer to the modeled cusp widths, and while the helium measurements do not follow the modeled trend, their average width is accurately predicted.

While the results of this ambipolar diffusion transport model are a better representation of the measured cusp widths in MPDX, the model should not be viewed as an accurate prediction of plasma loss area. The comparisons shown in Fig. 3.12, while an improvement over previous theory, are not satisfactory for predictive purposes. This is explained by two major physical effects

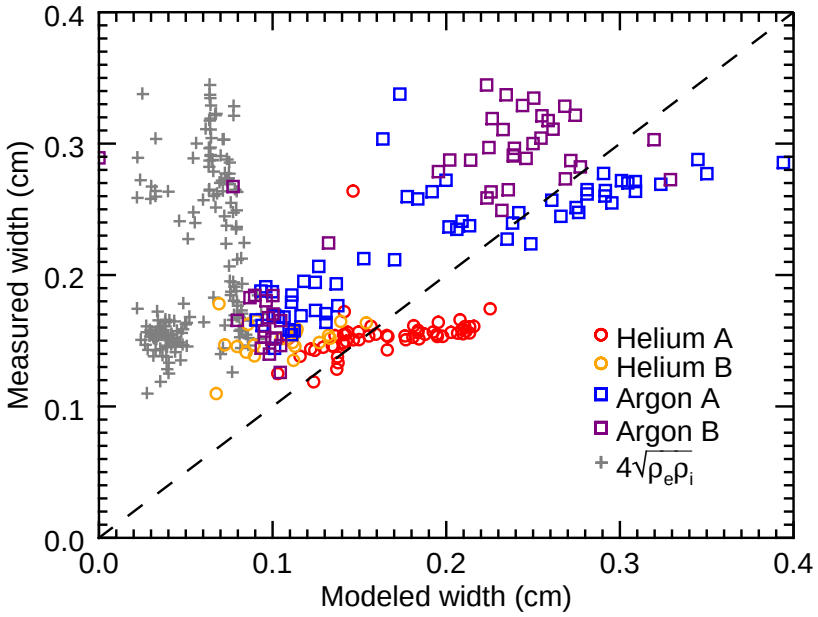

Figure 3.12: Comparison of measured cusp widths to modeled cusp widths. The gray data points show the prediction of the hybrid gyroradius theory, and it is apparent that the ambipolar diffusion model describe here is a much better fit to the data.

that are ignored: non-linear transport and diamagnetic effects. First, it has been mentioned that ion-electron elastic collisions can affect magnetized transport in the MPDX cusp field, and this model only addresses plasma-neutral collisions in its formulation of a diffusion coefficient. The relative importance of the nonlinear collision frequencies in the denominator of Eq. 3.9 can vary between helium and argon plasmas, but in general the $\nu_{ei}\nu_{in}$ nonlinear term can be larger than the linear $\nu_{in}\nu_{en}$ term at large ionization fractions. A more complete theory would include these effects, but the addition of a diffusion coefficient dependent on plasma density would significantly complicate the analytical and numerical calculations.

The second physical effect left out of this model is diamagnetic feedback on the cusp field itself. All magnetic calculations were conducted assuming a static vacuum magnetic field, with negligible plasma current. However, the solutions of the transport equations are very sensitive to the cusp field gradients, and a large enough plasma pressure might alter the field geometry in a

significant way. Preliminary work has suggested that very dense plasmas will reduce cusp field strength at radii inside of the surface where plasma thermal beta is equal is unity, while increasing field strength outside. A more complete model would account for these effects, requiring nonlinear feedback between the modeled density profile and the background field geometry. It remains to be seen whether these improvements would be valuable additions though, as the fundamental physical description of cusp transport has already been elucidated via the simpler model presented in this Chapter.

3.5 Edge ion drift modeling and measurements

One interesting consequence of ambipolar diffusion in the MPDX cusp is the modification of the edge drift flows. In general, the confluence of strong gradients in both plasma pressure and magnetic field results in plasma fluid drifts in the edge region. These drifts have been extensively measured with scanning velocity probes and can reach maximum speeds in excess of 5 km/s. In the absence of any radial electric fields in the plasma edge, these drifts are comprised solely of diamagnetic fluid drifts. However, ambipolar diffusion is regulated by an electric field that acts to slow the transport of the faster diffusing species, and this electric field will add an $\mathbf{E}\times\mathbf{B}$ component to the diamagnetic drifts at the plasma edge. If the linear transport model described above is a good description of the plasma edge, then it should be able to provide an accurate prediction of the total plasma drift.

The best edge drift measurements were taken in the helium plasma shown in Fig. 3.1. Using the measured core parameters as inputs for the transport model, the simulated density profile is obtained and compared to the probe data. Fig. 3.13 shows that the modeled edge profile is a very good match to the measurements. The corresponding velocity measurements from the probe array are shown in Fig. 3.14. A total of seven probes were used to diagnose the edge flows at seven different latitudes, and apart from the expected sign change from ring to ring, both the location and the magnitude of the drifts seem to be spherically uniform. Peak flow occurs somewhere around $r = 134$ cm, which is very close to the center of the density gradient region, and a reversal in flow

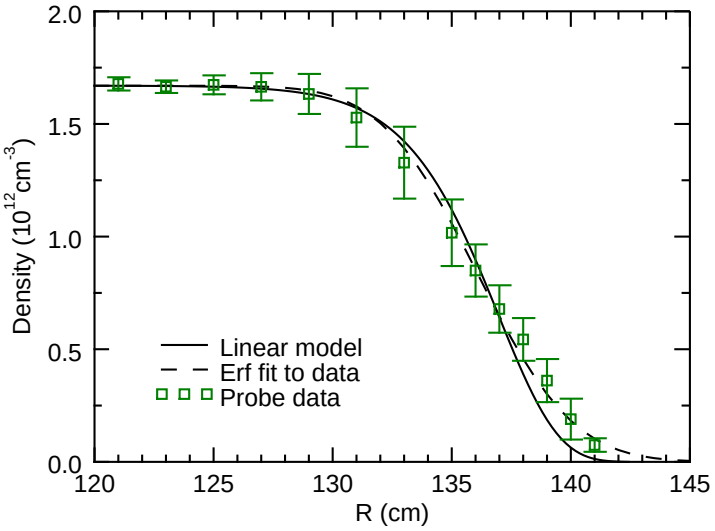

Figure 3.13: Comparison of measured edge density profile to modeled profile. The error function fit to the data is shown for reference, and is quite closely matched by the model results.

is observed at around $r = 138\,\text{cm}$. As the plasma density quickly drops to zero, the variability between latitudes increases, with some probes measuring a larger velocity reversal than others.

The right-hand plot in Fig. 3.14 shows the weighted average of all seven probe chords and compares that to the edge drifts predicted by the transport model. The two flow components that the model calculates are the diamagnetic flow and the $\mathbf{E} \times \mathbf{B}$ drift,

$$\mathbf{v}_D = -\frac{\nabla p \times \mathbf{B}}{enB^2} \tag{3.56}$$

$$\mathbf{v}_E = \frac{\mathbf{E} \times \mathbf{B}}{B^2} \tag{3.57}$$

which in the MPDX cusp geometry are always in the opposite directions for ions (which dominate the kinetic energy of the plasma flows). Using the modeled density and its gradient, and scaling the temperature gradient to approximately 1/2 of ∇n as suggested by probe measurements, we find that the predicted edge drifts are very close to the actual probe measurements. The model results accurately simulate both the radial location and the magnitude of the edge flows, and it

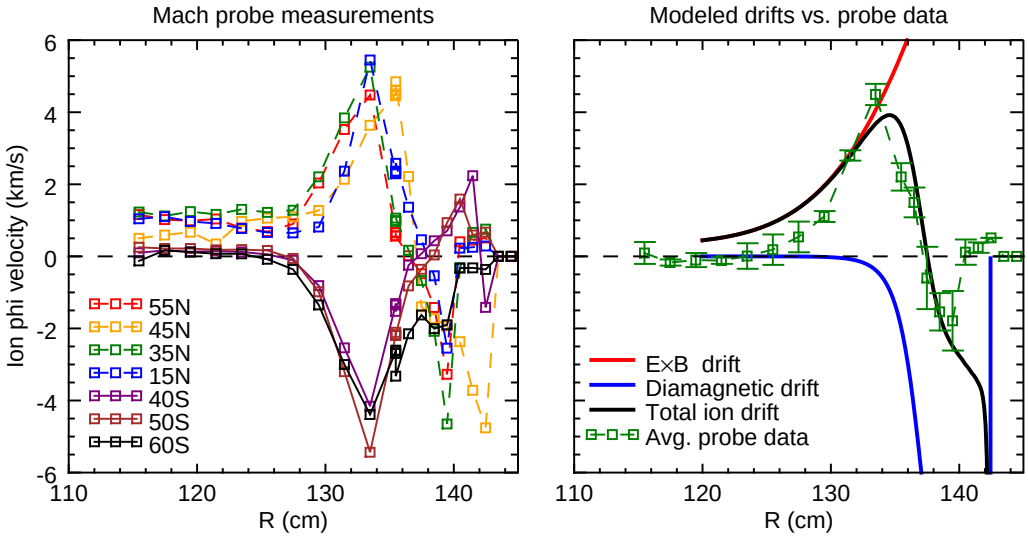

Figure 3.14: Comparison of measured edge drifts to modeled drifts. The direction of the measured flow is dependent on the direction of the local magnetic field, which switches from $+\hat{\theta}$ to $-\hat{\theta}$ every 5° latitude. The modeled components of the edge drifts are shown to be a good prediction of both the radial location and the absolute magnitude of the edge flows.

even recreates the sharp reversal in flow direction at $r = 138\,\text{cm}$. This is shown to be caused by the varying profiles of $\mathbf{v}_D$ and $\mathbf{v}_E$; the $\mathbf{E} \times \mathbf{B}$drift is the dominant momentum source closer to the core, but the diamagnetic drift becomes large enough to briefly force flow in the opposite direction before the plasma becomes too diffuse for any accurate measurements.

The predicted ambipolar electric field is small, involving a drop of only 5 V between the plasma core and the very edge of the density profile. Attempts have been made to measure these potential gradients in the plasma edge, but the typical densities of an MPDX plasma are too large for commonly used tungsten-filament emissive probes. A promising avenue for future work in this direction might involve the development of a LaB_6 emissive probe, which should be able to produce the required emission current density without burning up. The accurate measurement of this small electric field would be an excellent coda on these studies of the edge transport in a magnetic cusp device.

Chapter 4

Global plasma confinement: Particle, Charge, and Power balance

One of the most important parameters in designing a plasma experiment to investigate flow-driven MHD instabilities is the magnetic Reynolds number, *Rm*. This dimensionless ratio of magnetic advection to magnetic diffusivity needs to be large in order to excite an instability like the dynamo or the MRI, and this requires foremost a large electron temperature. It has been demonstrated that the magnetic cusp field in MPDX can confine quiescent dense plasmas, but this alone is not enough to guarantee a large *Rm*. Not only must the particle confinement time be sufficiently long, but the energy confinement time must also be long enough to permit electron temperatures in excess of 10 eV.

This chapter will detail the research on plasma heating in MPDX, with the goal of understanding the best way to heat electrons through DC arc discharges. Measurements of input power scans will be presented, and a global 0D power balance calculation will be used to determine the effectiveness of the aforementioned emissive LaB_6 cathodes in coupling power directly to the plasma. Power losses through radiation and neutral collisions (both elastic as well as charge-exchange) limit the efficiency of direct plasma heating, but the main limitation to discharge heating will be identified as the unexpected sensitivity of the plasma potential on the input power. Ultimately, the factors that limit the maximum *Rm* will be discussed, and future methods of heating (including a planned 100 kW ECH system) will be proposed to bypass current limitations.

4.1 Arc Discharge Heating

The method of arc discharge heating is one of the oldest ways to ionize and sustain a plasma. The first plasma experiments were conducted in evacuated glass tubes and used metal electrodes biased to large voltages [47, 48]. While the plasmas produced were very low density and have very small ionization fractions, these 'glow discharges' could be run CW thanks to the tiny current permitted by the cold electrodes. More modern discharge experiments use special electrodes with unusually low work functions to achieve higher discharge currents and therefore high plasma heating power. Specially coated refractory metals like thoriated tungsten permit relatively large emission at a small cost, but tend to have short lifetimes due to their fragility and failure at high temperatures. Ceramics like BaO and LaB_6 can be better choices for large, steady-state experiments thanks to their durability and particularly low work functions [30]. The cathodes used to heat MPDX are radiatively heating to a relatively cool 1300°C and yet still emit up to 120 A per cathode. This injection of energetic primary electrons is what initiates plasma ionization of a neutral fill gas, and even after plasma production becomes dominated by thermal electron ionization the primaries continue to inject power into the system via collisional thermalization and kinetic effects.

The gradual increase of the installed power on MPDX has allowed for the continual monitoring of the relationship between plasma parameters and input power. The total emissive electrode inventory currently numbers 12 individual LaB_6 cathodes, with an installed power of 360 kW. In general, the increase in installed power has resulted in higher electron densities and temperatures, as well as higher ion temperatures. A power scan was performed in both helium and argon plasmas in order to quantify these trends; the results are shown in Fig. 4.1. As the input power increases from 50 kW up to nearly 300 kW, the plasma pressure measured in the helium plasmas shows the largest increase, as *ne* and *Ti* increase by a factor of six (comparable to the power increase). Electron heating is also observed, with *Te* nearly doubling over the power scan. The argon measurements show a less pronounced change in plasma pressure, with n_e and T_i merely doubling and T_e hardly increasing at all.

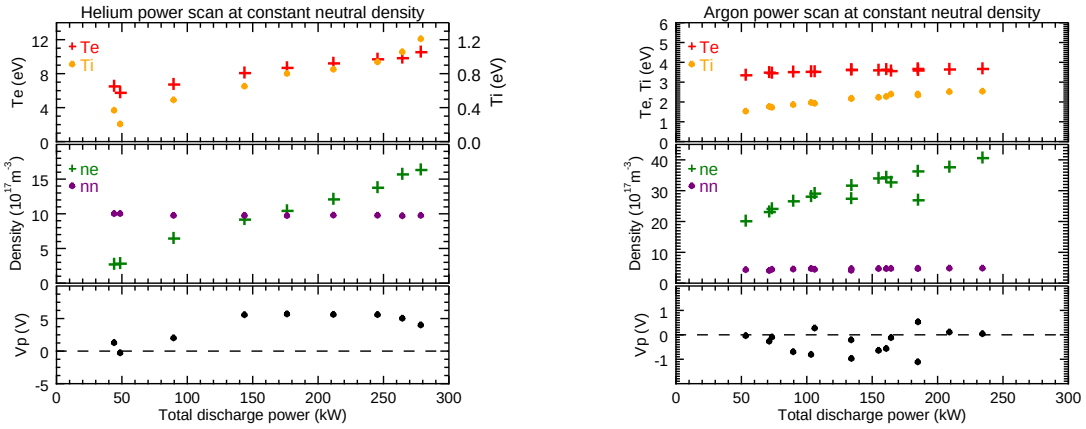

Figure 4.1: Input power scan in helium and argon. Plasma shots were binned in order to plot the plasma parameters at constant neutral pressure. The measured plasma potential is noticeably less than the expected 3-4 Te above the grounded anodes.

This difference in heating efficiency is easily explained by the well-known difference in radiation rates between the two gas species. Argon, being a higher Z element, has many more atomic transitions allowed for a given electron collision, and will radiate away a large fraction of the power that would otherwise go into heating plasma particles. This also explains the lower *Te* in argon plasmas. Conversely, argon has a lower first ionization potential compared to helium (15.8 eV vs. 24.6 eV), and so can be sustained at these low electron temperatures. The ionization fraction in argon plasmas increases dramatically at high input powers, so much so that the core of the plasma is almost certainly completely burned out. Note that the neutral pressure is measured at the wall by cold cathode vacuum gauges and that the mean free path of a room-temperature neutral argon atom a maximum of only 10 cm at these parameters; thus, the bulk of the confined argon plasma is nearly 100% ionized. Helium plasmas, while not completely burned out, still achieves ionization fractions in excess of 0.6. Such highly ionized plasmas are a first for so-called 'magnetic bucket' devices.

Perhaps the most interesting measurement made during these input power scans is the plasma potential. This, like the electron temperature, is measured by Langmuir probes inserted into the unmagnetized core and is calculated using classical Langmuir probe theory. Assuming a maxwellian electron distribution, the floating potential measured at the probe is related to the bulk plasma potential by [49, 50]

$$V_p = V_f - \lambda Te \tag{4.1}$$

$$\lambda = \ln\left(0.61\sqrt{2\pi\frac{m_e}{m_i}\left(1+\frac{Ti}{Te}\right)}\right) \tag{4.2}$$

Generally, λ is about -4.0 for helium plasmas and -5.0 for argon plasmas. This places the plasma potential somewhere between 15 V and 40 V above the floating potential the the probe. The same is true at any plasma facing surface; indeed, the plasma potential is determined by the combined effects of every sheath at every conducting surface. However, the measured plasma potential is consistently more negative than would be expected using this classical sheath description. A unique feature of the MPDX device is the insulating alumina limiters that cover the entire plasma-facing surface of each magnet ring. Unlike previous 'magnetic bucket' devices, the vessel wall is *not* electrically connected to the plasma, and so what would normally be the largest grounded plasma-facing conductor is now only a set of insulators that will float to a potential λTe volts below the plasma potential. The molybdenum anodes (and to a lesser extent, the smaller LaB_6 cathodes) are therefore the most important conducting surface area that the plasma sees, and will collectively determine the plasma potential.

This determination of V_p is important to plasma heating, because the energy of the injected primary electrons is directly proportional to the difference between the cathode bias and the plasma potential. Since the cathodes are biased to negative hundreds of volts with respect to the grounded anodes, primary electrons will be able to ionize the neutral gas species only if V_p is at least ~ 100 V above the cathode bias. We expect V_p to be very close to ground thanks to the large surface area of the anodes, and this is usually the case: the potential drop at the cathode sheath is hundreds of volts larger than the anode sheath voltage drop [51]. However, at large input powers (and more specifically, large input *currents*) a sudden and dramatic change in V_p has been observed. As shown

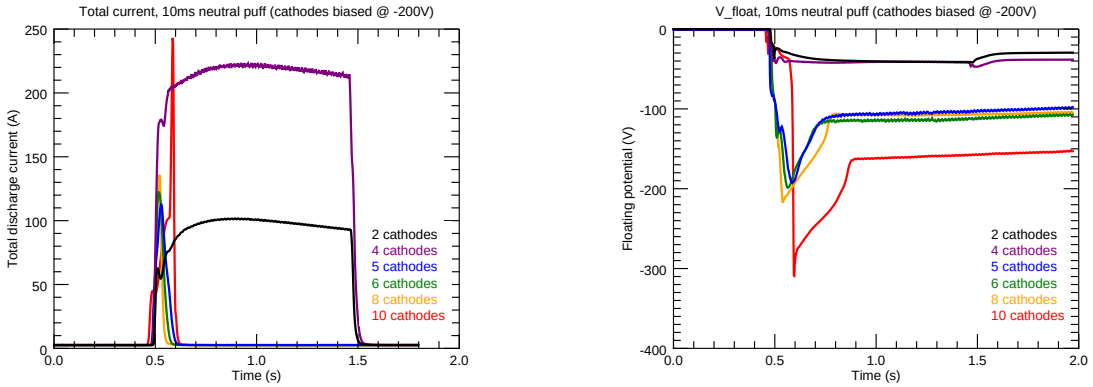

Figure 4.2: Input power scan in helium and argon. Plasma shots were binned in order to plot the plasma parameters at constant neutral pressure. The measured plasma potential is noticeably less than the expected 3-4 Te above the grounded anodes.

in Fig. 4.2, it is possible for the plasma to self-extinguish after only 100 ms. This phenomenon follows a predictable pattern. Immediately after the large negative bias is applied to the cathodes, the plasma density and temperature rise to expected levels. But when the input current is large enough (or, as will be discussed below, the anode area is small enough) within 100 ms there occurs a very sharp drop in the plasma potential. Once V_p falls to within ~ 50 V of the cathode bias, the primary electrons no longer are energetic enough to sustain plasma losses with ionization, and the plasma extinguishes. The DC bias power supplies, measuring this immediate change in electrical load, turn themselves off (as part of their arc prevention safeguards) and the plasma shot is ruined.

In order to better diagnosis this self-extinguishing event, an experiment was conducted wherein the total anode surface area was slowly decreased over the course of many helium plasma shots. Beginning with a total of twenty molybdenum anodes, one anode at a time was retracted from the plasma and the effect on V_p was measured. The experiment continued until the self-extinguishing phenomenon began to occur, at which point Langmuir probe measurements of the plasma parameters became impossible. The neutral fill pressure was varied at each anode area level to diagnose the effect of neutral collisional and radiative power loss channels. The results of this experiment

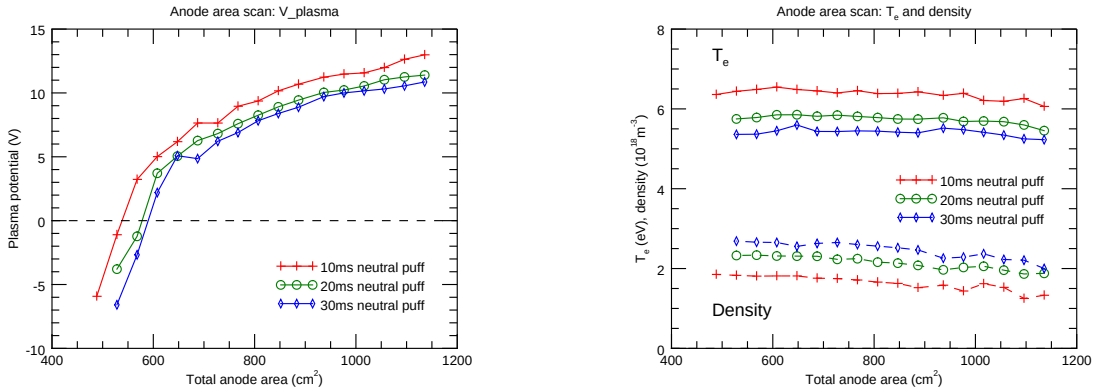

Figure 4.3: As anode area was slowly decreased, while input power was held constant, the measured plasma potential also decreased. The left-most points on the potential plot were the last measurements made for each neutral fill level before the plasma began to self-extinguish.

are shown in Fig. 4.3. The input discharge power was maintained at a constant level for each neutral fill pressure during the entire area scan, and so the bulk density and temperature are relatively constant. At maximum anode area, V_p was at least 10 V above ground, but as anodes were removed V_p decreased. V_p dropped below the grounded anode potential after the removal of 14 or 15 anodes, depending on neutral fill pressure, as the smallest fill level consistently resulted in a higher V_p relative to higher fill pressures. The sudden onset of the self-extinguishing events began just after the rate of change in V_p began to increase, and further Langmuir probe measurements were rendered impossible due to the extremely negative plasma potentials (which could easily burn out probe circuitry).

Having observed that V_p is affected both by a change in anode area as well as a change in input current, it stands to reason that anode current density the important factor in determining the plasma potential. The additional impact of neutral pressure implies that the problem is global in nature. For example, the amount of discharge current drawn at a certain cathode bias depends on many interconnected parameters; high plasma density and high electron temperature permit a larger conductivity, but require a similarly large neutral pressure in order to ionization to balance

the increases convective losses to the wall. The temperature of the cathode limits the emissivity and therefore the emitted primary current, but the core parameters determine whether the emission is space-charge limited or not. The rest of this chapter will explore how V_p is determined by these factors, and will use a detailed analysis of the various pathways for global particle, power, and current conservation in order to build a 0D numerical description of how the core plasma parameters are set. Much of this work is based on the particle and power balance work of Cho, Hershokowitz, and Intrator [52], which was also formulated in the context of a hot-filament discharge plasma in a multidipole device.

4.2 Particle Balance

In order to balance the particle sources and sinks in an MPDX plasma, it is necessary to take into account all the possible ways each species can enter and leave the system. We will consider four different plasma species: Maxwellian electrons, singly and doubly charged ions, and monoenergetic primary electrons. All species are lost into classical Bohm sheaths at plasma-facing insulators, both in the plasma bulk (like alumina or quartz shields on electrode shafts) and in the plasma cusp (at the alumina limiter tiles that cover the magnet rings). Particles are also lost at the conducting electrode surfaces, whose sheaths may or may not be Bohm-like. The cathode sheath is purely ion-collecting and repels both thermal and primary electrons. The anode sheath is more complicated and particle loss to the grounded anodes depends on the plasma potential. If $V_p > 0$ as is the usual case, then the anode sheath is ion-collecting and somewhat electron-repelling, but there have been many cases where an MPDX plasma has been measured to have $V_p < 0$. In these cases, the anode current density was always a small fraction (≤ 0.1) of the electron saturation current density, and so the anode sheath must include a double-layer potential structure [53, 54]. A simplified cartoon of these two scenarios is shown in Fig. 4.4. Particle balance equations must take into account variability both in V_p as well as in the ion-collecting part of the anode sheath, ΔV_A.

The ionization source terms will include ionization from both thermal and primary electrons, and are responsible for the production of thermal electrons and ions. These rates are obtained from ADAS tabulated rates and are summarized in Fig. 4.5.

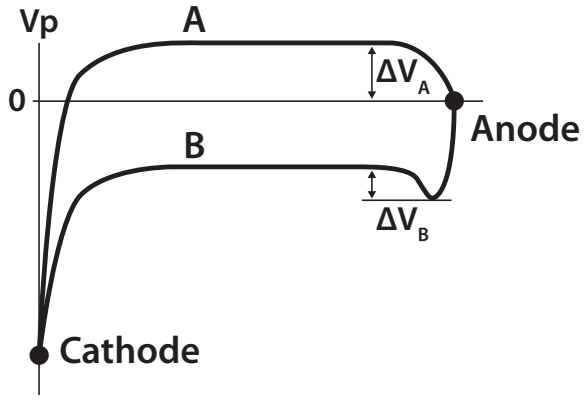

Figure 4.4: Plasma potential structure for two different anode sheath scenarios. A) $V_p > 0$ and the anode sheath is a classical Bohm sheath. B) $V_p < 0$ and a double-layer exists at the anodes. Ions are trapped in the potential well and must have some pumping mechanism to a near-by insulating surface, while electrons are still confined by ΔV_B.

The particle balance equations are as follows. We will treat primary electrons and thermal electrons as a single species for the purposes of particle confinement, as the mechanisms in MPDX for the transition from fast to slow electrons are not well understood as of yet. For primary electrons, which are injected through cathode emission current I_p, the main loss channels are to the wall through the cusp and to the non-cathode electrode surfaces. Thermal electrons are produced via primary and secondary ionization, and are lost to the cusp and to non-cathode electrodes. We differential between electrode (and probe) insulator surfaces, the cathode conducting surfaces, and the anode conducting surfaces, as particle flux to the conducting surfaces is strongly dependent on the surface's electrical bias.

$$I_p/e + n_e \mathbb{V} \nu_{iz}^e + n_p \mathbb{V} \nu_{iz}^p = n_p \mathbb{V} \nu_w + n_e \mathbb{V} (\nu_{ins} + \nu_a) \tag{4.3}$$

where $\mathbb{V}$ is the total plasma volume, n_p and n_e are the primary and thermal electron densities, and the loss rates are defined as

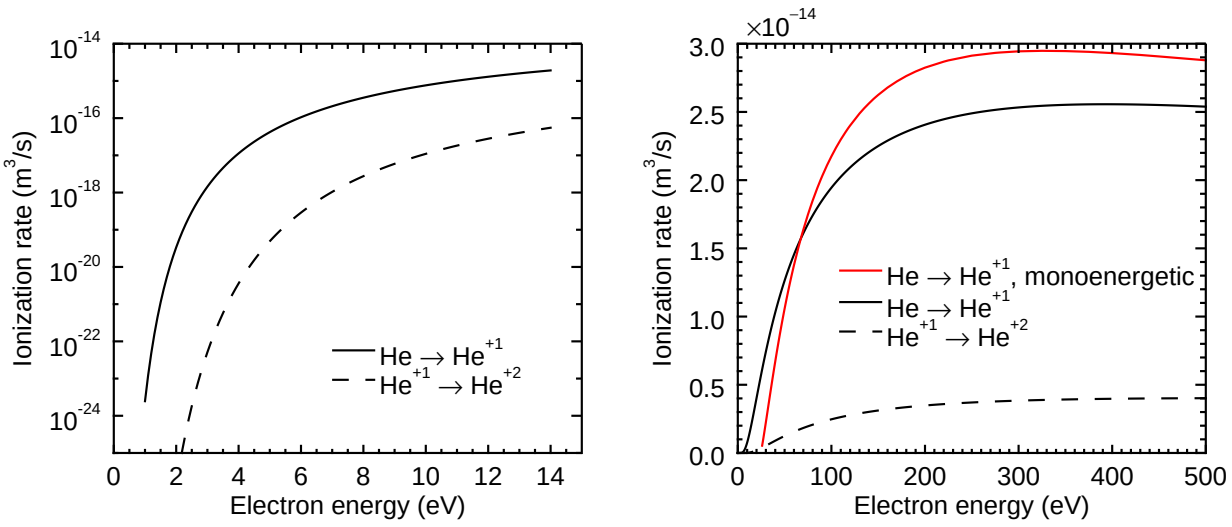

Figure 4.5: Ionization rates for thermal and monoenergetic electrons. Taken from ADAS rate tables and the NIST atomic spectral database [55].

$$\text{Ionization by thermal electrons}: \quad \nu_{iz}^{e} = n_n \langle \sigma_{iz1}^{e} v_e \rangle + n_i \langle \sigma_{iz2}^{e} v_e \rangle$$

$$\text{Ionization by primary electrons}: \quad \nu_{iz}^{p} = n_n \langle \sigma_{iz1}^{p} v_p \rangle + n_i \langle \sigma_{iz2}^{p} v_p \rangle$$

$$\text{Primary loss to all surfaces}: \quad \nu_w = \frac{1}{4} v_p \frac{A_a + A_{cp} + A_{ins}}{\mathbb{V}}$$

$$\text{Thermal loss to insulators}: \quad \nu_{ins}^{e} = 0.6 c_s \frac{A_c + A_{ins}}{\mathbb{V}}$$

$$\text{Thermal loss to anodes}: \quad \nu_a^e = \frac{1}{4}\sqrt{\frac{8}{\pi}} v_e \frac{A_a}{\mathbb{V}} X_e$$

$$where \;\; X_e = \exp(-e\Delta V_a / k_B T_e) \qquad\qquad V_p > 0$$

All insulating loss areas are lumped together into A_{ins}, which for the primary electrons includes a modified cusp loss width that is simply equal to the primary gyroradius at the magnet face. The anode loss area is A_a, and thermal electrode flux to the anodes is determined by the potential drop ΔV_a as defined in Fig. 4.4.

The ion particle balance equation takes the same form for both singly (n_i) and doubly (n_j) ionized particles.

$$n_e \mathbb{V} \nu_{iz}^e + n_p \mathbb{V} \nu_{iz}^p = (n_i + n_j)\mathbb{V}(\nu_{ins}^i + \nu_c^i + \nu_a^i) \tag{4.4}$$

with the loss rates defined as

$$\begin{aligned}
\text{Loss to insulators}: \ \nu_{ins}^i &= 0.6 c_s \frac{A_c + A_p}{\mathbb{V}} \\
\text{Loss to cathodes}: \ \nu_c^i &= 0.6 c_s \frac{A_c}{\mathbb{V}} \\
\text{Loss to anodes}: \ \nu_a^i &= 0.6 c_s \frac{A_a}{\mathbb{V}} X_i \\
where \ X_i &= \begin{cases} 1 & V_p > 0 \\ \exp(\Delta V_a / T_i) & V_p \leq 0 \end{cases}
\end{aligned}$$

The cathode loss area A_c is an ion-collection surface, while the ion flux to the grounded anodes is again a function of ΔV_a. However, if the plasma potential is lower than the anode potential (i.e. $V = 0$), ions cannot be lost to the anodes and are instead temporarily trapped in the double-layer potential well.

4.3 Current Balance

Because the plasma losses to the MPDX wall are electrically insulated from the vessel itself, it is relatively easy to determine the current balance between particle fluxes are the biased and grounded electrodes. In terms of the loss rates defined above, the current balance equation is

$$I_p + 0.6 e n_i c_s A_c = \frac{1}{4} e n_p v_p A_a + \frac{1}{4} e n_e \sqrt{\frac{8}{\pi}} v_e A_a X_e - 0.6 e n_i c_s A_a X_i \tag{4.5}$$

The primary electron current from the LaB_6 cathodes, I_p, is a function of the cathode emissivity and the local plasma parameters. There are two possibilities: if the LaB_6 is hot enough so that the number of emitted electrons is space-charge limited, then the primary current is a function of the cathode sheath size. If the LaB_6 is too cold, the thermionic emission is only a function of the cathode temperature and is independent of the sheath size.

In the space-charge limited case, the primary current is given as

$$J_0 = \frac{4}{9}\frac{\epsilon_0 \left(\frac{2e}{m_e}\right)^{1/2} V^{3/2}}{s^2}$$
$$\frac{s}{\lambda_D} = \frac{0.79}{\sqrt{\alpha_i}}\left(\frac{eV_0}{T_e}\right)^{3/4}$$

where s is the sheath thickness and α_i is the proportional drop in ion density through the presheath (ideally, $\alpha_i \sim 0.61$) [56]. Since the ion density is much larger than the primary electron density, s is set by the normal ion sheath physics. The potential drop at the anode must always be electron-confining, even if there is a double-sheath structure. The drop ΔV_a is a function of the current balance:

$$\Delta V_{anode} = -T_e \ln\left(\frac{I_p/e + 0.6 n_i c_s (A_c + A_a X_i) - 1/4 n_p v_p A_a}{1/4 n_e \sqrt{8/\pi} v_e A_a}\right) > 0 \tag{4.6}$$

As $\Delta V_a \to 0$, the amount of current drawn at the anodes approaches the electron saturation limit. However, the measured anode current density during the anode area scan does not come close the electron saturation current density, as shown in Fig. 4.6. Since anode current densities measured in MPDX plasmas rarely exceed 1/10 of the electron saturation current, we can assume that the anode sheath always has some ion-collecting, electron-rejecting structure; that is, $\nabla^2 \phi < 0$ over at least some of the sheath thickness.

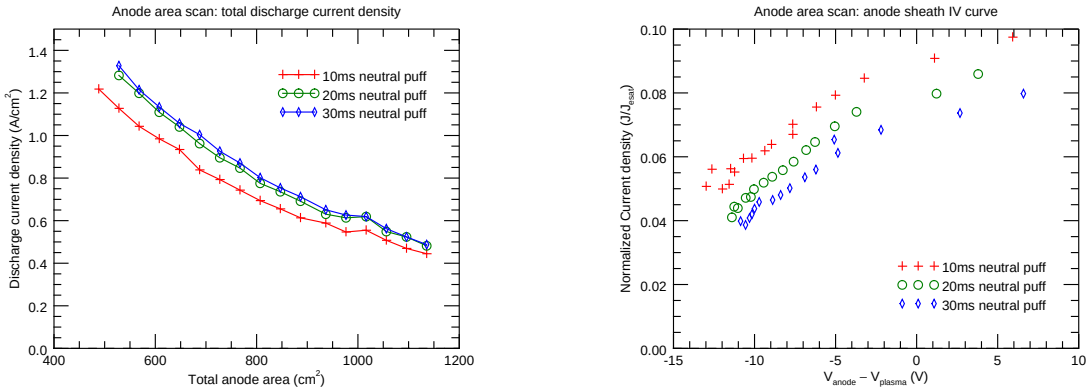

Figure 4.6: Anode current density increases as the anodes are removed. Normalized to the theoretical electron saturation current density, the anode current never exceeds 10% of the maximum possible electron current, even when the anode potential is greater than the plasma potential.

4.4 Power Balance

The power calculations in MPDX can be separated into the ion and electron power balances. For the ion power balance, the only source of power is electron-ion heating, but power is lost both through convection as well as elastic and charge-exchange neutral collisions,

$$Q_{ei} = Q_{in} + Q_{cx} + Q_w \tag{4.7}$$

where the power transfer rates are defined as [24]

$$\begin{aligned}
\text{Heating from electrons}: \quad & Q_{ei} = 3\frac{m_e}{m_i}(\nu_{ei} + \nu_{ej})n_e k(T_e - T_i)\mathbb{V} \\
\text{Loss to elastic neutral collisions}: \quad & Q_{in} = \frac{3}{2}\nu_{in}(n_i + n_j)k(T_i - T_n)\mathbb{V} \\
\text{Loss to charge-exchange collisions}: \quad & Q_{cx} = \nu_{cx} n_i k(T_i - T_n)\mathbb{V} \\
\text{Convective loss to wall}: \quad & Q_w = 1.6(\nu_a^i + \nu_c^i + \nu_{ins}^i)(n_i + n_j/2)k(T_i - T_n)\mathbb{V}
\end{aligned}$$

The rates ν_{ei} and ν_{in} represent electron-ion and ion-neutral collisions, respectively. Neutrals are assumed to be at the wall temperature, so $T_n = 0.025\,\text{eV}$.

The electron power equation balances the input discharge power with a number of loss channels,

$$Q_{disch} = Q_{eiz} + Q_{piz} + Q_{en} + Q_{en,rad} + Q_{ei} + Q_{ei,rad} + Q_w \tag{4.8}$$

where

$$\begin{aligned}
\text{Power to ionization by electrons}: \quad & Q_{eiz} = n_e n_n \langle \sigma^e_{iz1} v_e \rangle k E_{iz1} + n_e n_i \langle \sigma^e_{iz2} v_e \rangle k E_{iz2} \\
\text{Power to ionization by primaries}: \quad & Q_{piz} = n_p n_n \langle \sigma^p_{iz1} v_p \rangle k E_{iz1} + n_p n_i \langle \sigma^p_{iz2} v_p \rangle k E_{iz2} \\
\text{Loss to elastic neutral collisions}: \quad & Q_{en} = 3\frac{m_e}{m_i}(\nu_{en} n_e k(T_e - T_n) + \nu_{pn} n_p k(T_p - T_n))\mathbb{V} \\
\text{Loss to neutral radiation}: \quad & Q_{en,rad} = M_e Q_{eiz} + M_p Q_{piz} \\
\text{Ion heating}: \quad & Q_{ei} = 3\frac{m_e}{m_i}(\nu_{ei} + \nu_{ej}) n_e k(T_e - T_i)\mathbb{V} \\
\text{Loss to ion radiation}: \quad & Q_{ei,rad} = n_i(n_e P_{e1} + n_p P_{p1})\mathbb{V} + n_j(n_e P_{e2} + n_p P_{p2})\mathbb{V} \\
\text{Convective loss to wall}: \quad & Q_w = n_e \nu^e_a k T_e + \gamma_t(n_i \nu^i_l + 2 n_j \nu^j_l) k T_e + n_p \nu^p_l k \Delta V_c
\end{aligned}$$

The power loss to ionization is dependent the first and second ionization potentials E_{iz1} and E_{iz2} as well as the respective ionization cross-sections. A large fraction of the total power loss comes from radiation of neutrals and ions. The neutral radiation is calculated using the radiation multiplier coefficients M_e and M_p found in the ADAS tabulated rates, which accounts for the radiative loss associates with each ionization event. The ion radiation is similarly calculated using the tabulated collisional radiation rates P for thermal and primary electrons and both ion charge states [57]. The convective loss at the insulators is enhanced by ion heating within the sheath, and is calculated as a function of the total ion loss rates ν_l and multiplicative coefficient γ_t, which is defined as [58]

$$\gamma_t = \frac{2}{1-\delta_e} + \frac{2T_i}{ZT_e} - 0.6 \ln\left[\frac{2\pi m_e}{m_i}\left(Z + \frac{T_i}{T_e}\right)\frac{1}{(1-\delta_e)^2}\right] \tag{4.9}$$

This depends in part on the secondary electron emission coefficient δ_e and is only weakly dependent on the ion species. For $T_e < 20\,\text{eV}$, $\delta_e = 0$ and $\gamma_t \sim 5 - 8$.

4.5 Numerical balance calculations

These balance equations can be numerically solved with a globally convergent non-linear root-finding routine, like the Newton or Broyden methods [46]. The above equations can be reduced to a system of four equations: electron particle balance, current balance, electron power balance, and ion power balance. Three of the four unknowns to be solved for are chosen to be T_i, n_p, and ΔV_a, which in the case of the latter two are unable to be measured in MPDX. The final unknown variable must be related to the input power; options include either the plasma potential V_p or the cathode discharge current I_{disch}. It turns out that the balance equations are relatively insensitive to changes in V_p, mainly because the cathode bias is so much larger than variations of $10\,\text{V}$ about the $V = 0$ grounded anode potential. Therefore, I_{disch} is chosen as the forth unknown variable, and so can be compared to the measured discharge current in order to determine how accurate this balance model is.

Fig. 4.7 shows the model results using the measurement from the anode scan experiment. Measured data is shown as symbols, while model outputs are shown as solid lines, and the three different levels of neutral fill pressure are colored red, green, and blue. The residual errors in power balance and current balance are shown to be much smaller than unity. The x-axis on all plots is the inserted anode area in cm^2.

Generally speaking, the numerical solutions to the balance equations agree with measurements of neutral density and ion temperature. Note that the neutral density is measured by vacuum gauges at the vessel wall, and the volume averaged neutral density throughout the plasma is smaller due to ionization. It follows that the lower density shows have a smaller amount of neutral burn-out. Similarly, the modeled T_i follows the same trend and ordering as the measured T_i. Measurement errors for this experiment were larger than expected ($\sim 0.5\,\text{eV}$) and so the power balance solutions of T_i fall within the Fabry-Perot error. Regardless, the Fabry-Perot data shows clear signs of ion heating in MPDX, a significant achievement in the field of 'magnetic bucket' devices. Ion heating

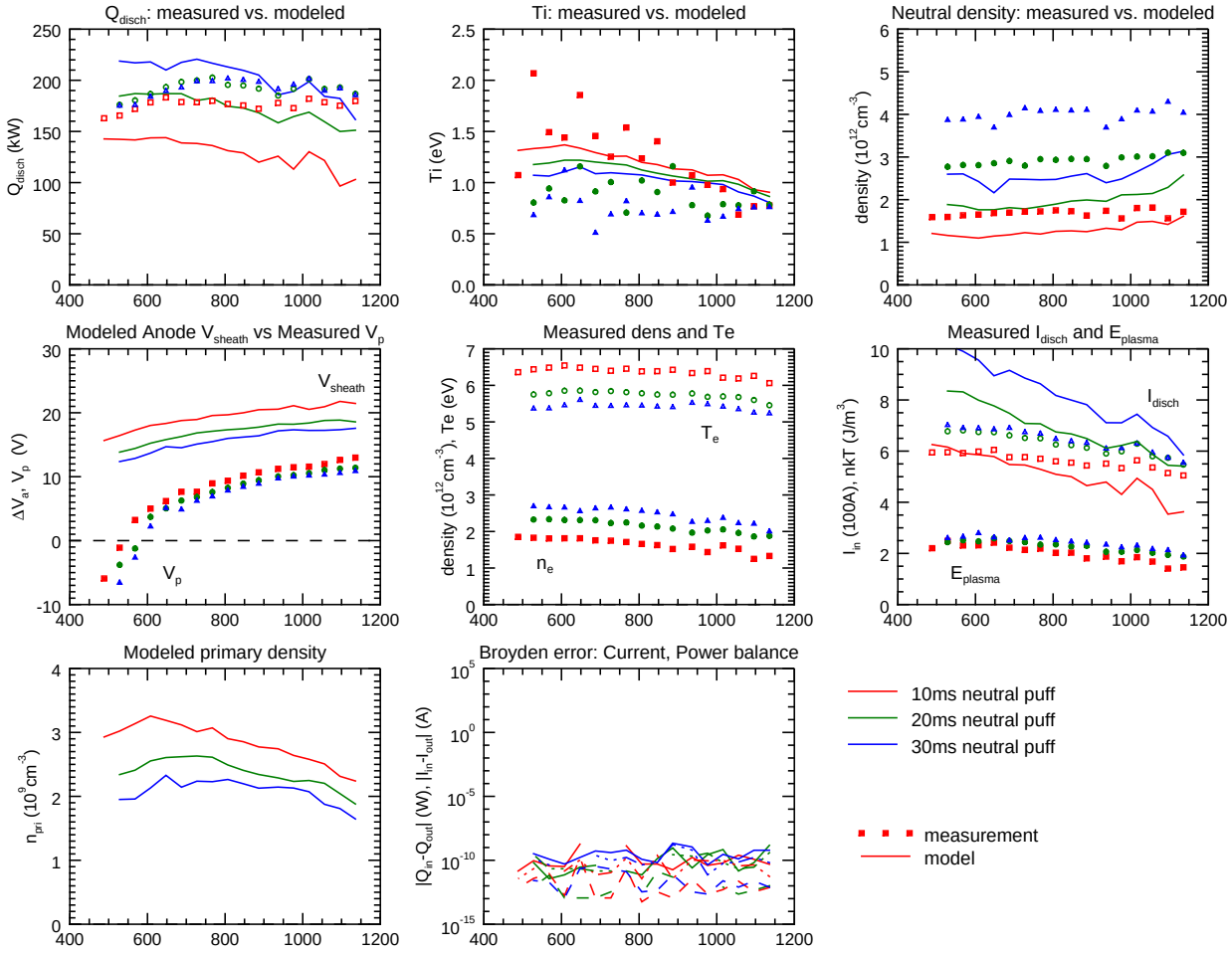

Figure 4.7: Summary of solutions to the balance equations for the three neutral fill levels in the anode area experiment. The x-axis on all plots is the inserted anode area in cm^2.

is most efficient at low neutral densities due to the reduced power loss through charge-exchange collisions.

The model solutions for n_p and ΔV_a are harder to compare to experimental data, since neither of these quantities are directly measured. However, all solutions for the primary electron density are very small compared to n_e and n_i, making up about 0.1% of the total charge density. Since the anode sheath potential is largest at small neutral fill levels, it makes physical sense that the increased electron confinement would lead to slightly higher n_p. The overall trend of slightly higher plasma pressures at smaller anode area means that the modeled T_i and n_p are also larger at

smaller anode area. Furthermore, the modeled anode sheath potential ΔV_a is relatively constant as a function of anode area. This is due to the exponential relation between ΔV_a and electron confinement at the anodes: a small change in the sheath potential is enough to effect a large charge in electron confinement.

The main result of this model is the comparison of measure discharge current and power to measured discharge current and power. Fig. 4.7 shows that the modeled input power $Q_{disch} = I_{disch}(V_p - \Delta V_c)$ is more spread out as a function of neutral fill pressure. For example, the model solutions for the 10 ms neutral puff show that the measured plasma pressure shouldn't need as much input power as is experimentally measured. The same is true for the other two neutral fill levels when the inserted anode area is large. This may hint at an unexpected channel for primary electron power loss, which would result in a lower percentage of input power finding its way into electron and ion heating.

Fig. 4.8 shows the individual terms in the four balance equations, and Table 4.1 give the definition of each term. Several important features are apparent. First, the ion particle losses to the anodes (Ni_a) are exactly zero, while the electron particle losses to the anodes (Ne_a) are identically equal to the injected primary particle rate (Ip/e). This is a consequence of current balance in the case where the anode sheaths are small enough to completely confine ions. The anode sheaths are obviously not classical Bohm sheaths, and this is further evidence for the existence of a double-layer at the anode-plasma interface.

Second, the main channels for power loss are not convective. Indeed, the total electron convective losses (Q_{ew}) are on the order of 10 kW whereas the power losses through neutral radiation ($\mathrm{Q}_{en,rad}$) and through ion-neutral elastic collisions (Q_{in}) dominate the electron and ion power balance. Also important is the electron-ion heating term (Q_{ei}), which is the second largest power sink the electron balance. This indicates that the ring cusp confinement geometry is excellent at increasing the energy confinement time, mainly due to the very small ratio of cusp loss area to plasma volume.

While this model adds to the understanding of particle and power balance in MPDX plasmas, it still does not explain the high degree of V_p sensitivity to anode current density. Looking at the

Ne_{iz}	Primary ionization by thermal electrons
Ne_{iz2}	Secondary ionization by thermal electrons
Np_{iz}	Primary ionization by primary electrons
Np_{iz2}	Secondary ionization by primary electrons
Ni_{c}	Ion loss to cathodes
Ni_{a}	Ion loss to anodes
Ni_{ins}	Ion loss to insulators (includes cusp)
Ip/e	Primary electron source from LaB_6 emission
Ne_{a}	Electron loss to anodes
Ne_{ins}	Electron loss to insulators (includes cusp)
Q_{ei}	Ion heating by thermal electrons
Q_{in}	Ion power loss to elastic neutral collisions
Q_{cx}	Ion power loss to charge-exchange collisions
Q_{iw}	Ion convective power loss
Q_{disch}	Input discharge heating power
$Q_{en,rad}$	Electron power loss to neutral radiation
Q_{en}	Electron power loss to elastic neutral collisions
Q_{eiz}	Electron power loss to primary ionization
Q_{eiz2}	Electron power loss to secondary ionization
$Q_{ei,rad}$	Electron power loss to ion radiation
Q_{ew}	Electron convective power loss

Table 4.1: Definition of terms in Fig. 4.8

relatively flat ΔV_a curves, it is clear that power balance does not play a large role in setting the potential drop at the anode sheath. It is likely that more complicated plasma-material interaction physics is at play here. The hypothesized anode double-layer could be caused by secondary electron emission at the molybdenum surface, and the density and energy of primary electrons would significantly alter the rate of secondary emission [59, 60, 61]. Recent numerical studies have

shown that secondary emission can alter the plasma potential on a global scale [62]. The specifics of ion pumping out of the double-layer potential well is also a possible complication in the sheath physics [53]: this would involve detailed analysis of the shape and structure of the anode sheath and presheath. It is quite likely that future work on this problem will require kinetic modeling, especially since the neutral elastic collision length can be hundreds of cm long, orders of magnitude longer than the electron and ion collision lengths.

Until this issue of dramatic drops in V_p and self-extinguishing plasmas is better understood, it is recommended that additional methods of plasma heating be explored. Current work on a high-power electron cyclotron heating system is close to completion, and up to 100 kW of ECH should be installed on MPDX in the near future. This will dramatically change the power balance in MPDX by allowing much more power to be directed to electron heating without any of the complicated sheath effects discussed in this Chapter. If plasma heating is decoupled from the discharge current, then the emissive LaB_6 cathodes can be used more selectively for plasma flow drive, as they were originally intended to be. It is hoped that lowering discharge current will only improve plasma conditions, by lowering thermal loading on electrodes and improving shot-to-shot repeatability.

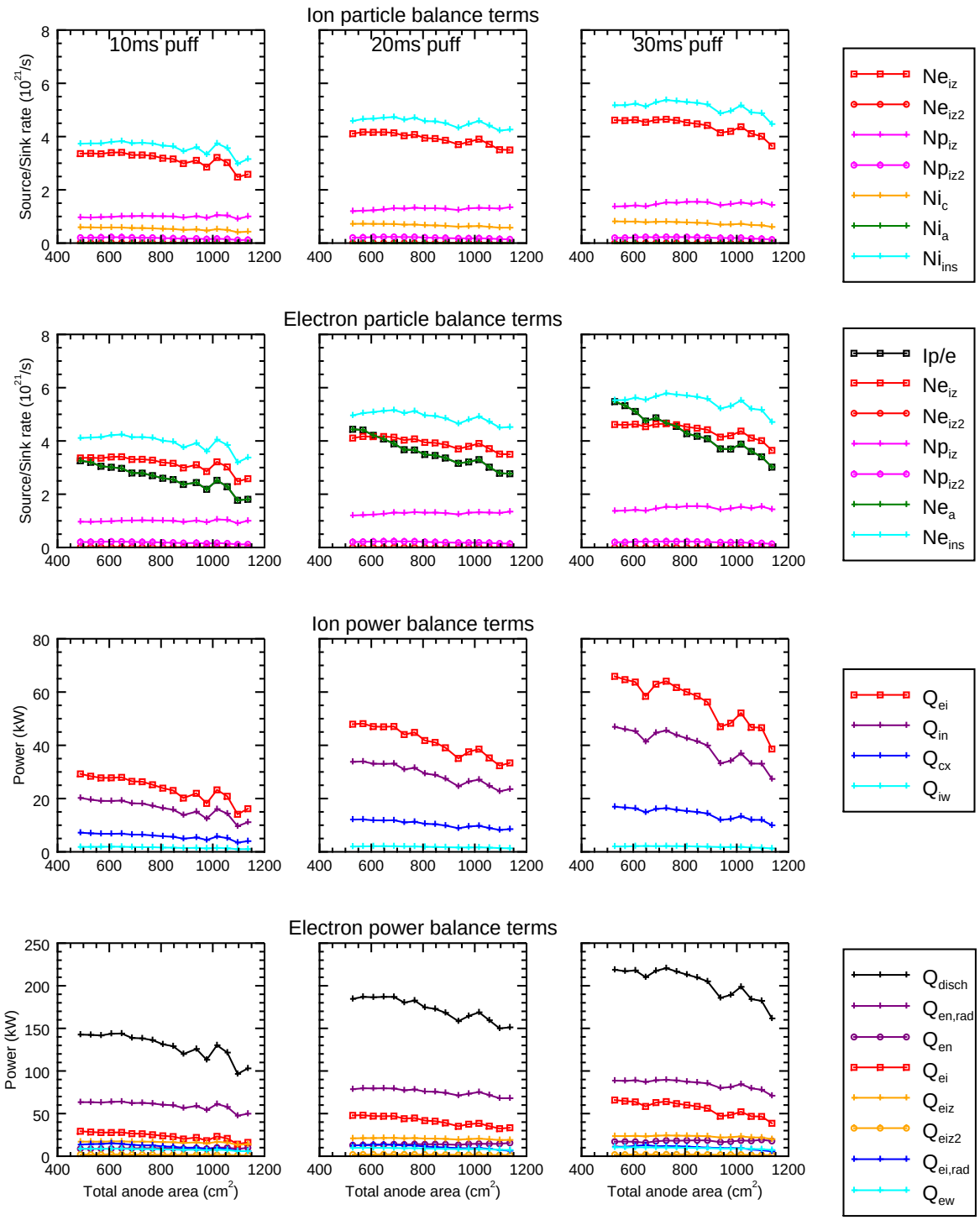

Figure 4.8: Summary of particle and power balance terms for the three neutral fill levels in the anode area experiment. The x-axis on all plots is the inserted anode area in cm^2, and the three vertical columns represent the three neutral fill levels.

Chapter 5

Two techniques for stirring high Alfven Mach number plasmas

Having explored the confinement and heating characteristics of MPDX plasmas, the last ingredient necessary for a high *Re* plasma is ion flow. This Chapter presents the hydrodynamic theory and measurements of generating flowing plasmas in MPDX. First, a series of numerical simulations are described which suggest that a spherical unmagnetized plasma experiment is capable of generating a laminar, 'slow' dynamo. The results of two different types of flow experiments are presented, and the velocity measurements are shown to match hydrodynamic models. In addition to these dynamo-capable flows, a set of couette-like flow experiments are detailed that show promise for the investigation of the MRI. The qualified success of these flows is discussed, as is the future work necessary for the realization of both types of flow-driven MHD instabilities.

5.1 Numerical modeling of plasma hydrodynamics

The design and construction of MPDX is based on the results of previous work addressing the feasibility of a laboratory plasma dynamo. A kinematic dynamo code was written to determine whether positive magnetic growth rates were achievable given the expected MPDX parameter regime. As described in Chapter 1, the dimensionless numbers *Re* and *Rm* were used to describe the global properties of the flowing conducting fluid. Two additional dimensionless parameters are useful in parameterizing the global flow characteristics: the Alfvenic Mach number *Ma* and the dimensionless neutral drag χ,

$$Re = VR/\eta = 7.8\frac{n_{18}\sqrt{\mu}Z^4 V_{km/s} R_m}{T_{i,eV}^{5/2}},$$

$$Rm = \mu_0 \sigma V R = 1.6\frac{T_{e,eV}^{3/2} V_{km/s} R_m}{Z},$$

$$Ma = V/V_A = 0.46\frac{\sqrt{n_{18}\mu} V_{km/s}}{B_G},$$

$$\chi = \frac{R^2}{\nu \tau_{in}} = 31.8\frac{n_{18} n_{n,18} Z^3 R_m^2}{T_{i,eV}^2},$$

where V and R are the characteristic velocity and length scales of the experiment, ν is the kinematic viscosity, and σ is the resistivity. These definitions are defined above in terms of plasma parameters using Braginskii's derivations of plasma transport parameters [24], where n_{18} and $n_{n,18}$ are the plasma and neutral densities in units of 10^{18} m^{-3}, T_e and T_i are in electron volts, μ is the ion species atomic weight in amu, and B_G is the small field (in Gauss) of the plasma bulk due to the uncorrected horizontal component of the Earth's magnetic field. The role these parameters play in the dynamo effect is apparent given the dimensionless forms of the Navier-Stokes equation and the induction equation,

$$\frac{\partial \mathbf{v}}{\partial t} = \nabla^2 \mathbf{v} - Re[(\mathbf{v} \cdot \nabla)\mathbf{v} + \nabla p] - \chi \mathbf{v}, \tag{5.1}$$

$$\frac{\partial \mathbf{B}}{\partial t} = \nabla^2 \mathbf{B} + Rm \nabla \times (\mathbf{v} \times \mathbf{B}). \tag{5.2}$$

An experiment capable of exciting flow-driven MHD instabilities should have significantly more magnetic advection compared to magnetic diffusivity. This corresponds to a large magnetic Reynolds number, since *Rm* is defined as the ratio of these two terms in the induction equation. *Rm* in turn is directly proportional to the magnitude of the velocity gradients present in the plasma flow, the establishment of which are determined by solutions to the Navier-Stokes equation. Again, a

larger value of *Re* is desirable here since, by definition, such a system would have less momentum diffusivity (i.e. viscosity) and therefore steeper spacial gradients in flow. A third dimensionless parameter χ has been added to the Navier-Stokes equation, describing the loss of ion momentum via charge-exchange collisions with stationary neutrals. As cusp-confined plasmas are typically not 100% ionized, this term can have a large effect on the equilibrium velocity field $\mathbf{v}$. The dimensionless neutral drag is a function of the viscosity and the ion-neutral collision time, and acts as a body drag force that opposes the viscous momentum transport. In general, a plasma well suited to produce growing magnetic fields should have $Re \gg 1$, $Rm \gg 1$, $Ma > 1$, and $\chi < Re$.

All flow drive described in this Chapter is driven by $\mathbf{J} \times \mathbf{B}$ torque on the plasma, using discharge current from the emissive LaB_6 cathodes in conjunction with either the edge cusp magnetic field or a uniform axial field generated by external Helmholtz coils. In the former case, a purely hydrodynamic treatment of the flow dynamics can be applied to the unmagnetized plasma core. The relative magnetization is parametrized by the ratio of the gyrofrequency to the collision frequency, ω/ν. In the bulk of the plasma the ion magnetization is much less than unity, meaning that the Lorentz force on ion motion is negligible compared to collisional fluid effects and so the Navier-Stokes equation is sufficient to describe the equilibrium velocity field. Spherical harmonics are used to represent the toroidal and poloidal velocity components [63], and the axisymmetric spherical hydrodynamic system is fully defined by global values of *Re* and χ along with velocity boundary conditions on the surface of the sphere. Since the $\mathbf{J} \times \mathbf{B}$ drive is purely toroidal at the plasma edge, the boundary conditions are defined as

$$\mathbf{v}(r = R) = v_\phi(\theta)\hat{\phi}, \qquad 0 \leq \theta \leq \pi \tag{5.3}$$

where $v_\phi(\theta)$ is a function of the polar angle θ with physical restriction $v_\phi(0) = v_\phi(\pi) = 0$. The remaining computational details are described in the Appendix, along with the formalism for translating discrete cathode stirring loci on at plasma edge into spherical harmonic boundary condition in v.

This hydrodynamic model is used to find the 2D solutions to the Navier-Stokes equation for the MPDX axisymmetric spherical geometry. The fully defined velocity field is then used as the

constant **v** in an iterative eigenmode solver, using the kinematic induction equation to find the magnetic mode with the largest dynamo growth rate $\partial B/\partial t = \gamma_b$. The 'ideal' plasma parameters for dynamo excitation can be found by varying ***Re***, χ, $v_\phi(\theta)$, and finally ***Rm*** to identify the conditions that results in a positive γ_b. For example, a numerical study with counter-rotating hemispheres was conducted with the boundary condition

$$v_\phi(\theta) = \sum_{n=2}^{N} a_n \sin(n\theta), \qquad n \text{ even.} \tag{5.4}$$

Optimizing a_n for the smallest Rm_{crit} results in a set of 'ideal' flow geometries, all of which have a similar shape. In all cases tested ($4 \leq N \leq 14$), the $N = 2$ component of this Fourier expansion results in a northern hemisphere and southern hemisphere with opposite rotation directions, with higher order components adding a more complicated flow reversal near the equator. A more complete description of the numerical results is presented in [64], but as an example the ideal laminar dynamo flow geometry for $N = 4$ is shown in Fig. 5.1. The toroidal flow penetrates far into the center of the spherical plasma thanks to the absence of any neutral drag, and sharp gradients in the radial direction are apparent near the plasma edge. The two poloidal flow cells are driven through centripetal forcing on the fluid by the $v_r = v_\theta = 0$ boundary condition at the plasma edge.

For $Re = 250$, this counter-rotating geometry has a critical ***Rm*** of 309, which is the minimal value found with only four Fourier components defining the v_ϕ. This Rm_{crit} is lower if a higher number of Fourier components is included, as shown in Fig. 5.2. The relationship between ***Re*** and Rm_{crit} is due to the increase in poloidal flow at higher ***Re***: the lower viscosity allows a more efficient transferal of kinetic energy from the toroidal to poloidal direction due to gyroscopic pumping [65]. This trend is demonstrated using the $N = 4$ optimized flow geometry in Fig. 5.3.

These numerical simulations have shown that an MPDX plasma with counter-rotating hemispheres would be dynamo-capable with dimensionless parameters of $Re \sim 250$ and $Rm \sim 250$. Measurements of plasma flow show that while these goals may be achievable at higher input power and lower neutral drag, they are slightly outside the current capabilities of the emissive electrode heating and flow drive.

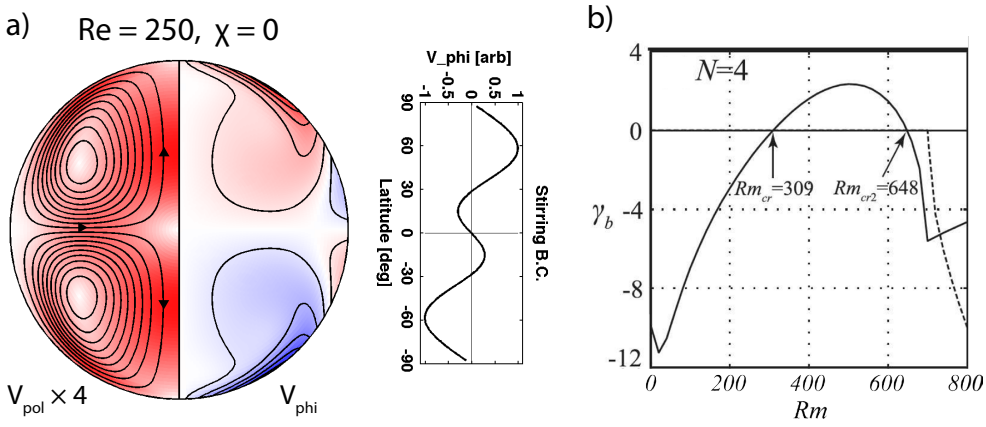

Figure 5.1: Hydrodynamic modeling of ideal $N = 4$ edge flow drive. a) Poloidal (left, with streamlines) and toroidal (right) flow components, with the normalized $v_\phi(\theta)$ boundary condition profile. Not surprisingly, the ideal flow geometry has zero neutral drag. b) The magnetic growth rate γ_b as a function of *Rm*. Due to the laminar flow, this is a 'slow' dynamo with a minimum and maximum limits of *Rm*.

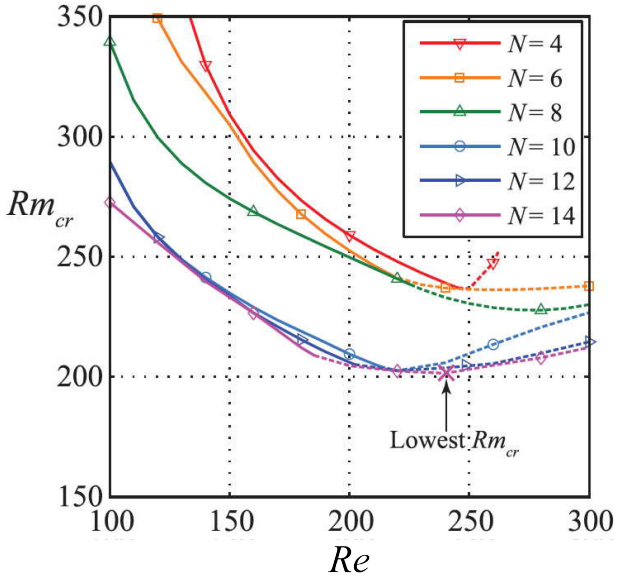

Figure 5.2: Critical magnetic Reynolds number as a function of fluid Reynolds number for optimized flows with different number of driving harmonics. Dashed curves describe flows at marginal hydrodynamic stability. Flows become unstable to nonaxisymmetric hydrodynamic modes above a critical *Re*, rendering the use of a 2D axisymmetric code untenable.

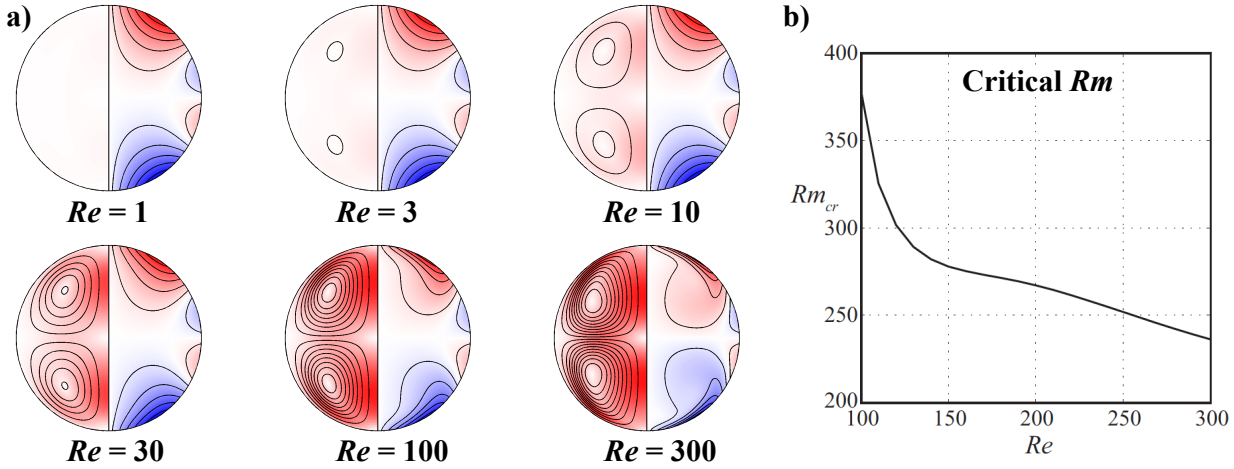

Figure 5.3: Evolution of Navier-Stokes solutions as *Re* is increased to the point of hydrodynamic instability, using the optimized $N = 4$ edge flow profile. The fraction of flow energy in poloidal circulation increases with *Re*, corresponding to a decrease in the critical magnetic Reynolds number Rm_{crit}.

5.2 Edge-driven Flow

The first method of injecting momentum into the bulk unmagnetized plasma uses the application of a J×B torque at the plasma's magnetized edge, as shown in Fig.5.4c. The emissive LaB_6 cathodes are retracted to a radial position closer to the vessel wall ($r \sim 130$ cm), where the magnetic cusp field is significantly stronger, while the molybdenum anodes are inserted well beyond the cusp field ($r \sim 115$ cm). The bulk unmagnetized plasma is thus maintained at a uniform electric potential close to the grounded anodes, and all current drawn from the cathodes is directed radially. Because the cusp field is aligned in the theta direction at the cathode locations, the resulting J×B torque due to the discharged current is in the phi direction. This spins up the edge of the plasma in the direction determined by the polarity of the cusp field: at co-latitudes of ±85,±75,...,±15,±5 flow is in the $-\hat{\phi}$ direction, while at co-latitudes of ±80,±70,...,±20,±10 flow is in the $+\hat{\phi}$ direction. Simulations of this flow drive in a cylindrical cusp device have been conducted [66], and this work is the first experimental demonstration of this technique for differential rotation on an unmagnetized plasma.

Momentum is transported from the spinning edge into the core via ion-ion viscosity, but is lost to charge-exchange collisions with unconfined neutrals. A simple 1D form of the momentum equation is,

$$\frac{\partial v_\phi}{\partial t} = \frac{1}{mn}\left(J_r \times B_\theta\right)_\phi - \frac{v_\phi}{\tau_{in}} + \nu_{ii}\left[\nabla^2 \mathbf{v}\right], \tag{5.5}$$

where the J×B torque is only non-zero at the plasma edge. The transport of momentum inward is calculated using a global value of *Re*, where the classical unmagnetized plasma ion viscosity is calculated using measured T_i and n_e,

$$\nu = 0.96 v_{ti}^2 \tau_{ii} \propto \frac{T_i^{5/2}}{n\sqrt{\mu}}, \tag{5.6}$$

and the neutral drag term is calculated using 1D neutral transport to model the neutral burn-out in the plasma core,

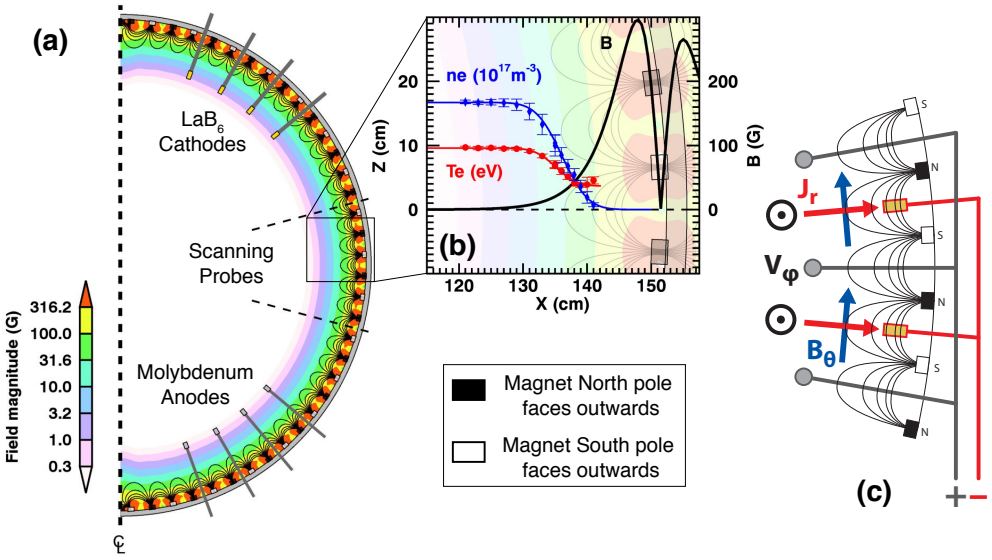

Figure 5.4: Cross-sectional schematic of the MPDX vessel. a) The ring cusp magnetic field is axisymmetric about the z-axis, and electrodes and probes are inserted through ports between magnet rings. b) The cusp field decreases exponentially with radius and confines a homogeneous plasma. c) Edge toroidal flow is driven by a J×B torque near retracted cathodes.

$$n_n(r) = A\frac{\sinh(r/\lambda_{mfp})}{r/\lambda_{mfp}}, \tag{5.7}$$

$$\lambda_{mfp} = v_{th,n}/(\nu_{iz} + \nu_{cx}), \tag{5.8}$$

$$A = \frac{n_{nR}R/\lambda_{mfp}}{\sinh(R/\lambda_{mfp})}, \tag{5.9}$$

where λ_{mfp} is the total neutral mean free path for ionization and charge-exchange collisions, $v_{th,n}$ is the neutral thermal velocity (based on room temperature $T_n = 0.025\,\text{eV}$) and n_{nR} is the measured neutral density at the wall ($r = R$). Thus the amount of neutral burn-out can be encoded in the radial profile of the dimensionless neutral drag χ.

The strategic placement of cathodes allows the edge plasma flow to be arbitrarily controlled, and permits the realization of a wide possibility of differentially rotating flow geometries. Edge flow is primarily a function of cathode latitudinal location and cathode current, as well as the

strength of the edge field at the cathode radial position. The two experimental flow geometries established using this technique are a) counter-rotating hemispheres and b) co-rotating hemispheres. In the spherical expansions of Bullard and Gellman [63], these correspond to the T_1 and T_2 toroidal flow harmonics, and at low enough viscosity both result in one poloidal circulation cell in each hemisphere. The only limitation on the edge rotation profile is the presence of Helmholtz coils which block cathode installation at latitudes of 35 degrees and 30 degrees in both the northern and southern hemispheres. This explains the somewhat conspicuous gap in cathode placement evident in the experimental setups present throughout the remainder of this Chapter.

5.2.1 Counter-rotating hemispheres

The numerical simulations described in Section 5.1 have shown that counter-rotating hemispheres in a sphere produces a laminar flow geometry that is capable of exciting the dynamo instability. In the spherical analog to von-Karman flow, the oppositely directed toroidal flow in the north and south hemispheres can drive two poloidal flow cells, with strong radial outflow from the equator to the poles and a weaker inflow at the equatorial plane. This so-called 'two-vortex' flow can, at large enough *Rm*, advect and amplify a weak transverse seed magnetic field through a stretch-twist-fold mechanism. The transition to positive magnetic growth rates has shown to be very sensitive to details of the flow geometry, and so well-established flow control is important in a dynamo experiment.

To drive counter-rotating flow in MPDX, 8 cathodes were distributed at mid-to-high latitudes in both the north and south hemispheres, and retracted into the cusp so the LaB_6 spanned $130 < r < 135$ cm. Two additional cathodes near the equator were not retracted, and were used only to provide additional heating power without affecting the edge flow. Nine velocity probes were scanned between $r = 90$ and $r = 130$ cm, and their electron density measurements in the plasma core were calibrated to the line-averaged mm-wave interferometer measurements.

Fig.5.5 shows the results from the counter-rotating experiment, including the results of 2D hydrodynamic modeling. The maximum flow velocity was measured to be about 6 km/s, resulting in dimensionless parameters of $Re = 175$, $Rm = 200$, and $\chi(r = R) = 50$. The results of the

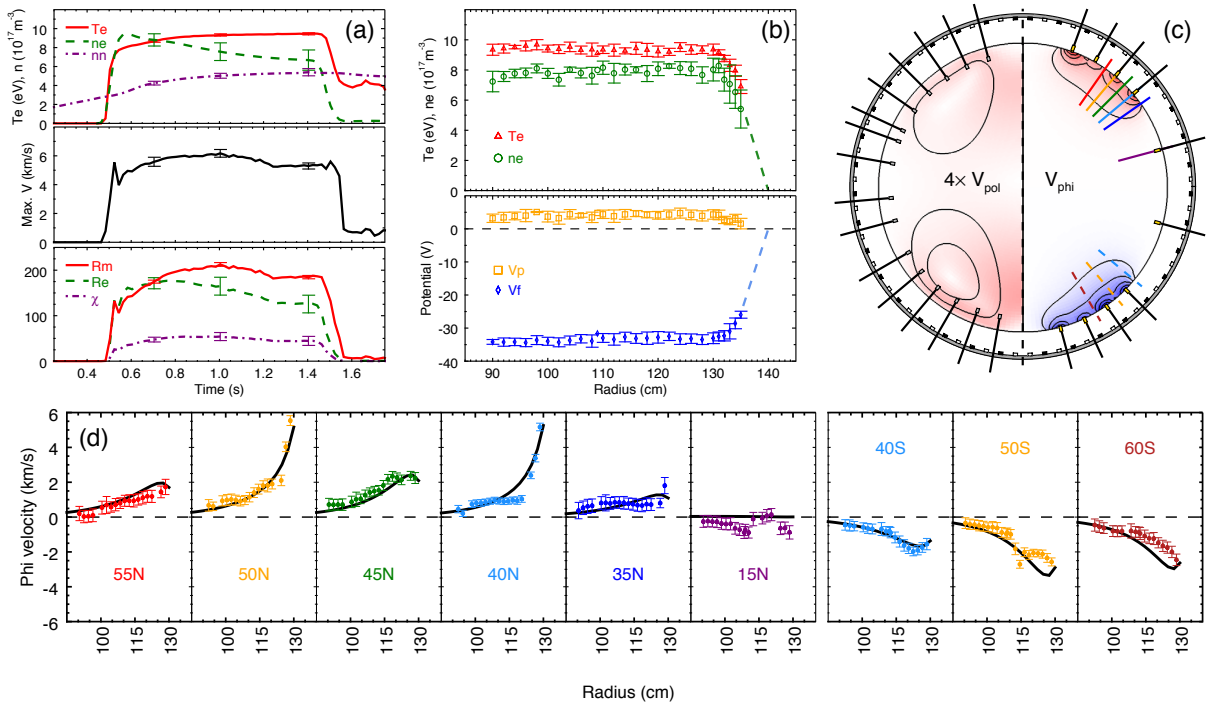

Figure 5.5: Counter-rotating flow measurements in Helium. a) Global plasma parameters; error bars indicate shot-to-shot variation. b) Globally averaged radial profiles from scanning Langmuir probes. c) Electrode and probe placement with modeled flow. d) Velocity probe radial profiles, showing counter-rotating hemispheres. Colors correspond to probe positions in (c), solid lines are modeled flow.

hydrodynamic simulations (with the neutral burn-out profile in χ) compare favorably with velocity probe measurements in MPDX. The two hemispheres are clearly rotating in opposite directions, and the edge momentum is transported inward at rates close to what classical viscous diffusion would predict. At these moderate ionization fractions the neutral drag is a significant factor in the momentum transport equation, driving toroidal flow to zero by $r = 90$ cm, the maximum insertion depth of the velocity probe array. The simulated flow geometry is globally suppressed compared to the ideal, $\chi = 0$ flow models in Fig. 5.1: not only does the edge flow fail to penetrate as far using the measured dimensionless parameters, but the poloidal flow is a much smaller fraction of the

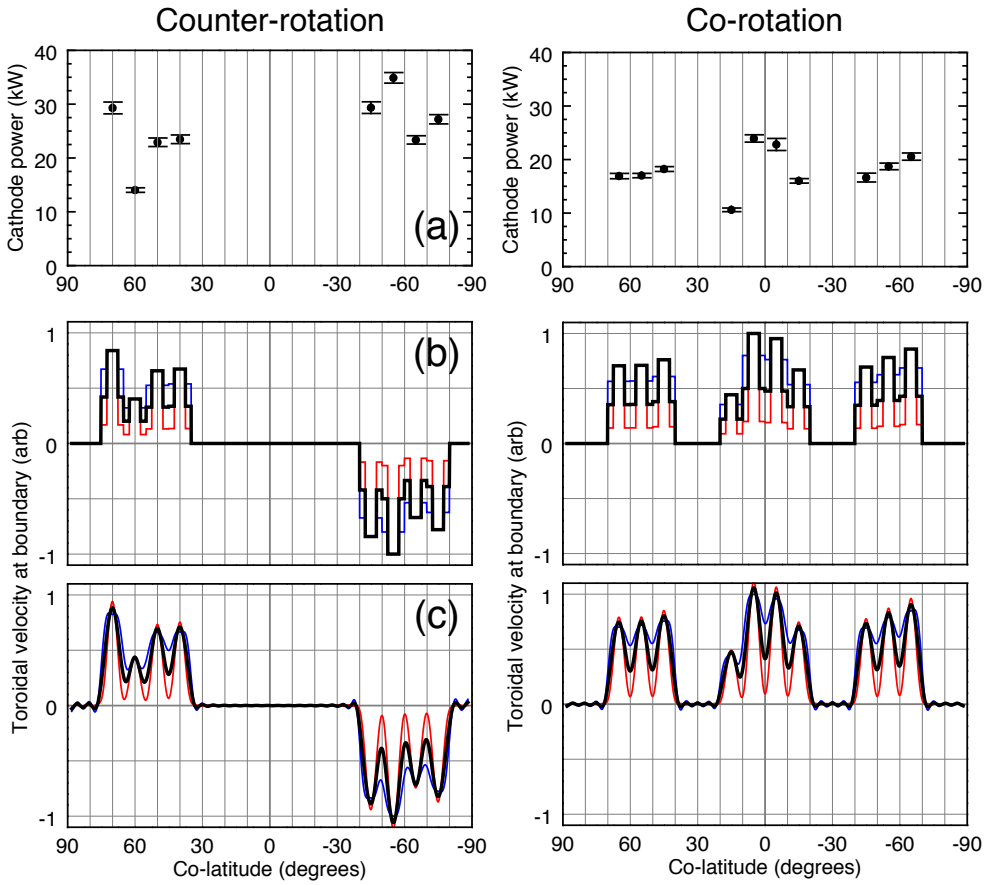

Figure 5.6: Process for determining hydrodynamic model BCs based on experimental data. a) Measurements of emissive cathode input power as a function of latitudinal position. b) Discretized v_ϕ boundary condition based on cathode power. c) Spherical harmonic expansion of discrete edge flow drive. The decrease in edge flow between nearby cathodes is a fitting parameter, and flow measurements are best fit by an inter-cathode scaling of 0.5, shown in black (red=0.2 and blue=0.8)

total flow energy. While the velocity probes measure both toroidal and poloidal flow components, the poloidal measurements are within error bars of zero, similar to the simulated v_θ.

Fig.5.5d shows toroidal velocity measurements at the nine different polar positions indicated in Fig.5.5c compared to simulation results. The variation in profile magnitude and shape is a function of the modeled boundary conditions, which are based on the emissive cathode latitudinal positions and measured power input. Fig. 5.6 shows the derivation of the modeled boundary conditions, both

for counter-rotation as well as the co-rotation scheme discussed in Section 5.2.2. This arrangement explains the relatively larger flows measured by probes at 50 N and 40 N: these probes are the only ones that share a magnet ring with a stirring cathode. The probe at 15 N does not show a similar amount of flow because the cathode at 15 N is inserted past the cusp field, and thus is not imparting any $\mathbf{J} \times \mathbf{B}$ torque to the local plasma.

5.2.2 Co-rotating hemisphere

A second stirring geometry was tested in MPDX, in which all cathodes were installed so as to drive flow in the same direction. This co-rotating flow is designed to be a simple model of the differential flow observed in the solar convective zone, where the equatorial period of 25 days is much shorter than the polar period of 34 days [67]. For this experiment, ten cathodes were distributed between the north and south poles and retracted into the cusp field to $130 < r < 135$ cm. Unlike the counter-rotating flow experiment, there is no velocity null at the machine equator, and so stirring cathodes can be placed at the equator as well as at mid-to-high latitudes. Five velocity probes were scanned, with four of them located in the same magnet ring as a stirring cathode.

Fig.5.7 shows the results of the co-rotating experiment, and their comparison to the hydrodynamic model results. The electron density and neutral density was significantly less than the counter-rotating experiment, resulting in a lower values of $Re \sim 100$ and $\chi \sim 20$ even at a lower ionization fraction. Comparable magnitudes of *Te* and the maximum velocity ensured that *Rm* remained high, close to 200. The Langmuir probe radial profiles in Fig.5.7b once again indicate a homogeneous core, with the difference of a slight increase in temperature and density at the radial position of the LaB_6 cathodes. This local increase in plasma pressure is frequently observed in magnet rings with retracted stirring cathodes, and is presumably present in the counter-rotating experiment as well. It is more evident here only due to the increased number of probes in cathode rings. Note that the inputs to the corresponding hydrodynamic simulation were calculated using $R = 130$ cm, taking into account the observation that the core volume of homogeneous viscosity and *Re* extends out only as far as the volume of constant n_e.

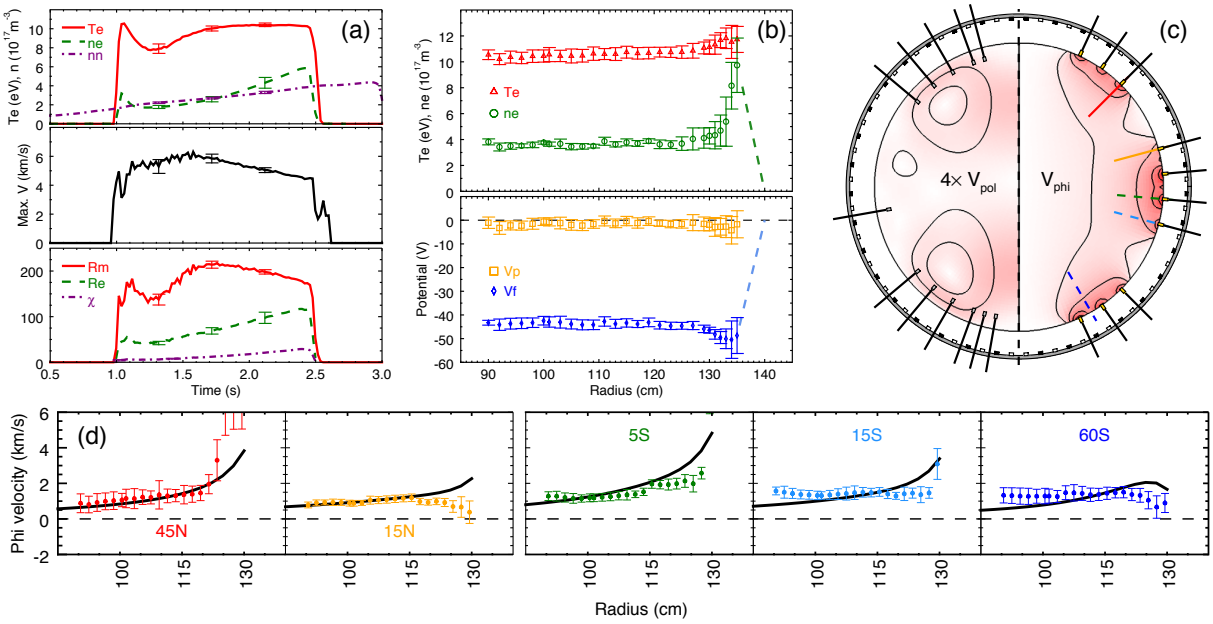

Figure 5.7: Co-rotating flow measurements in Helium. a) Global plasma parameters; error bars indicate shot-to-shot variation. b) Globally averaged radial profiles from scanning Langmuir probes. c) Electrode and probe placement with modeled flow. d) Velocity probe radial profiles, showing co-rotating hemispheres. Colors correspond to probe positions in (c), solid lines are modeled flow.

The measured velocity profiles in Fig.5.7d show a uniform rotation direction, with relatively small gradients and a faster flow in the plasma core. This is partially attributable to the lack of a velocity null near the equatorial plane, which in the counter-rotating case served to further suppress flow in the plasma core. The smaller values of *Re* and χ here also serve to increase radial momentum flux and decrease the loss of momentum to charge-exchange. A downside to decreased *Re* would be decreased poloidal flow, and the modeled flows agree with probe measurements of v_θ to the extent that both are below the noise level of Mach probe error bars. Toroidal velocity data, on the other hand, matches the latitude-dependent flow magnitude based on the cathode boundary conditions shown in Fig. 5.6. The measured velocity gradients are a poorer match to simulation results, at least at radial positions closer to the edge cusp field; this may be due to a lack of spherical symmetric in neutral out-gassing that is more apparent thanks to the smaller flow gradients in the co-rotating geometry.

5.3 Volumetric-driven Flow

The second method of stirring MPDX plasmas is designed to generate flow profiles appropriate for the study of the MRI. In astrophysical accretion disks, the plasma in the disk itself follows a Keplarian velocity profile,

$$\Omega(r) = \sqrt{GM/r^3}, \tag{5.10}$$

in which plasma close the axis of rotation is flowing at much higher velocities than plasma at larger cylindrical radii. This radial dependence is opposite that of the edge-driven flows described above, and requires a different flow drive technique. Instead of limiting $\mathbf{J} \times \mathbf{B}$ torque to the magnetized edge region of MPDX plasmas, a uniform axial magnetic field is externally applied using the 4.07 m diameter Helmholtz coil set. Discharge current that flows in the cylindrical radial direction will generate a $\mathbf{J} \times \mathbf{B}$ torque throughout the entire volume of the plasma, and the geometric effects of current continuity will result in a current density that decreases with cylindrical radius. The resulting velocity profile has maximum flow near the axis of rotation, which slows to a nearly stationary boundary condition at the equatorial plasma edge. In order to force current to flow perpendicular to the applied axial field, LaB_6 cathodes are inserted near the machine equator while anodes are inserted near the north and south poles, as shown in Fig.5.8. A weak axial field was applied ($B_z = 0.5\,\mathrm{G}$ for helium stirring, $B_z = 2.0\,\mathrm{G}$ for argon stirring).

MRI-capable flow must meet two criteria. First, the angular velocity must decrease with radius. Second, the flow must be hydrodynamically stable, a condition that requires the angular momentum increase with (cylindrical) radius [68]. That is,

$$\frac{d\Omega}{dr} < 0, \quad \frac{d(r^2\Omega)}{dr} > 0. \tag{5.11}$$

Eight velocity probes were used to measure plasma flow in both hemispheres, in both helium and argon plasmas. Velocity probe measurements are shown in Fig.5.9, where data points are identified by probe latitude and hemisphere and correspond to the colored radial chords shown in Fig. 5.8. The probes were distributed so as to completely cover the radial interval spanned by the

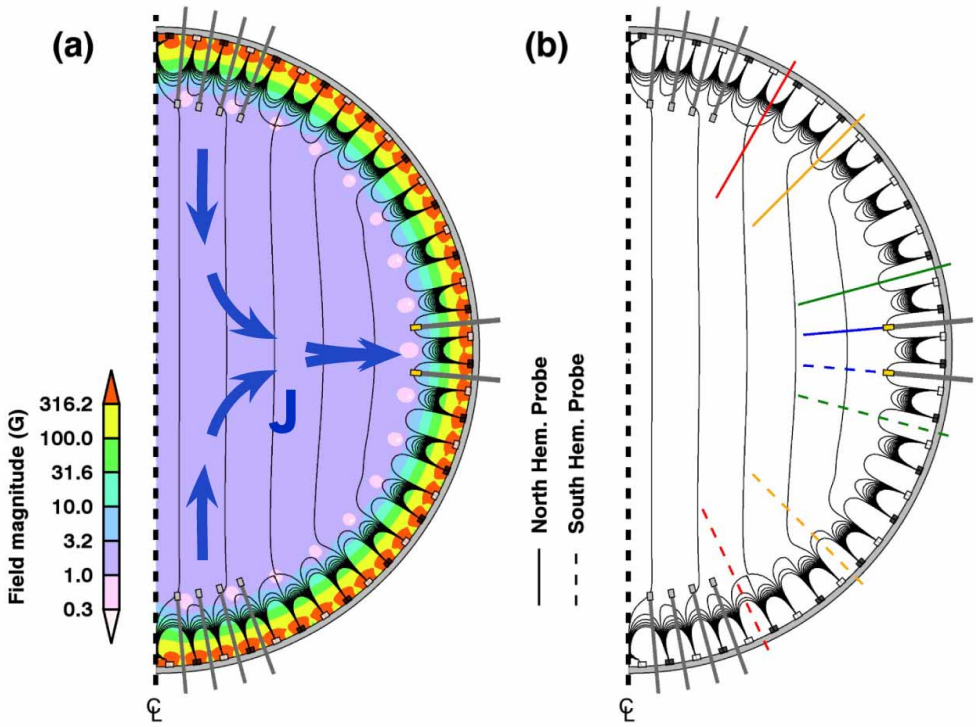

Figure 5.8: Experiment setup for volumetric-driven flow: cathodes (gold) are at equator, anodes (grey) are at poles. a) Discharge current is forced across the axial field ($B_z = 2.0\,\mathrm{G}$). b) Scanning probes are distributed across the northern and southern hemispheres.

polar anodes and equatorial cathodes. One thing that is immediately apparent is that the measured velocity is symmetric about the vessel equator. This is not a result of well-balanced input current from the two cathodes; instead, it suggests that the fluid Reynolds number is large enough such that Ferraro's theorem is applicable. Simply put, Ferraro's theorem states that, in an inviscid conducting fluid, contours of constant magnetic flux are also contours of constant angular velocity. Since the axial field is symmetric about the machine equator, this would make the toroidal flow similarly mirrored.

Global parameter measurements for the helium and argon plasmas are shown in Fig.5.10. The two ion species are an interesting contrast, both in dimensionless parameters and velocity profile. Helium, with a low ion temperature of $T_i = 0.36\,\mathrm{eV}$, has a relatively high *Re*, indicating that viscosity is low. The resulting flow is well-fit by the Couette flow in a cylinder,

$$v_\phi = Ar + B/r \tag{5.12}$$

The inner region is marginally stable to the hydrodynamic instability, but the radial gradient in angular momentum becomes negative outside of $r \sim 90\,\text{cm}$. This indicates that the MRI may be active in the inner core of the rotating plasma column, and could even be modifying the equilibrium velocity profile to push the outer core into a hydrodynamically unstable regime. A dearth of modeling on this flow drive geometry limits the physical intuition that can be applied to these measurements, but the overall data shows promise for future MRI studies in helium. The Alfven Mach number is consistently larger than unity and the fluid Reynolds number is large ($Re \sim 200$), indicating that the axial field is still weak compared to the generated flows and that viscosity is negligible. Both of these conditions are requirements for exciting growing MRI modes that are strong enough to resist viscous damping or Lorentz force modifications.

In contrast, the argon measurements have a much lower *Re* thanks to the much higher ion temperature of $T_i = 1.29\,\text{eV}$. This indicates that viscosity is much larger and will play a larger role in regulating velocity gradients. The measurements show a flat velocity profile out to $r = 90\,\text{cm}$, which is not well-fit by a Couette-driven flow. The inner flow is therefore much more stable than the marginal amount, with a constant rate of radial increase in the angular momentum. Still, the outer core of the rotating plasma column is hydrodynamically unstable, and should undergo a transition to non-axisymmetric modes due to the Rayleigh criterion.

It should be emphasized that no velocity fluctuations have been measured over the course of all MPDX flow experiments. The lack of fluid instability signatures perhaps points to the enhanced role of either neutrals or viscosity in damping potential fluid turbulence. In the case of volumetric helium flow, a relatively low ionization fraction means that there is little neutral burn-out in the plasma core, leading to significant neutral drag on the flowing ions. The volumetric $\mathbf{J} \times \mathbf{B}$ torque dominates the momentum loss to neutrals, but the smaller fluctuations from a transition to turbulence could be more susceptible to damping. A similar rational can be applied to the volumetric argon flow, which while being highly ionized has a very small fluid Reynolds number ($Re \sim 18$).

(a) Helium volumetric flow

(b) Argon volumetric flow

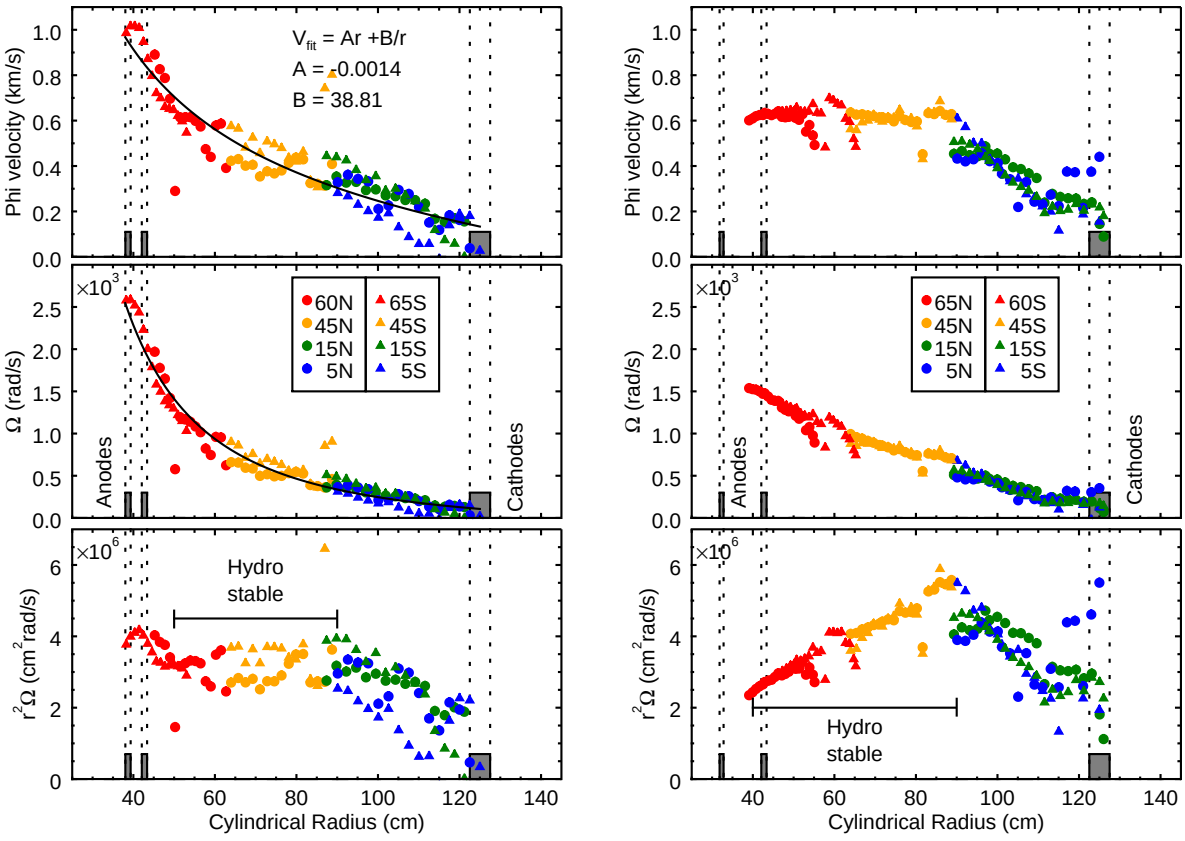

Figure 5.9: Velocity probe measurements of volumetric flow in helium (left) and argon (right) plasma. Each gas species meets the MRI criteria $d\Omega/dr < 0$ over the entire measured volume, as well as being hydrodynamically stable at internal radii. Furthermore, mirrored flow velocities in the northern and southern hemispheres suggests a confirmation of Ferraro's theorem.

This increase in viscosity could act to smooth out turbulent fluctuations and prevent the observed angular momentum profiled from being truly unstable.

(a) Helium volumetric flow (b) Argon volumetric flow

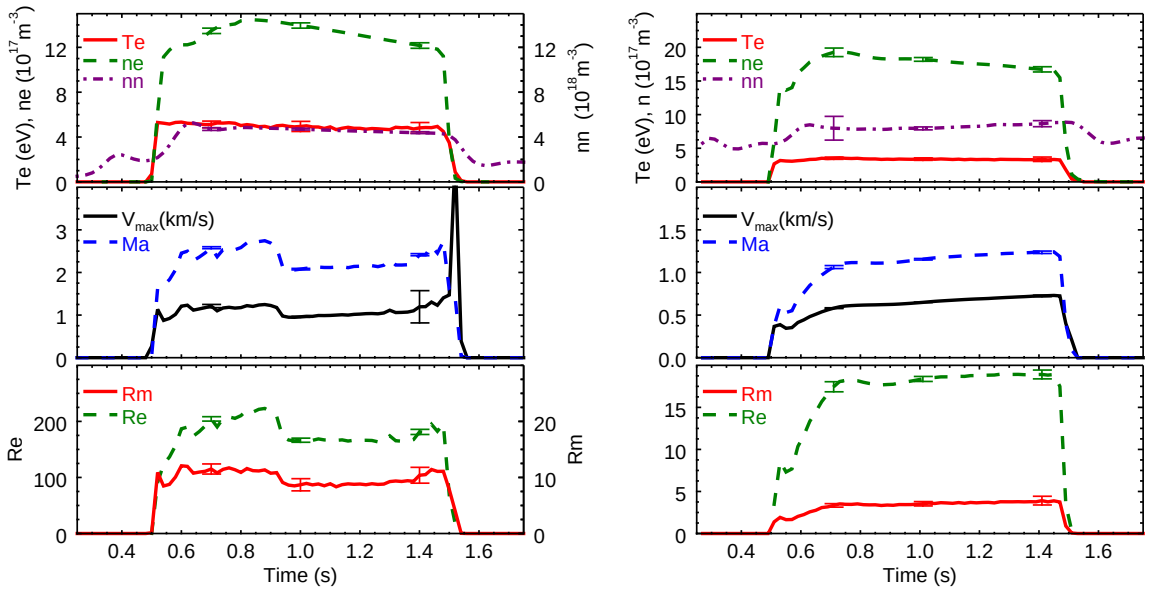

Figure 5.10: Global measurement for helium (left) and argon (right) volumetric flow drive. Core $T_i = 0.36\,\text{eV}$ in helium, $T_i = 1.29\,\text{eV}$ in argon.

5.4 Prospects for instability measurements

The various flow geometries described in this Chapter are all designed to investigate the physical processes underlying astrophysical instabilities. However, the measured flows and dimensionless parameters are not sufficient to match numerical models that predict magnetic mode growth. In all cases, *Rm* is too low in comparison to the neutral drag force and the plasma viscosity. Specifically, the hydrodynamic flow modeled using the cathode placement and input power for the counter-rotating and co-rotating experiments can be used as the kinematic velocity field in the induction equation solver discussed in Section 5.1. The results are as expected: the calculated magnetic eigenmodes all have negative growth rates, and no magnetic amplification is predicted. Of course, the measured flow profiles are not close to the optimized flow profiles; the presence of neutral drag as well as the lack of flow reversal at the equator means that the critical magnetic Reynolds number for the experimental flows is much larger than the ideal Rm_{crit} shown in Fig. 5.2.

It remains to be seen whether the non-ideal flow geometry is the main reason that experimental flows are not predicted to generate growing magnetic fields. What is certainly true, though, is that the plasma parameters fall short of the desired Re, Rm, and χ. The results discussed in Chapter 4 suggest that the use of discharge current heating is by itself insufficient to produce plasmas that meet these requirements. The unfavorable coupling between input power, plasma density, and neutral density means that a high-power power must have a large electron density, which in turn requires a large neutral density. The two parameters Re and χ are tied together, and it is difficult to increase the former while decreasing the later. An added complication comes from the dependence of Re on the ion temperature. An ideal dynamo-capable plasma would have a large plasma density but cold ions. Unfortunately, these two parameters are once again linked by electron-ion heating, which become more efficient at the higher collisionalities inherent in a dense plasma. The change in ion confinement at the anode sheath as a function of V_p furthers this undesirable coupling.

It appears that the best path forward for optimized plasma conditions involves the introduction of electron cyclotron heating, which should break most of these couplings. Future work should move towards this goal, which should also include improving the MPDX magnetic diagnostic suite in preparation for more sensitive magnetic measurements. This Chapter has shown that experimental control of the plasma hydrodynamics in MPDX is possible, and the fundamental mechanics of flow drive are now well understood. The experimental detection of flow-driven MHD instabilities is the next step in this next generation of plasma astrophysics.

Chapter 6

Conclusion

This thesis is the culmination of six years of graduate work in the physics department at the University of Wisconsin - Madison. The Madison plasma dynamo experiment was designed and constructed during this timeframe, and the data presented herein are the first experimental plasma results from this new device. The author of this thesis was the primary researcher on many of the hardware and software systems described above, and was involved in the operation and analysis of everything mentioned in this thesis. The LaB_6 emissive cathodes and combination Langmuir/Mach probe array are two examples of hardware projects conducted exclusively by the author; this includes the filament power supplies, the remote motor control, and the discharge bias power supply installation. The linear transport and global particle/power balance models are also owned by the author, while the hydrodynamic and induction numerical solvers were expansions of previous work. Finally, the extensive data acquisition and logbook databases were built and managed by the author, in addition to the LabView experimental control interface and data visualization. What was originally (Jan. 2012) an empty laboratory space has now been turned into a fully operational, intermediate-sized plasma device with a growing number of graduate students and collaborators. It is this author's hope that the effort and time put into making the MPDX hardware and software both rugged and user-friendly will continue to pay dividends for years to come.

6.1 Summary of Thesis

The main goals of this thesis were to create and characterize a highly conducting, low viscosity plasma in a large, unmagnetized volume, and to create a flowing plasma with applications to the

study of flow-driven MHD instabilities like the dynamo and the MRI. These goals was achieved through the design and construction of a new plasma device which uses a cylindrically symmetric spherical boundary ring cusp geometry built from strong permanent magnets to confine a large (R=1.5 m), warm ($T_e < 20\,\text{eV}$), dense ($n_e < 5 \times 10^{18}\,\text{m}^{-3}$), unmagnetized plasma. The plasma is stirred via $\mathbf{J} \times \mathbf{B}$ torques using current drawn from emissive cathodes at the magnetized plasma edge, and maximum flow speeds of 6 km/s and 3 km/s have been measured in helium and argon plasmas, respectively. High Alfven Mach number flows have also been generated by drawing current across a global axial magnetic field, resulting in a velocity geometry conducive to MRI experiments.

In order to generate plasmas with the desired global dimensionless parameters *Re* and *Rm*, the plasma confinement was characterized and the relationship between plasma parameters and conductivity/viscosity important for flow dynamics was parameterized. Particle losses to the magnets were measured directly using a high spatial resolution array of Langmuir probes embedded in a plasma tile, complimented by 1D and 2D Langmuir probe scans in the plasma edge. Particle balance and neutral density measurements show the plasmas are highly ionized and that the particle confinement is controlled by ambipolar cross field diffusion through the cusp field at the boundary and parallel streaming losses to the magnets. A numerical analysis of the details of ambipolar transport in the ring cusp geometry show that the total wall loss area is determined by this balance between diffusion and ionization, and numerical predictions of the edge plasma gradient are good qualitative matches to probe measurements. Mach probe measurements of intrinsic plasma rotation due to diamagnetic and $\mathbf{E} \times \mathbf{B}$ drifts are also shown to be consistent with the density gradients and ambipolar electric field that result from this transport model. The level of neutral burn-out is shown to be a key difference in the cusp loss area between helium and argon plasmas, and reveals the possibility of non-monotonic plasma flux profiles when inserted electrode area is a significant particle loss channel.

In addition to particle confinement, plasma heating is also a critical component of generating highly conducting plasmas. The details of discharge heating in MPDX plasmas was elucidated by

an experimental campaign studying discharge behavior as the total anode area was varied. Analysis of the balance between input and output discharge current has shown that the anode sheath controls the plasma potential, thanks in large part to the ceramic tiles that electrically insulate the plasma from the vessel wall. At large anode current densities, the potential drop at the anode sheath is shown to experience a rapid transition that drives the bulk plasma potential to hundreds of volts below ground, resulting in a power balance that makes continued plasma heating impossible. This phenomenon of self-extinguishing plasmas imposes an upper limit on discharge heating, preventing operational access to the full *Re*, *Rm* parameter space.

Plasma flow experiments were conducted based on the findings from these confinement and heating studies, resulting in measurements of several interesting flow geometries. An array of combination Langmuir/Mach probes were used to diagnose ion flows around the entire perimeter of the device, as well as at insertion depths of up to 45% of the total spherical radius. Flow experiments are categorized into two types of flow, both using $\mathbf{J} \times \mathbf{B}$ torque from the emissive cathode discharges to impart momentum to the plasma. Edge-driven flow uses cathodes that have been retracted into the ring cusp field, driving toroidal flow that is localized to the plasma plasma edge. Velocity measurements show that this momentum is transported into the unmagnetized bulk via ion viscosity, but is lost to neutral charge-exchange collisions. Both counter-rotating and co-rotating boundary conditions show an unprecedented level of control over the differential rotation of the bulk plasma, and hydrodynamic models of the bulk spherical plasma agree with velocity probe measurements. These flow geometries are also shown to be ideal for the generation of a laminar, 'slow' dynamo; however, plasma heating limitations suggest that discharge heating is not sufficient to achieve the desired combination of low neutral drag and low T_i with high n_e and T_e.

A second set of flow experiments demonstrated the novel production of MRI-capable flow profiles, using the cylindrical symmetry to drive cathode discharge current radially across a weak axial magnetic field. The resulting $\mathbf{J} \times \mathbf{B}$ torque is no longer localized to the plasma edge, and the geometric constraints on the current density results in a rotation profile where $d\Omega/dr < 0$, ideal for MRI studies. This stirring technique also overcomes several of the limitations inherent in viscously coupled flow drive, including the significant reduction in the importance of neutral

drag and plasma viscosity. However, the plasma potential was found once again to be sensitive to discharge current density and plasmas were observed to self-extinguish if the axial magnetic field was too strong.

6.2 Future Work

In conclusion, a clearer path towards both the dynamo and the MRI has been characterized. Several additions and modifications to the experimental design are recommended if these flow-driven MHD instabilities are to be successfully studied on MPDX.

First and foremost, the plasma heating should be decoupled from the emissive discharge current. Work is currently underway to complete the installation of an ECH system, allowing electron heating independent of the plasma potential and electron and neutral densities. Future ECH operation will utilize the established control of LaB_6 temperature to regulate emission current and avoid self-extinguishing plasmas while still maintaining the required levels of electron heating. Since high power input will be possible at low neutral pressures, the charge-exchange neutral drag can be minimized and ionization fractions in both helium and argon plasmas should approach unity. The resulting increases in electron temperature and density will extend the experimental parameter space to larger values of *Rm* and *Re* and open up the possibility of studying turbulent, 'fast' dynamos.

The addition of ECH heating will also expand the flow-drive capabilities of MPDX, increasing the bulk plasma velocity and permitting investigations of Ferarro's theorem and toroidal magnetic wind-up (the omega effect). MRI conditions should be possible with slightly faster rotation and higher density (lower viscosity). An increase in flow speed and a decrease in viscosity will enhance the efficiency of poloidal flow generation, perhaps increasing the energy in the predicted poloidal flow cells to measurable levels. The development of an array of sensitive magnetic Hall probes is currently underway to help diagnose the magnetic signatures of these processes. Eventually, a global set of magnetic flux loop sensors could provide detailed measurements of the global field structure and begin to identify the harmonic composition of magnetic activity.

Finally, the possible flow drive geometries in this experiment have only just begun to be realized. The complexity of $\mathbf{J} \times \mathbf{B}$ differential rotation extends far beyond the simple counter-rotating and co-rotating hemisphere scenarios presented in this thesis. For example, the injection of small wavelength helicity is as easy as alternating the flow drive direction in each magnet ring. This high-order harmonic boundary condition might drive MHD turbulence in the plasma core and would provide an interesting backdrop for 'fast' dynamo research. The MRI-capable volumetric flow drive could also be expanded to include more complex magnetic field geometries. For example, replacing the external axial field with a quadrupolar field could allow for counter-rotating vortex flow similar to the Bullard Gellman geometry studied in previous liquid metal experiments.

In short, this thesis has set the stage for a wide variety of plasma experiments on a novel confinement device. It is this author's hope that this work serves as a solid foundation to the many discoveries that await future experimental researchers in the field of astrophysical MHD instabilities.

Appendix A: Vacuum Field Equations

A.1 Analytic equations for Vector Potential

For a single axisymmetric loop of current centered on the origin, the only non-zero component of the vector potential is in the $\hat{\phi}$ direction [69],

$$A_\phi(r,\theta) = I_0 \left(\frac{a}{\rho}\right) \frac{(2-k^2)K(k) - 2E(k)}{k^2}, \tag{A.1}$$

where $K(k)$ and $E(k)$ are the complete elliptic integrals of the first and second kinds, a is the loop radius in meters, $I_0 = \mu_0 I/\pi$ with I the current in amps, and

$$k^2 = \frac{4ar\sin\theta}{\rho^2}, \tag{A.2}$$

$$\rho^2 = a^2 + r^2 + 2ar\sin\theta. \tag{A.3}$$

The first derivatives of A_ϕ are

$$\frac{\partial A_\phi}{\partial \alpha} = \frac{I_0 a}{(\rho k^2)^2}\left[\rho k^2\left(C_{\alpha 1} - 2\frac{\partial E}{\partial \alpha}\right) - C_{\alpha 2}\left((2-k^2)K - 2E\right)\right], \tag{A.4}$$

where $\alpha = r, \theta$ and

$$C_{\alpha 1} = \frac{\partial}{\partial \alpha}\left[(2-k^2)K\right] = (2-k^2)\frac{\partial K}{\partial \alpha} - 2k\frac{\partial k}{\partial \alpha}K, \tag{A.5}$$

$$C_{\alpha 2} = \frac{\partial}{\partial \alpha}\left[\rho k^2\right] = k^2\frac{\partial \rho}{\partial \alpha} + 2\rho k\frac{\partial k}{\partial \alpha}. \tag{A.6}$$

The second derivatives of A_ϕ are

$$\begin{aligned}\frac{\partial}{\partial \beta}\frac{\partial A_\phi}{\partial \alpha} =& \frac{I_0 a}{(\rho k^2)^3}\Bigg[\rho k^2\Bigg\{C_{\beta 2}\left(C_{\alpha 1} - 2\frac{\partial E}{\partial \alpha}\right) + \rho k^2\left(\frac{\partial C_{\alpha 1}}{\partial \beta} - 2\frac{\partial^2 E}{\partial \beta \partial \alpha}\right) \\ &- \frac{\partial C_{\alpha 2}}{\partial \beta}\left((2-k^2)K - 2E\right) - C_{\alpha 2}\left(C_{\beta 1} - 2\frac{\partial E}{\partial \beta}\right)\Bigg\} \\ &- 2C_{\beta 2}\left\{\rho k^2\left(C_{\alpha 1} - 2\frac{\partial E}{\partial \alpha}\right) - C_{\alpha 2}\left((2-k^2)K - 2E\right)\right\}\Bigg]\end{aligned} \tag{A.7}$$

which, for $\alpha = \beta$, simplifies to,

$$\begin{aligned}\frac{\partial^2 A_\phi}{\partial \alpha^2} =& \frac{I_0 a}{(\rho k^2)^3}\Bigg[\rho k^2\Bigg\{\rho k^2\left(\frac{\partial C_{\alpha 1}}{\partial \alpha} - 2\frac{\partial^2 E}{\partial \alpha^2}\right) - \frac{\partial C_{\alpha 2}}{\partial \alpha}\left((2-k^2)K - 2E\right)\Bigg\} \\ & - 2C_{\alpha 2}\Bigg\{\rho k^2\left(C_{\alpha 1} - 2\frac{\partial E}{\partial \alpha}\right) - C_{\alpha 2}\left((2-k^2)K - 2E\right)\Bigg\}\Bigg]\end{aligned} \tag{A.8}$$

A.2 Analytic equations for Magnetic Field

The magnetic field components are

$$B_r = \frac{1}{r\sin\theta}\frac{\partial}{\partial \theta}(\sin\theta A_\phi), \tag{A.9}$$

$$B_\theta = -\frac{1}{r}\frac{\partial}{\partial r}(r A_\phi), \tag{A.10}$$

$$B_\phi = 0. \tag{A.11}$$

In order to solve the field line tracing differential equations, the gradients of the vacuum field must also be analytically known.

$$\frac{\partial B_r}{\partial r} = \frac{1}{r}\left(\frac{\partial^2 A_\phi}{\partial r \partial \theta} + \cot\theta\frac{\partial A_\phi}{\partial r}\right) - \frac{1}{r^2}\left(\frac{\partial A_\phi}{\partial \theta} + \cot\theta A_\phi\right), \tag{A.12}$$

$$\frac{\partial B_r}{\partial \theta} = \frac{1}{r}\left(\frac{\partial^2 A_\phi}{\partial \theta^2} + \cot\theta\frac{\partial A_\phi}{\partial \theta} - \csc^2\theta A_\phi\right), \tag{A.13}$$

$$\frac{\partial B_\theta}{\partial r} = -\frac{\partial^2 A_\phi}{\partial r^2} - \frac{1}{r}\frac{\partial A_\phi}{\partial r} + \frac{A_\phi}{r^2}, \tag{A.14}$$

$$\frac{\partial B_\theta}{\partial \theta} = -\frac{\partial^2 A_\phi}{\partial \theta \partial r} - \frac{1}{r}\frac{\partial A_\phi}{\partial \theta}, \tag{A.15}$$

where

$$\frac{\partial B}{\partial \alpha} = \frac{B_r}{B}\frac{\partial B_r}{\partial \alpha} + \frac{B_\theta}{B}\frac{\partial B_\theta}{\partial \alpha}. \tag{A.16}$$

The conversions to cylindrical coordinates are

$$B_x = B_r \sin\theta + B_\theta \cos\theta, \tag{A.17}$$

$$B_z = B_r \cos\theta - B_\theta \sin\theta, \tag{A.18}$$

and

$$\frac{\partial B}{\partial x} = \frac{x}{r}\frac{\partial B}{\partial r} + \frac{z}{r^2}\frac{\partial B}{\partial \theta}, \tag{A.19}$$

$$\frac{\partial B}{\partial z} = \frac{z}{r}\frac{\partial B}{\partial r} - \frac{x}{r^2}\frac{\partial B}{\partial \theta}. \tag{A.20}$$

A.3 Field line tracing

In order to solve the 1D particle balance problem with flux averaging, a field line tracing program is required. The unit length parallel to the magnetic field is expressed as,

$$dl = \sqrt{dx^2 + dz^2}, \quad \frac{dz}{dx} = \frac{B_z}{B_x} \tag{A.21}$$

where the relation of field line slope to B_x and B_z is a consequence of $\hat{l} \times \hat{b} = 0$, where $\hat{l} = dx\hat{x} + dz\hat{z}$. A field line tracing program solves the differential equation,

$$x'(z) = \frac{B_x(x,z)}{B_z(x,z)} \tag{A.22}$$

beginning at an initial value of $z = 0$, $x(0) = x_0$ and ending when the magnet face has been reached, ie:

$$r = \sqrt{x^2 + z^2} > r_{mag} = 150.18\,\text{cm}. \tag{A.23}$$

A.4 Vacuum field plots

Simulating the entire MPDX cusp field involves the application of the magnetostatic equations outlined in Sections A.1 and A.2 to the exact ring cusp geometry described in Chapter 2. A field

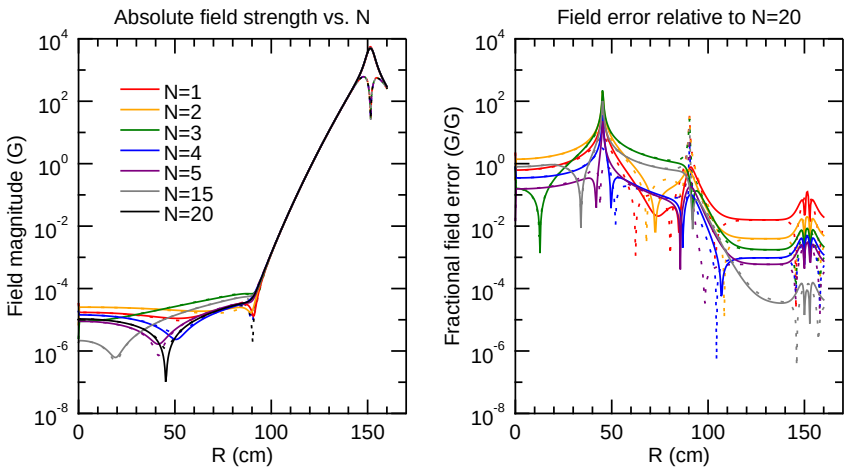

Figure A.1: Field error as a function of the number of discrete current rings per magnet ring sidewall, compared to a 20-ring calculation. Solid curves indicate radial chords that terminate at the center of a magnet rind, dotted curves bisect magnet rings.

generated by a permanent magnet can be represented in this manner by continuous sheets of surface current on the faces of the magnet, such that

$$\mathbf{J_{ms}} = \mathbf{M} \times \hat{\mathbf{n}} \tag{A.24}$$

where $\mathbf{M}$ is the magnetization and $\hat{\mathbf{n}}$ is the normal unit vector for each side of the magnet ring. Since each magnet ring is magnetized in the radial direction, the analogous surface current flows in the $\hat{\phi}$ direction on the side walls of each ring. This ribbon of surface current is approximated by a finite number of discrete 1D rings of current. Fig. A.1 shows the results of a convergence calculation, indicating that using 4 discrete current rings will keep the relative field error below 0.1% (over the entire magnetized edge).

This magnetostatic calculation is calibrated to a series of Hall probe measurements taken near the vessel wall, shown in Fig. A.2. The probe measurements are an excellent fit to the analytic field, which ideally would fall to microGauss levels in the center of the vessel. However, the Earth's magnetic field prevents this from occurring. A set of single turn Helmholtz coils are installed on MPDX to cancel out the vertical component of Earth's field (~ 0.5 G), but the remaining horizontal

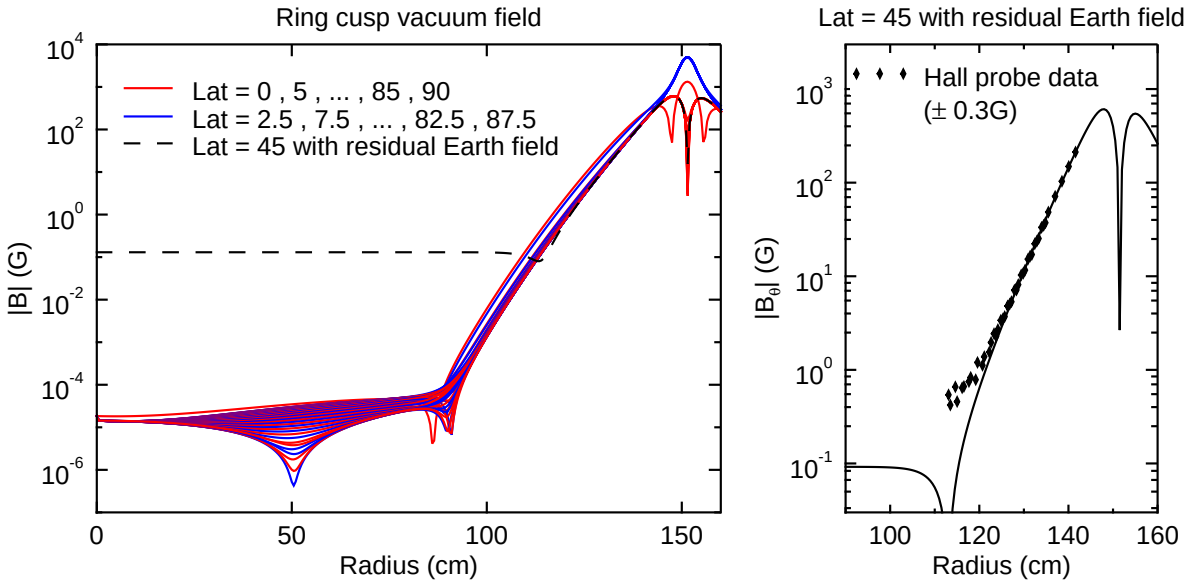

Figure A.2: Modeled magnetic field along radial chords. With correction coils on, the residual Earth field is ~ 0.1 G

component is still much stronger than the true vacuum field. This baseline field strength is shown in Fig. A.2, and is about 0.1 G at the vessel center.

A contour plot of the vacuum field magnitude is shown in Fig. A.3. As expected, the cusp field falls off exponentially with radius. At $r \sim 90$ cm, this trend levels off and the combined interference of the 36 magnet rings results in a homogeneously magnetized central core.

The direction of the vacuum field (without the addition of Earth's field) has a high order of variability in the magnetized edge. Fig. A.4 shows the relative magnitude of the cylindrical and spherical field components, normalized to the total field strength. While the multicusp geometry is obvious at radii larger than 90 cm, the center of the vessel is shown to have a very weak dipole field in the $-\hat{z}$ direction.

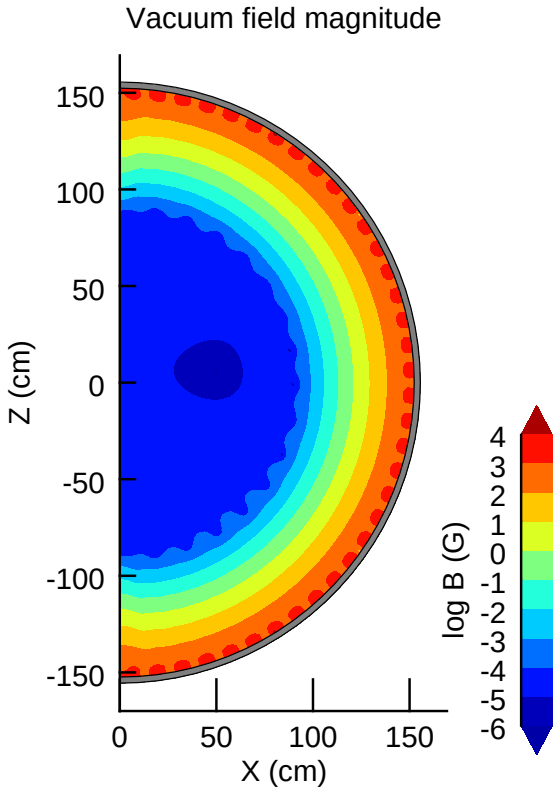

Figure A.3: Global contour plot of the vacuum field magnitude

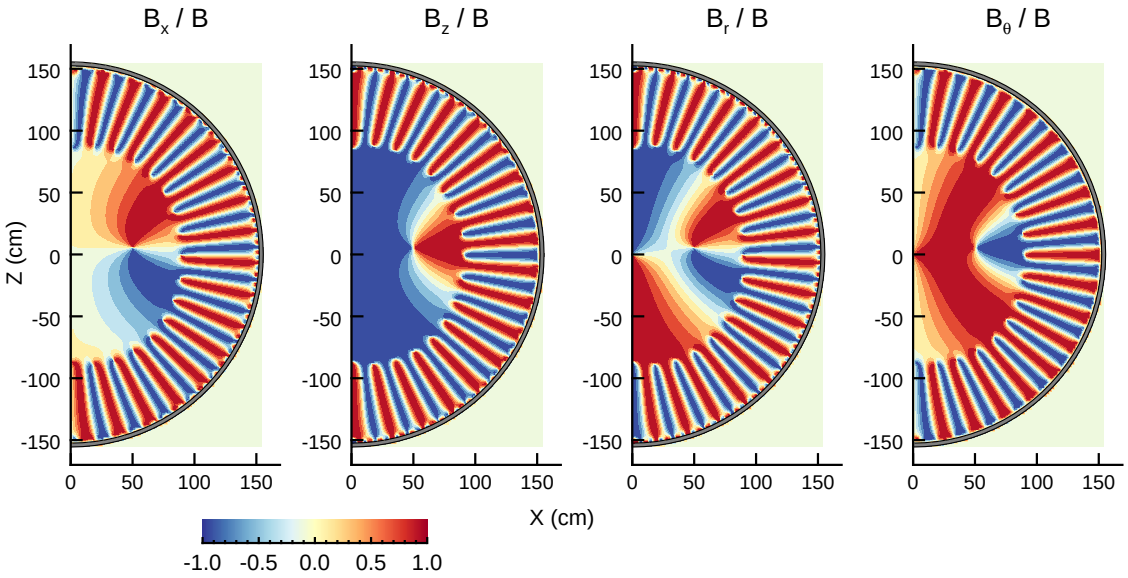

Figure A.4: Fractional components of vacuum magnetic field.

Appendix B: Hydrodynamic model

Numerical modeling of axisymmetric flows in the MPDX spherical geometry is a valuable tool in analyzing experimental results. Previous work has established a two-dimensional quasi-spectral code that solves the Navier-Stokes equation (Eq.5.1) using the boundary condition $\mathbf{v}(R) = v_\phi(\theta)$ at the plasma edge, which is expressed as a sum of spherical harmonics,

$$v_\phi = -\sum_{l=1}^{L} \tau_l \frac{\partial P_l(\cos\theta)}{\partial\theta}. \tag{B.1}$$

The discrete polar locations of the stirring cathode is decomposed into Fourier harmonics,

$$v_\phi = \sum_{n=1}^{N} a_n \sin 2n\theta + b_n \cos 2n\theta, \tag{B.2}$$

which are integrated to give the spherical harmonic coefficients τ_l that are the main input into the hydrodynamic Navier-Stokes solver,

$$\tau_l = \sum_{n=1}^{N} (F_{ln} a_n + G_{ln} b_n), \tag{B.3}$$

where the coefficients F_{ln} and G_{ln} are the integrals,

$$F_{ln} = \frac{2l+1}{2l(l+1)} \int_0^\pi \sin 2n\theta \sin^2\theta \frac{\partial P_l(\cos\theta)}{\partial\theta} d\theta, \tag{B.4}$$

$$G_{ln} = \frac{2l+1}{2l(l+1)} \int_0^\pi \cos 2n\theta \sin^2\theta \frac{\partial P_l(\cos\theta)}{\partial\theta} d\theta. \tag{B.5}$$

Fig.5.6 shows the discrete and spherical harmonic forms of the edge boundary conditions used for the counter- and co-rotation models discussed above. Also shown are the measured cathode discharge powers used to scale the edge boundary conditions. The red and blue curves indicate edge profiles where the flow between cathode rings has been scaled by 0.8 and 0.2 of the cathode drive amplitude, respectively. The black curve is the 0.5 scaling used in the models shown in Fig.5.5 and Fig.5.7.

REFERENCES

[1] H. Moffatt, *Magnetic field generation in electrically conducting fluids*. Mar 1978.

[2] H. Moffatt, "Stretch, twist and fold," *Nature*, vol. 341, no. 28 Sept., pp. 285–286, 1989.

[3] G. O. Roberts, "Dynamo action of fluid motions with two-dimensional periodicity," *Phil. Trans. R. Soc. Lond. A*, vol. 271, pp. 411–454, Dec 1972.

[4] S. Vainshtein and Y. B. Zel'dovich, "Origin of magnetic fields in astrophysics (turbulent "dynamo" mechanisms)," *Soviet Physics Uspekhi*, vol. 15, pp. 159–172, Sep 1972.

[5] D. Galloway and M. Proctor, "Numerical calculations of fast dynamos in smooth velocity fields with realistic diffusion," *Nature*, vol. 356, pp. 1–3, Jun 1992.

[6] R. Hollerbach, D. Galloway, and M. Proctor, "Numerical evidence of fast dynamo action in a spherical shell," *Physical Review Letters*, vol. 74, pp. 1–4, Apr 1995.

[7] D. Hughes, F. Cattaneo, and E. Kim, "Kinetic helicity, magnetic helicity, and fast dynamo action," *Physical Letters A*, pp. 1–6, Mar 1996.

[8] S. Balbus, "Enhanced angular momentum transport in accretion disks," *Ann. Rev. Astron. Astrophys.*, vol. 50, pp. 555–97, Feb 2003.

[9] U. Frisch and S. Orszag, "Turbulence: challenges for theory and experiment," *Phys. Today*, vol. 43, p. 24, 1990.

[10] E. Velikhov, "Stability of an ideally conducting liquid flowing between cylinders rotating in a magnetic field.," *Soviet Phys.-JETP*, vol. 36, pp. 995–998, 1959.

[11] S. Chandrasekhar, "The stability of non-dissipative couette flow in hydromagnetics," *Proc. Natl. Acad. Sci.*, vol. 46, pp. 253–257, 1960.

[12] S. Balbus and J. Hawley, "A powerful local shear instability in weakly magnetized disks," *Astrophys. J.*, vol. 376, p. 214, 1991.

[13] J. Hawley, "Global magnetohydrodynamical simulations of accretion tori.," *Astrophys. J.*, vol. 528, p. 462, 2000.

[14] J. Hawley, "Global magnetohydrodynamic simulations of cylindrical keplerian disks.," *Astrophys. J.*, vol. 554, p. 534, 2001.

[15] J. Hawley, C. Gammie, and S. Balbus, "Local three-dimensional magnetohydrodynamic simulations of accretion disks," *Astrophys. J.*, vol. 440, p. 742, 1995.

[16] A. Gailitis, O. Lielausis, E. Platacis, G. Gerbeth, and F. Stefani, "Laboratory experiments on hydromagnetic dynamos," *Rev. Mod. Phys.*, vol. 74, pp. 1–18, Sep 2002.

[17] R. Stieglitz and U. Muller, "Experimental demonstration of a homogeneous two-scale dynamo," *Phys. Fluids*, vol. 13, p. 561, Apr 2001.

[18] C. B. Forest, A. Bayliss, R. Kendrick, M. Nornberg, R. O'Connell, and E. Spence, "Hydrodynamic and numerial modeling of a spherical homogeneous dynamo experiment," *Magnetohydrodynamics*, vol. 38, p. 104, Nov 2002.

[19] R. Monchaux, M. Berhanu, M. Bourgoin…, M. Moulin, P. Odier, J.-F. Pinton, R. Volk, S. Fauve, N. Mordant, F. Petrelis, A. Chiffaudel, F. Daviaud, B. Dubrulle, C. Gasquet, L. Marie, and F. Ravelet, "Generation of a magnetic field by dynamo action in a turbulent flow of liquid sodium," *Phys. Rev. Lett.*, Jan 2007.

[20] E. Spence, M. Nornberg, C. Jacobson, C. Parada, N. Taylor, R. Kendrick, and C. B. Forest, "Turbulent diamagnetism in flowing liquid sodium," *Phys. Rev. Lett.*, vol. 98, p. 164503, Apr 2007.

[21] E. Kaplan, M. Clark, M. Nornberg, K. Rahbarnia, A. Rasmus, N. Taylor, C. B. Forest, and E. Spence, "Reducing global turbulent resistivity by eliminating large eddies in a spherical liquid-sodium experiment," *Phys. Rev. Lett.*, vol. 106, p. 254502, Jun 2011.

[22] H. Ji, J. Goodman, and A. Kageyama, "Magnetorotational instability in a rotating liquid metal annulus," *Mon. Not. Roy. Astron. Soc.*, vol. 325, pp. L1–L5, 2001.

[23] A. Roach, E. Spence, C. Gissinger, E. Edlund, P. Sloboda, and H. Ji, "Observation of a free-shercliff layer instability in cylindrical geometry," *Phys. Rev. Lett.*, vol. 108, p. 154502, 2012.

[24] S. Braginskii, "Transport processes in a plasma," *Rev. Plasma Phys.*, vol. 1, p. 205, May 1965.

[25] N. Katz, C. Collins, J. Wallace, M. Clark, D. Weisberg, J. Jara-Almonte, I. Reese, C. Wahl, and C. Forest, "Magnetic bucket for rotating unmagentized plasma," *Rev. Sci. Instrum.*, vol. 83, no. 063502, pp. 1–7, 2012.

[26] C. Collins, N. Katz, J. Wallace, J. Jara-Almonte, I. Reese, E. Zweibel, and C. B. Forest, "Stirring unmagnetized plasma," *Phys. Rev. Lett.*, vol. 108, p. 115001, Mar 2012.

[27] C. Collins, M. Clark, C. M. Cooper, K. Flanagan, I. V. Khalzov, M. D. Nornberg, B. Seidlitz, J. Wallace, and C. B. Forest, "Taylor-couette flow of unmagnetized plasma," *Physics of Plasmas*, vol. 21, p. 042117, Apr 2014.

[28] C. Collins, *Creating a Couette Flow of Unmagnetized Plasma for Magnetorotational Instability Studies in the Plasma Couette Experiment*. PhD thesis, UW Madison, Sep 2013.

[29] M. A. Lieberman and A. Lichtenberg, *Principles of Plasma Discharges and Materials Processing*. John Wiley & Sons, Inc., 2nd ed., 2005.

[30] D. Goebel, Y. Hirooka, and T. Sketchley, "Large-area lanthanum hexabordie electron emitter," *Rev. Sci. Instrum.*, vol. 56, pp. 1–6, May 1985.

[31] C. Cooper, W. Gekelman, P. Pribyl, and Z. Lucky, "A new large area lanthanum hexaboride plasma source," *Rev. Sci. Instrum.*, vol. 81, p. 083503, Jan 2010.

[32] D. M. Goebel and R. M. Watkins, "Compact lanthanum hexaboride hollow cathode," *Rev. Sci. Instrum.*, vol. 81, p. 083504, Jan 2010.

[33] C. Cooper, J. Wallace, M. Brookhart, M. Clark, C. Collins, W. Ding, K. Flanagan, I. Khalzov, Y. Li, J. Milhone, M. Nornberg, P. Nonn, D. Weisberg, D. Whyte, E. Zweibel, and C. Forest, "The madison plasma dynamo experiment: A facility for studying laboratory plasma astrophysics," *Physics of Plasmas*, vol. 21, pp. 1–11, Jan 2014.

[34] C. Forest, K. Flanagan, M. Brookhard, M. Clark, C. Cooper, V. Desangles, J. Egedal, D. Endrizzi, I. Khalzov, H. Li, M. Miesch, J. Milhone, M. Nornberg, J. Olson, E. Peterson, F. Roesler, A. Schekochihin, O. Schmitz, R. Siller, A. Spitkovsky, A. Stemo, J. Wallace, D. Weisberg, and E. Zweibel, "The wisconsin plasma astrophysics laboratory," *Journal of Plasma Physics*, vol. 81, no. 05, p. 345810501, 2015.

[35] M. Coakley, F. Roesler, R. Reynolds, and S. Nossal, "Fabry-perot ccd annular-summing spectroscopy: study and implementation for aeronomy applications," *Applied Optics*, vol. 35, pp. 6479–6493, Oct 1996.

[36] N. Hershkowitz, K. Leung, and T. Romesser, "Plasma leakage through a low-beta line cusp," *PRL*, pp. 1–4, Oct 1975.

[37] G. Knorr and D. Willis, "Leak width of a cusp-confined plasma," *Z. Naturforsch*, vol. 37q, pp. 780–785, Feb 1982.

[38] C. Koch and G. Matthieussent, "Collisional diffusion of a plasma in multipolar and picket fence devices," *Phys. Fluids*, vol. 26, p. 545, May 1982.

[39] K. Leung, N. Hershkowitz, and K. Mackenzie, "Plasma confinement by localized cusps," *Phys. Fluids*, vol. 19, p. 1045, 1976.

[40] C. Gauthereau, G. Matthieussent, J. Rauch, and J. Godiot, "Adjustable plasma density gradient in a multipolar discharge," *Physics Letters A*, vol. 101A, pp. 394–396, May 1984.

[41] C. Gauthereau and G. Matthieussent, "Plasma density profiles in discharges surrounded by magnetic multipole walls," *Physics Letters A*, vol. 102A, pp. 231–234, May 1984.

[42] A. Fukano, T. Mizuno, A. Hatayama, and M. Ogasawara, "Estimation of the cusp loss width in negative-ion sources," *Rev. Sci. Instrum.*, vol. 77, p. 03A524, Jan 2006.

[43] O. Olson and H. Skarsgard, "The diffusion of highly ionized plasma across magnetic field," *Canadian Journal of Physics*, vol. 43, pp. 1–17, Feb 1964.

[44] A. H. Boozer, "Establishment of magnetic coordinates for a given magnetic field," *Phys. Fluids*, vol. 25, p. 520, Jan 1982.

[45] W. D'haeseleer, W. Hitchon, J. Callen, and J. Shohet, "Flux coordinates and magnetic field structure," *Springer Series in Computational Physics*, pp. 1–126, Feb 1991.

[46] W. Press, S. Teukolsky, W. Vetterling, and B. Flannery, *Numerical Recipes: the art of scientific computing*. Cambridge University Press, 3rd ed., 2007.

[47] H. Mott-Smith and I. Langmuir, "The theory of collectors in gaseous discharges," *Physical review*, Jan 1926.

[48] S. Self and H. Ewald, "Static theory of a discharge column at intermediate pressures," *Physics of Fluids*, Jan 1966.

[49] F. Chen, "Langmuir probe diagnostics," *Mini-course on Plasma Diagnostics, IEEE-ICOPS 2003*, pp. 1–42, May 2003.

[50] N. Hershkowtitz, *Plasma Diagnostics*, ch. 3. How Langmuir Probes Work, pp. 113–183. Academic Press, Inc., Apr 1989.

[51] P. Prewett and J. Allen, "The double sheath associated with a hot cathode," *Proc. Roy. Soc. Lond. A*, vol. 348, pp. 435–446, Sep 1976.

[52] M.-H. Cho, N. Hershkowitz, and T. INTRATOR, "Particle and power balances of hot-filament discharge plasmas in a multidipole device," *J. Appl. Phys.*, vol. 67, pp. 1–6, May 1990.

[53] C. B. Forest and N. Hershkowtitz, "Steady-state ion pumping of a potential dip near an electron collecting anode," *Journal of Applied Physics*, vol. 60, p. 1295, Jan 1986.

[54] L. A. Schwager, "Effects of secondary and thermionic electron emission on the collector and source sheaths of a finite ion temperature plasma using kinetic theory and numerical simulation," *Phys. Fluids B*, vol. 5, p. 631, Jan 1993.

[55] A. Kramida, Y. Ralchenko, J. Reader, and the NIST ASD Team, "Nist atomic spectra database (version 5.3), [online]," 2015.

[56] N. Hershkowitz, "Sheaths: More complicated than you think," *Physics of Plasmas*, vol. 12, p. 055502, Jan 2005.

[57] D. Whyte, T. Evans, A. Kellman, D. Humphreys, A. Hyatt, T. Jernigan, R. Lee, S. Luckhardt, P. Parks, and M. S. et al., "Proceedings of the 24th european conference on controlled fusion and plasma physics," vol. 21A, p. 1137, 1997.

[58] P. C. Stangeby, "Plasma sheath transmission factors for tokamak edge plasmas," *Physics of Fluids*, vol. 27, p. 682, Jan 1984.

[59] J. P. Sheehan, N. Hershkowitz, I. D. Kaganovich, H. Wang, Y. Raitses, E. V. Barnat, B. R. Weatherford, and D. Sydorenko, "Kinetic theory of plasma sheaths surrounding electron-emitting surfaces," *Physical Review Letters*, vol. 111, p. 075002, Aug 2013.

[60] S. Takamura, N. Ohno, M. Y. Ye, and T. Kuwabara, "Space-charge limited current from plasma-facing material surface," *Contrib. Plasma Phys.*, vol. 44, pp. 126–137, Apr 2004.

[61] M. Y. Ye and S. Takamura, "Effect of space-charge limited emission on measurements of plasma potential using emissive probes," *Physics of Plasmas*, vol. 7, no. 8, pp. 3457–3463, 2000.

[62] M. D. Campanell, "Entire plasmas can be restructured when electrons are emitted from the boundaries," *Physics of Plasmas*, vol. 22, p. 040702, Apr 2015.

[63] E. Bullard and H. Gellman, "Homogeneous dynamos and terrestrial magnetism," *Phil. Trans. R. Soc. Lond. A*, vol. 247, pp. 213–278, Feb 1954.

[64] I. Khalzov, B. Brown, C. Cooper, D. Weisberg, and C. Forest, "Optimized boundary driven flows for dynamos in a sphere," *Phys. Plasmas*, vol. 19, pp. 1–12, Apr 2012.

[65] M. Miesch and B. Hindman, "Gyroscopic pumping in the solar near-surface shear layer," *The Astrophysical Journal*, pp. 1–27, Aug 2011.

[66] I. V. Khalzov, B. P. Brown, F. Ebrahimi, D. D. Schnack, and C. Forest, "Numerical simulation of laminar plasma dynamos in a cylindrical von kármán flow," *Physics of Plasmas*, vol. 18, p. 032110, Jan 2011.

[67] M. S. Miesch and J. Toomre, "Turbulence, magnetism, and shear in stellar interiors," *Annu. Rev. Fluid Mech.*, vol. 41, pp. 317–345, Jan 2009.

[68] G. Taylor, "Stability of a viscous liquid contained between two rotating cylingers," *Phil. Trans. R. Soc. Lond.*, vol. 223, p. 289, 1923.

[69] J. D. Jackson, *Classical Electrodynamics*. John Wiley & Sons, Inc., 3rd ed., 1999.